Cryo-electron microscopy of Weibel-Palade Bodies in human endothelial cells

James William Albert Streetley

16th December 2014

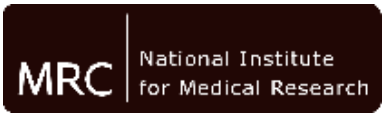

Thesis submitted for the degree of Doctor of Philosophy

I, James Streetley, confirm that the work presented in this thesis is my own. Where information has been derived from other sources, I confirm that this has been indicated in the thesis.

Abstract

Weibel-Palade bodies (WPBs) are a secretory storage organelle found in endothelial cells. Their primary cargo is the large haemostatic protein von Willebrand factor (VWF), however there are many other minor components, both in the membrane and lumen of the WPB. VWF is stored in long helical tubules which define the 'rod-like' shape of the WPBs. WPBs are released in response to raised intracellular Ca^{2+} or cAMP levels, secreting the VWF content. Upon exocytosis, the environment of the VWF changes from acidic to neutral pH, causing the tubules of VWF to unfurl into strings. The expansion of the VWF tubules into strings exposes binding and cleavage sites, turning VWF into its haemostatically active form. As tubules transform into strings, the overall shape of the WPB changes, first becoming round before releasing its contents.

Imaging at the periphery of frozen-hydrated, whole human umbilical vein endothelial cells (HUVECs) by cryo-electron microscopy (cryo-EM) and cryo-electron tomography has been used to study WPBs within their native environment. The structure of WPBs within HUVECs both unstimulated and stimulated to release WPBs with raised intracellular Ca^{2+} has been examined. This has enabled imaging of both rod-shaped and rounded WPBs. Round WPBs in HUVECs exposed to hypotonic shock and within human heart microvasculature endothelial cells (HHMECs) have also been imaged.

A subset of the WPBs imaged within endothelial cells contain an internal vesicle within them. Light microscopy studies have shown a vesicle with corresponding characteristics is enriched for the membrane protein CD63, a known constituent of WPBs.

Finally, a technique for chemically fixing cells for light microscopy studies prior to plunge-freezing is shown, with subsequent correlative light and electron microscopy experiments looking at CD63-enriched vesicles within WPBs. The quality of preservation for cryo-EM experiments, including tomography and image processing for correlative microscopy is discussed.

Contents

Acknowledgements

Firstly, I would like to thank my supervisor, Dr Peter Rosenthal, for giving me this project and supporting me through it, particularly for always having an open door for the discussion of images, new experiments or analyses. I would also like to thank my second supervisor, Dr Tom Carter, for helping me with all the biological aspects of this project and providing the cell samples. I am grateful to Dr Justin Molloy and Dr Jean-Paul Vincent for their thoughtful comments as members of my thesis committee.

All members of the Rosenthal lab past and present have helped me out greatly with both the project and making the group a fun place to work. Particular thanks go to Dr Rishi Matadeen, who got me trained up as a cryo-microscopist and tomographer and Dr Sebastian Wasilewski, who trained me in tomographic processing and kept my computer running smoothly. Dr Tim Grant fielded many stupid questions and only sometimes laughed at them, which is commendable.

The whole Carter lab have been very generous with their reagents, bench space and time. In particular, I thank Laura Knipe, who taught me cell culture and Dr Violeta Fonseca, who conducted the light microscopy investigations into the WPB internal vesicles in Chapter 5.

I thank the Confocal and Image Analysis Lab at NIMR for their training and advice on all the light microscopy experiments.

I am indebted to Wiebke, who has been supported me throughout the project and been a patient listener during the difficult parts. Her support during the writing-up phase has been great; keeping me fed and in clean clothes. I hope to return the many favours when she writes up.

The wider NIMR community have made studying here a great experience; something I hope they will be able to replicate at the Crick. I therefore thank all those whom I've propped up the bar with, played football with, danced with or put on theatre shows with.

Lastly, I thank my family for all their support throughout the last 8 years of my studies in London. Even if they weren't always sure what I was doing or why I wanted to do it, their faith, interest and encouragement has been a huge help.

Abbreviations

2D	two-dimensional
3D	three-dimensional
ADAMTS13	a disintegrin and metalloproteinase with a thrombospondin type 1 motif, member 13
cAMP	3'-5'-cyclic adenosine monophosphate
CCD	charge coupled device
CFP	cyan fluorescent protein
CK	cystine knot
CLEM	correlative light-electron microscopy
EGFP	enhanced green fluorescent protein
EM	electron microscopy
ER	endoplasmic reticulum
ESCRT	endosomal sorting complex required for transport
FFT	fast Fourier transform
FIB	focussed ion beam
FRAP	fluorescence recovery after photobleaching
GFP	green fluorescent protein
HHMEC	human heart microvasculature endothelial cells
HUVEC	human umbilical vein endothelial cells
IHRSR	Iterative Helical Real Space Reconstruction

IL-8	Interleukin-8
ILEM	integrated light and electron microscope
ILV	intraluminal vesicle
MyoVa	myosin Va
MyRIP	myosin and Rab27a interacting protein
NSF	N-ethylmaleimide sensitive fusion protein
PBS	phosphate buffered saline
PDBe	Protein Data Bank in Europe
PFA	paraformaldehyde
SEM	scanning electron microscope
Slp4-a	synaptotagmin-like protein 4-a or granulphilin
SM	Sec1/Munc18-like
SNARE	soluble NSF attachment protein receptor
STORM	stochastic optical reconstruction microscopy
STXBP1	Syntaxin binding protein 1 or Munc18-1
TGN	trans-Golgi network
VAMP	vesicle associated membrane protein
VWA	von Willebrand Factor A domain
VWF	von Willebrand Factor
WPB	Weibel-Palade body

List of Tables

List of Figures

1 Introduction

1.1 Weibel-Palade Bodies

1.1.1 Discovery, formation and composition of WPBs

Weibel-Palade bodies (WPBs) are secretory storage organelles found in endothelial cells. They were first discovered in 1964 by Ewald Weibel and George Palade who observed a new "rod-shaped tubulated body" in the endothelial cells of multiple small arteries in human and rat, using electron microscopy (EM). They described small, regularly spaced cylindrical tubules within the body, enclosed by a limiting membrane [129].

Subsequently, in 1982, a combination of immunofluorescence microscopy and immunoelectron microscopy ascertained that the haemostatic protein von Willebrand factor (VWF) is stored in WPBs [123]. The pattern of immunogold labelling even suggested the VWF was responsible for the striated tubules of WPBs, lying along the long axis of the bodies. In his 50^{th} anniversary review [128], Ewald Weibel credits Wagner et al [123] with an independent rediscovery of the Weibel-Palade body, as they had been looking for locations of VWF storage, rather than the specific cargo of WPBs.

VWF is the main cargo of WPBs and was initially thought to be the only component of the granules [28]. In fact, many other proteins are incorporated into WPBs (table 1, reviewed in [67]), but VWF is by far the most prevalent [28]. The expression of VWF in cells that do not natively express VWF is enough to induce formation of rod-shaped WPB-like structures in those cells [124], indicating that VWF levels are the driving force behind WPB formation and that the rod-like shape of the organelle is directly related to the tubule structure of its main cargo.

Therefore, the first step of WPB formation is VWF synthesis. VWF is translated as a 2813 residue sequence, but processed into a signal peptide, proregion and mature subunit ([115], figure 1a). The signal peptide is responsible for ensuring the nascent

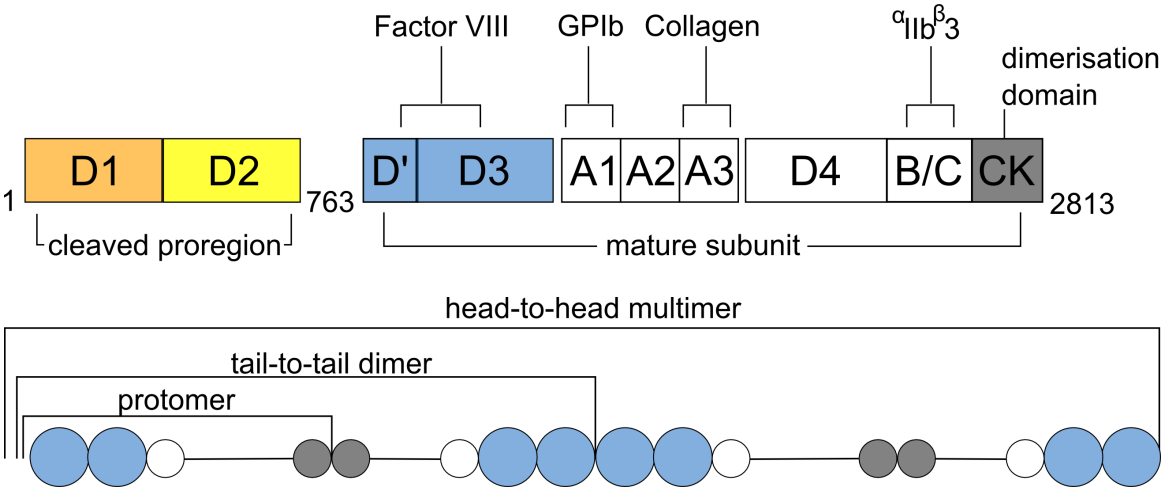

Figure 1: **A** Domain organisation of VWF, with key binding sites marked. Residues 1-22 make up the signal peptide (not shown) **B** Organisation of the VWF multimers, using the same colour scheme.

polypeptide chain enters the endoplasmic reticulum (ER) where it is then cleaved and lost. Mature VWF is highly glycosylated, with 12 N-linked and 10 O-linked oligosaccharides [106] and this process starts in the ER with N-linked oligosaccharide addition. Subsequently, covalent 'tail-to-tail' dimers are formed by 3 interchain disulphide bonds between cystine knot (CK) domains ([106, 61, 139], figure 1). The crystal structure of dimerised CK domains show that in addition to the 3 interchain disulphide bonds, there is also an extensive hydrogen bond network within the dimer and each CK domain is also reinforced with 4 intrachain disulphide bonds [139]. The intrachain disulphide bonds form an 8 residue ring, with an additional intrachain disulpide passing through the ring [139] and giving rise to the 'knot' name. Both the N-linked glycosylation and C-terminal dimerisation steps are required for VWF dimers to pass into the Golgi apparatus [122].

Glycosylation also continues in the Golgi apparatus with the O-linked sugars. Within the Golgi and trans-Golgi network (TGN), the proregion (figure 1) is cleaved by furin [131] but stays associated with mature VWF. Association of proregion with mature VWF is required for multimer formation [116, 121], and multimerisation can occur even if a non-cleavable mutant of proVWF is used [117]. In the TGN, VWF

dimers form covalent, linear 'head-to-head' multimers through disulphide bond formation between D3 domains [61, 106, 120, 121]. Multimerisation requires an acidic pH and presence of Ca^{2+} ions [122, 47], and can continue within immature WPBs which have a similar pH [26]. Multimerisation can lead to VWF chains up to 20 MDa in size ([91], figure 1).

VWF tubules begin to form in the TGN (figure 2, [134]). Tubule formation is an efficient, paracrystalline method of packing the VWF cargo into the WPB [4] which allows the VWF tubules to expand 50-fold in length upon unfurling [103]. Tubulation is an independent step from multimerisation, however both must occur for VWF to be functional upon WPB exocytosis [68, 67]. The minimal requirements for tubulation are the D1D2-D'D3 domains with the non-covalent interaction between proregion (D1D2) and D'D3 domains forming the tubule (figure 1 and figure 3, [68, 47]).

WPBs bud from the TGN through the selective aggregation of VWF tubules but require an AP-1/clathrin coat in order to emerge as a nascent WPB [59, 134]. Once a nascent granule has left the TGN, there are still other steps through which it must pass before achieving maturation (figure 2). One marker of maturation is acquiring the small GTPase Rab27a [40]. Rab27a is recruited in a specific manner hours after leaving the Golgi [40] and forms part of a complex which anchors the WPBs to actin at the cell periphery ([73], section 1.1.4). The granules also condense with maturation, becoming more electron dense as tubules become closer to each other and granule width decreases [134].

As shown in table 1, WPBs can contain many other components as well as their primary VWF cargo. Some components, such as the membrane protein P-selectin, are incorporated into the WPB at the Golgi [43] and others are delivered post-Golgi as a mark of maturation, such as Rab27a [40] or Rab3D [53]. The membrane protein CD63 is delivered post-Golgi in an AP-3 dependent manner via late endosomes/multivesicular bodies (MVBs) [43, 83]. CD63 is a tetraspanin found on endosomal compartments, and its presence on WPBs, combined with their acidic pH marks them a

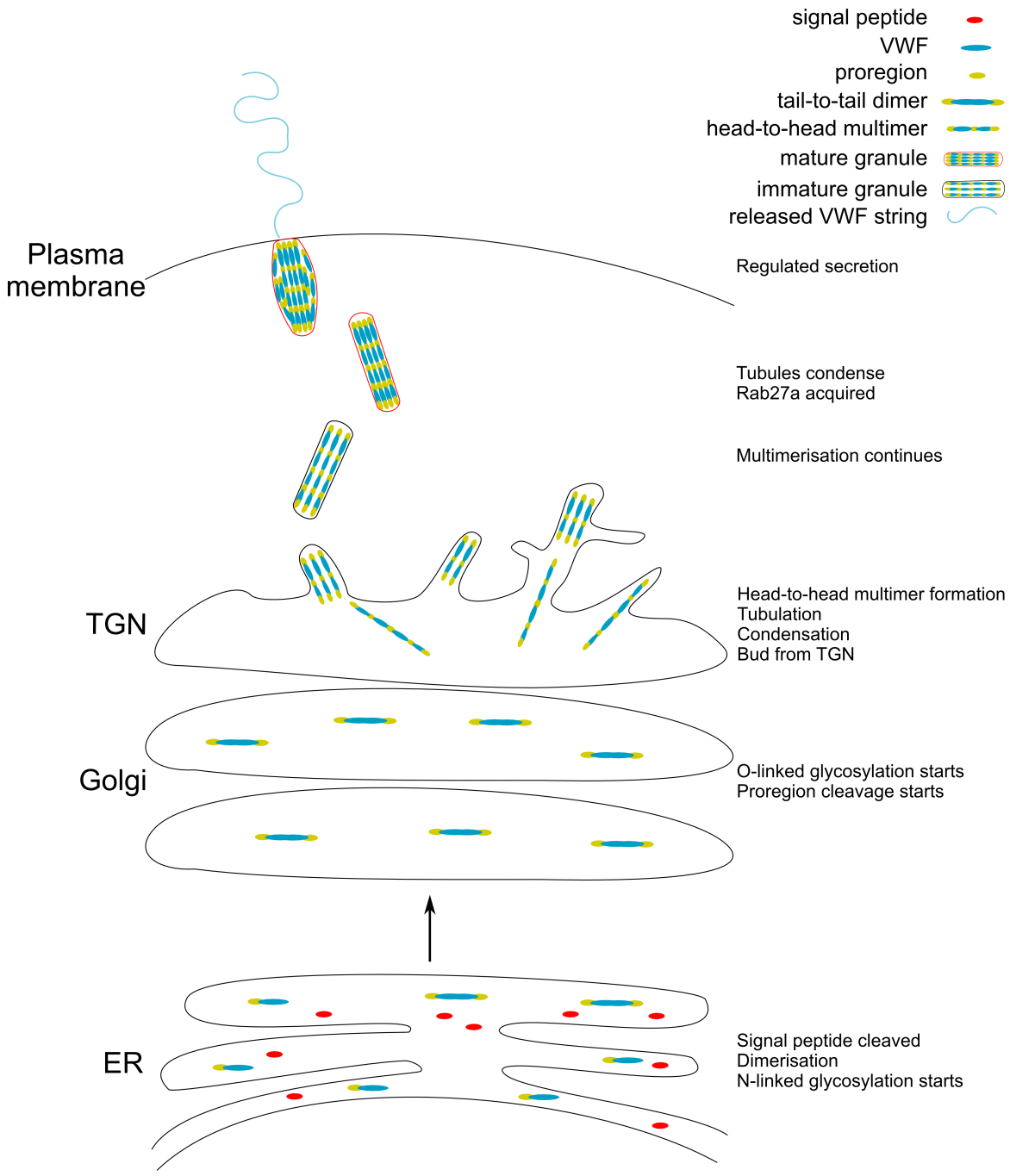

Figure 2: Biogenesis of WPBs and processing of VWF. Adapted from [69].

Protein	Role	Recruitment	Reference
VWF	Haemostasis	TGN	[123]
Proregion	Tubulation of VWF	TGN	[28]
P-selectin	Leukocyte adhesion, haemostasis	TGN	[7]
Osteoprotegerin	Regulates osteoclast levels. Unknown in WPBs	TGN	[133]
Clathrin/AP-1	Budding of WPB from TGN	TGN	[59]
α-1,3-Fucosyltransferase VI	Glycosylation in Golgi. Unknown in WPBs	TGN	[94]
Angiopoietin-2	Angiogenesis, inflammation, vascular homeostasis	TGN	[31]
Calcitonin gene-related peptide	Vasodilation	TGN	[77]
Endothelin-1	Vasoconstriction	TGN	[77]
Interleukin-8	Leukocyte adhesion, inflammation	TGN	[108]
Tissue-type plasminogen activator	Fibrinolysis	TGN	[48]
Eotaxin-3	Leukocyte recruitment	TGN	[76]
VAMP3	v-SNARE	TGN	[84]
VAMP8	v-SNARE	TGN	[84]
CD63	Cell adhesion/migration, membrane organisation	Post-Golgi	[119]
Rab3D	Membrane trafficking regulation	Post-Golgi	[53]
Rab27a	Association with MyRIP/MyoVa	Post-Golgi	[40]
Rab15	Membrane trafficking regulation	Post-Golgi	[140]
Rab33a	Membrane trafficking regulation	Post-Golgi	[140]
Rab37	Membrane trafficking regulation	Post-Golgi	[140]
Munc13-4	Rab effector protein	Post-Golgi	[140]
Slp4-a	Rab effector protein, binds syntaxin	Post-Golgi	[5]
MyRIP	Rab27a effector protein, binds to MyoVa	Post-Golgi	[73]

Table 1: Table showing WPB components, roles and recruitment points.

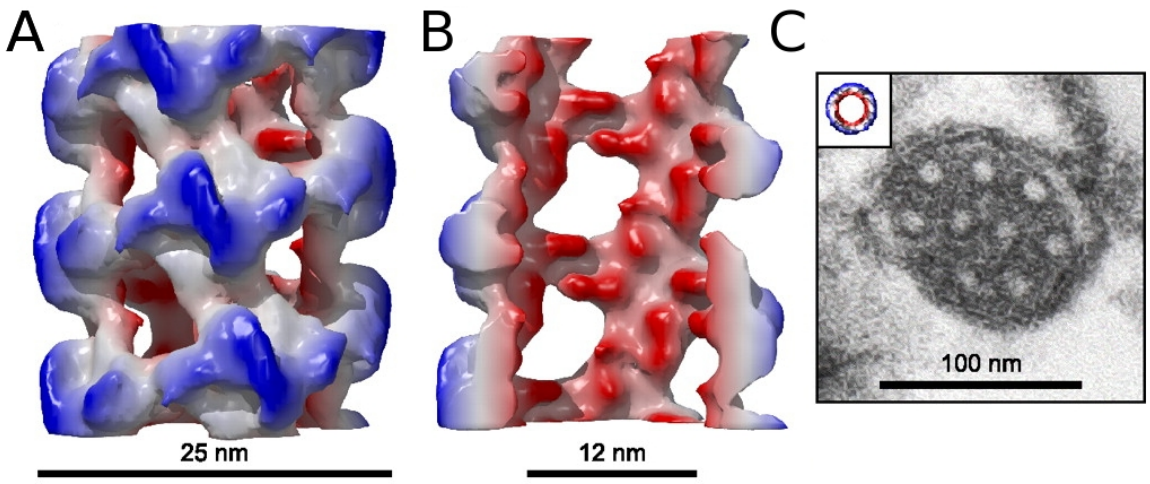

Figure 3: **A** Surface model of VWF tubule formed by D1D2 and D'D3 domains. Colour denotes distance from helical axis (red to blue). External diameter of tubule is 25 nm. **B** Cutaway view of tubule in A. Internal diameter is 12 nm. **C** Electron micrograph of WPB cross-section showing tubules compared with model tubule (inset) at same scale. From [47], copyright by the National Academy of Sciences.

lysosome-related organelles.

As some components are delivered post-Golgi and at different times, not every WPB contains all of these components, leading to different populations of WPBs within the cell. These additional components can be broadly divided into two groups; those with a role in haemostasis and those involved in the trafficking and secretion of the WPB. In addition to gaining components, content may also need to be removed from the WPB, such as clathrin/AP-1, once the WPB has emerged from the TGN [134]. It is possible that some proteins found in WPBs in over-expression studies are not targeted to the WPB, but not completely excluded from WPBs, as over expression of EGFP in the secretory pathway is found in WPBs with a similar storage efficiency to IL-8, IL-6, tPA and eotaxin-3 [52].

In addition to being packaged in WPBs, VWF is also constitutively secreted by endothelial cells. Pulse-chase experiments with radiolabelled ^{35}S methionine determined that an average of 5 % of newly synthesised VWF was targeted to the regulated pathway and the rest was constitutively released in low molecular weight forms [101]. More recent work has suggested that circulating VWF levels in the absence of stimulation

arise from basal exocytosis of WPBs, with 50 % of newly synthesised VWF being released without stimulation within 24 hours and 80 % of that coming from WPBs [37]. This means much of the VWF released without stimulation is targeted to storage, rather than directly released after synthesis and in contrast to the low proportion of VWF previously thought to be stored. Basal release of stored VWF from WPBs also allows for the release of mature VWF rather than the dimers and low molecular weight forms that are constitutively released [37].

1.1.2 Structure of WPBs and VWF

Von Willebrand factor is a highly repetitive protein with 4 types of repeated domains; A, B, C and D [115] and a C-terminal cystine knot domain for dimerisation (figure 1). As in section 1.1.1, the D domains of proregion and at the N-terminus of mature VWF are used for multimerisation and D'D3 contains the factor VIII binding site [91]. The repeated A domains contain binding sites for collagen and platelet glycoproteins [91] and the cleavage site for the protease ADAMTS13, which regulates the length of circulating VWF multimers by cleaving at partially unfolded A2 domains [136, 103]. The B and C domains, recently reclassified as all belonging to a group of VWC domains [138], form 6 tandem repeats towards the C-terminus of VWF. The fourth repeat, corresponding the C1 domain (or VWC4 in the re-assignment) contains the binding site for the platelet integrin $\alpha_{IIb}\beta_3$ [138].

In WPBs, VWF multimers are packaged as long, helical tubules which give rise to the elongated morphology of WPBs [109, 4]. The helical structure of an *in vitro*, truncated VWF construct has also been calculated (figure 3, [47]). A comparison of the two VWF tubule models; from WPBs within cells and an *in vitro* truncation of just the D domains (D1D2D'D3) shows that they are quite similar. They share similar helical pitch, with the 120 Å pitch from VWF in WPBs [4] being one of the 5 helices formed by negatively stained, truncated VWF *in vitro* with pitches from 96-120 Å, [47]. The overall dimensions are also similar, with WPBs forming 24 nm tubules with

a 12 nm internal diameter and in vitro tubules forming 25 nm tubules with a 12 nm internal diameter. Both reconstructions also contain large fenestrations within the tubule.

The similarity between the two helices seems surprising because the *in vitro* helix is formed by only 44 % (residues) of the full-length VWF. This indicates that the remainder of the C-terminus not in the *in vitro* tubules can not be packed in the same manner as the D1D2-D'D3 domains that form the density seen in the tubule reconstructions. It must therefore be highly flexible, not conforming to the helical symmetry of the N-terminal domains, and have been 'averaged out' across the full-length helical reconstructions. Tubule formation with only the D1D2-D'D3 domains demonstrates that neither the C-terminal domains, nor tail-to-tail dimerisation through those domains are requirements for tubulation [47, 68].

The structure of the C-terminal domains has been examined using truncation mutants containing C-terminal domains (A1-CK and smaller) and imaging by negative stain EM, under the dimerisation promoting conditions found in the TGN [137]. Images of these constructs at pH 6.2 showed the C-terminal region to have a 'dimeric bouquet' structure (figure 4b), where the 'flowers' are the A1-A2-A3-D4 domains, the 'stem' is formed from B1-B2-B3-C1-C2 and the base from the CK domain dimer. In A1-CK constructs, the density for the A1 and A2 domains in class averages is much weaker than for the A3-CK stem region, indicating that the A domains are separated by flexible linkers and are being averaged out. This is consistant with images of A1-A2-A3 alone, which show variable distances and angles between the domains, again indicating a flexible linker [137]. These findings led to the proposition of a model for how the C-terminal dimeric bouquet fits with the N-terminal tubule information above (figure 4a, [137, 36]).

Such a model does not fully explain how such a tubule would pack into WPBs, decorated by ~51 nm dimeric bouquets. The A1-A2 region appears to be flexible, and so it could be possible that the bouquet extends not radially (as drawn) but instead in

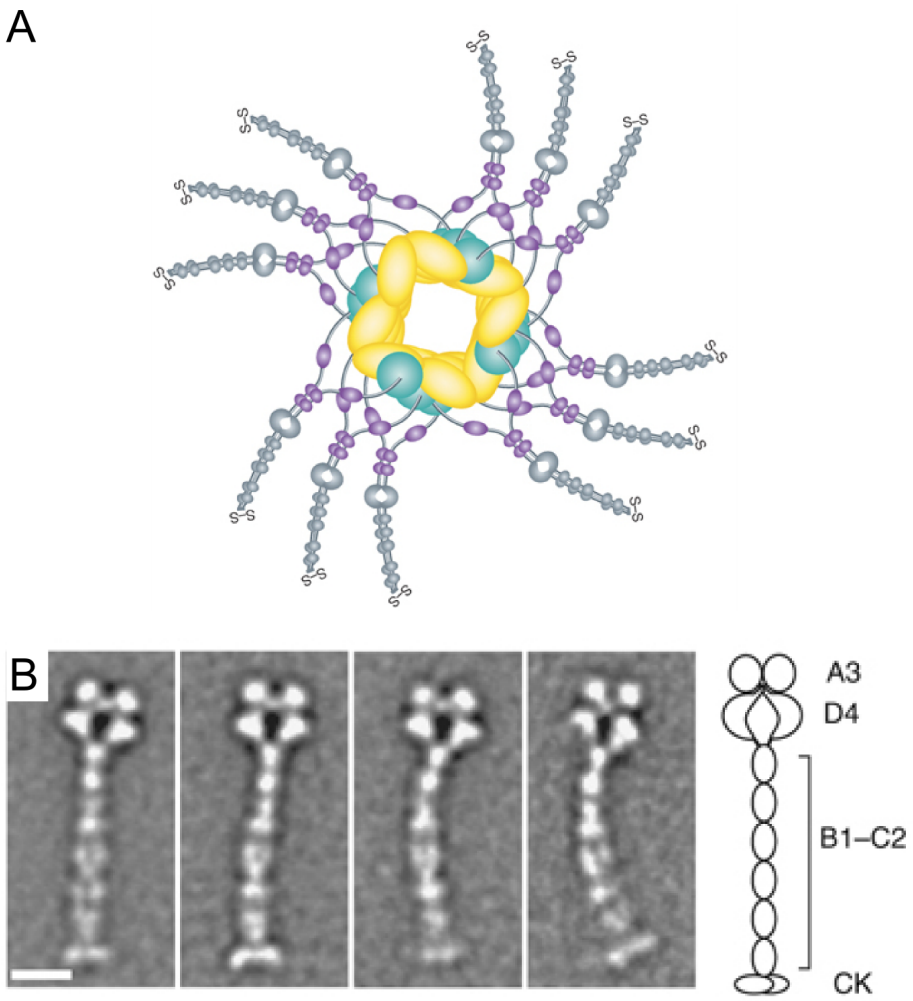

Figure 4: **A** Schematic of the axial view of a VWF tubule, showing how D1-D2 (yellow) and D'-D3 (green) might form a helix decorated by flexible dimeric bouquets formed by A1-A2-A3 (purple), and D4-B1-B2-B3-C1-C2-C3-CK (grey). From [36], copyright European Molecular Biology Organization. **B** Negative stain EM class averages of the C-terminal dimeric bouquet formed by A3-CK truncation of VWF at pH 6.2. A1-A2 not shown. Scale bar: 10 nm. From [137], copyright European Molecular Biology Organization.

an axial fashion [137]. The flexibility of the A1-A2 region may allow it to act as a hinge, so the C-terminal region can break with the helical symmetry to pack around other tubules, meaning it would not be visible in a helical reconstruction. This concept is imaginable when the tubules are less densely packed before maturation, where the centre-to-centre spacing may be greater [134], but when centre-to-centre distance between tubules becomes only a few nanometres larger than the tubules themselves (28.4 nm ± 3.1 nm for a 24 nm tubule) [4] then it becomes less clear.

The large size of VWF makes obtaining crystals for structure determination by X-ray crystallography unlikely, but the structures of some individual domains of VWF have been crystallised and determined, namely the A domains and CK domain.

The A domains are the defining members of a family of domains known as the VWA domains [102, 103]. The domain consists of a central, 5-stranded β-sheet with a single anti-parallel strand surrounded by 6 α helices, and PDBe (Protein Data Bank in Europe, *https://www.ebi.ac.uk/pdbe*) shows 27 structures across the A domains from multiple organisms and with various ligands. Whilst A1 and A3 contain the binding sites for the platelet glycoprotein GpIbα and collagen respectively [91], A2 does not contain a binding site but instead the cleavage site for ADAMTS13. Additionally, the A2 structure shows it missing both the α4 helix and a long-range disulphide bond contained in the other A domains [135], rendering it less stable. The structure also shows that the ADAMTS13 cleavage site is well buried within the domain, indicating that partial unfolding would be required to make the cleavage site accessible. The force required to partially unfold the VWF A2 domain is similar to the force VWF experiences in the vasculature and this elongation force is required for ADAMTS13 to cleave the domain [136]. Together, these experiments indicate that the A2 domain is a "force-sensing" domain which permits cleavage of itself by ADAMTS13 in VWF multimers under conditions found in the vasculature [136, 135, 103].

In contrast, the structure of the CK domain demonstrates features allowing it to resist such force, being heavily reinforced with hydrogen bonds and many disulphide

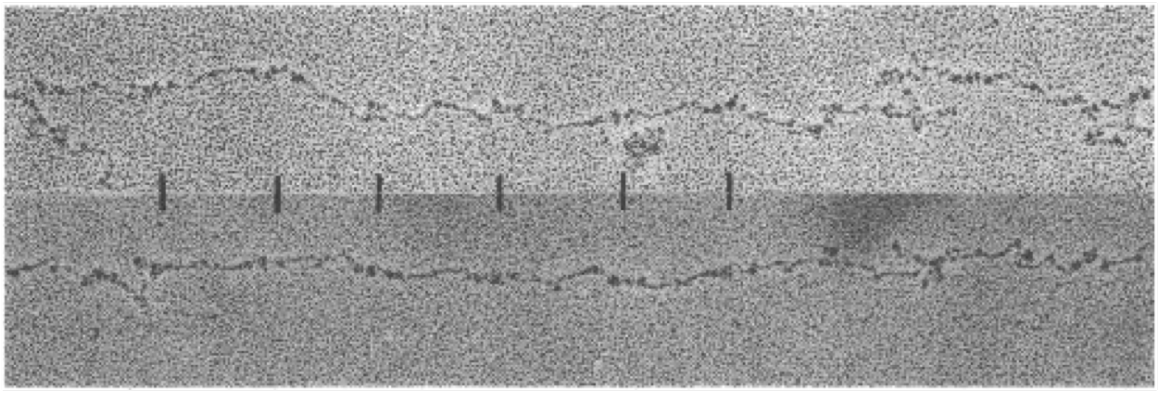

Figure 5: Electron micrographs of VWF in an extended, string form, isolated from fresh plasma and prepared using the "glycerol spray/vacuum dry" method. Bars show 120 nm repeats of the fully extended monomer. Republished with permission of The American Society for Clinical Investigation, Inc., from [32]; permission conveyed through Copyright Clearance Center, Inc.

bonds [139], both to stabilise the domain and to dimerise VWF monomers.

Upon secretion, VWF undergoes a large structural transformation, from tightly packed, helical tubules to the linear strands that can be isolated from blood (figure 5, [32, 98]). VWF strings show nodular domains that repeat with a periodicity of 120 nm and two-fold symmetry about a central axis [32], reflecting that the multimers are made from repeating dimers. These strings can be very long, up to a millimetre and form along the endothelial surface binding platelets [21].

This large change in conformation; from a tightly packed helical tubule, to a long, extended string results in a 50-fold expansion in length [17], indicating how efficient VWF storage in WPBs is. This structural change exposes the hidden binding and cleavage sites in the A domains and is mediated through the change in pH upon exocytosis and shear force from blood flow through the vasculature [68, 103]. As discussed in section 1.1.1, WPBs bud from the TGN, where the pH is ~6.4 , and this is also the condition at which VWF tubules form. WPBs then acidify with maturation to reach a pH of 5.5 [26]. Upon exposure to blood, with a neutral pH (7.2), the non-covalent interactions that were formed at acidic pH are now lost. This includes the interaction between proregion and mature VWF, causing the tubules to unfurl and proregion to freely diffuse away from the fusion site [41].

The link between pH and unfurling has been demonstrated by treating cells with the drug monensin, which neutralises the pH of acidic organelles, and then denuding the WPBs of their enclosing membrane with Triton X-100. This causes VWF to disperse, whereas detergent treatment alone leaves relatively stable VWF staining [68]. Pre-treatment with monensin before inducing secretion leads to the secretion of shorter, less effective VWF strings. This has led to the hypothesis that tubules are more than a convenient method for storing such large multimers as mature VWF, but also provide a mechanism for orderly uncoiling, such that tangles are not formed [68]. This has recently been challenged by fluoresence microscopy of secreted VWF in the presence and absence of flow, which indicate that in the absence of flow, VWF is secreted as patches on the cell surface from which strings can form if flow is subsequently started [70], meaning that tubules need not directly unfurl into strings but can be formed via an intermediate.

Without shear flow conditions, a third conformation for VWF is possible where the strings are not extended but wrapped up as a "ball of yarn", which is the predominant form when VWF is isolated from blood [98]. As this form is not so extended, it is presumably smaller VWF strings in the absence of shear, where the sites for platelet binding and cleavage are occluded to allow free circulation of the VWF.

1.1.3 Von Willebrand disease

Von Willebrand disease is estimated to be the most common inherited bleeding disorder in humans, however estimates of prevalence are variable. A recent study [8] evaluated the prevalence at 1 in 1000, but previous studies have put it at between 1 in 100 and 1 in 10,000 [6, 89], depending on the measuring method used.

VWD is divided into three main types [92]:

- type 1; a partial quantitative deficiency in VWF levels
- type 2; qualitative deficiency in VWF levels, which can be broken down further into 4 sub-types

  - type 2A; selective absence of the largest, most biologically active multimers
  - type 2B; increased affinity for GpIbα leads to increased platelet binding and subsequent clearance of VWF
  - type 2M; decreased affinity for GpIbα leading to present but ineffective VWF
  - type 2N; decreased affinity for Factor VIII leading to present but ineffective VWF
- type 3; an almost total loss of VWF

A database of disease-causing mutations is maintained at *http://www.vwf.group.shef.ac.uk* [39].

The mechanism and structural basis for the phenotype of some mutants have been investigated [126, 125, 132]. Disease-causing mutations reflect the importance (as in section 1.1.2) of the A2 domain in regulating VWF cleavage by ADAMTS13 as mutations here can render VWF more susceptible to proteolysis and cause type 2A disease by cleaving the largest multimers [132]. Investigation of mutations interupting disulphide bond formation and causing types 1 and 3 VWD show defects in formation of WPBs resulting in ER retention and formation of round WPBs with fewer and shorter VWF tubules [126].

1.1.4 Weibel-Palade body exocytosis machinery and mechanisms

Weibel-Palade body exocytosis must be carefully regulated as the high-molecular weight VWF multimers they contain are very haemostatically active. WPBs are secreted in response to rising concentrations of either Ca^{2+}or cAMP, with both pathways giving rise to a distinct exocytotic profile and with different effects on the cytoskeleton [118]. Compounds that raise the intracellular Ca^{2+}concentration, such as histamine or ionomycin, release WPBs from both perinuclear and peripheral regions of the cell. cAMP-raising compounds, such as forskolin, release fewer WPBs and only from the

cell periphery. These different release patterns also coincide with different patterns of cytoskeletal reorganisation, indicating a role for actin and microtubules in WPB exocytosis [118].

Long-range movement of WPBs to the cell periphery is achieved by microtubules [60], which explains why microtubule deploymerisation affects Ca^{2+}-evoked secretion of perinuclear WPBs [118]. Short-range 'diffusive' movements at the cell periphery are attributed to both microtubules and actin. The short-range movements are smaller than would be expected for free diffusion of the WPBs, indicating a tethering process occurs to hold WPBs at the cell edge [60].

WPBs move towards the cell membrane in a maturation and Rab27a-dependent manner [40, 73], whereby mature granules are Rab27a-positive and are anchored at the cell periphery. Acquisition of Rab27a allows the WPB to interact with MyRIP (myosin and Rab27a interacting protein) and MyoVa (myosin Va) and together these proteins anchor WPBs to cortical actin at the cell periphery [73, 85]. Anchoring WPBs to cortical actin provides a "ready releaseable pool" of VWF at the cell edge and ready for exocytosis and inhibits release of immature WPBs [73].

The WPB tethering role of the Rab27a-MyoVa-MyRIP complex to actin has been probed in numerous experiments, and if any member is missing; Rab27a [73], MyoVa [85], MyRIP [73] or the cortical actin itself [118] then secretion is increased.

Membrane fusion between vesicles and the plasma membrane requires the interaction of SNARE (soluble NSF attachment protein receptor) proteins on each membrane and a soluble cytosolic SM protein [105]. SNARE proteins reside on both vesicle membranes and their target membranes (in this case the plasma membrane) and when active bring together both membranes and provide the energy required to fuse membranes. This is done by the 'zipping' together of four helices, 3 from the t-SNARE (plasma membrane) and 1 from the v-SNARE (WPB) to form an 4-helix bundle, known as a trans-SNARE complex (figure 6). It is the combination of SNARE complex constituents and SM proteins that ensures only the correct vesicles fuse and

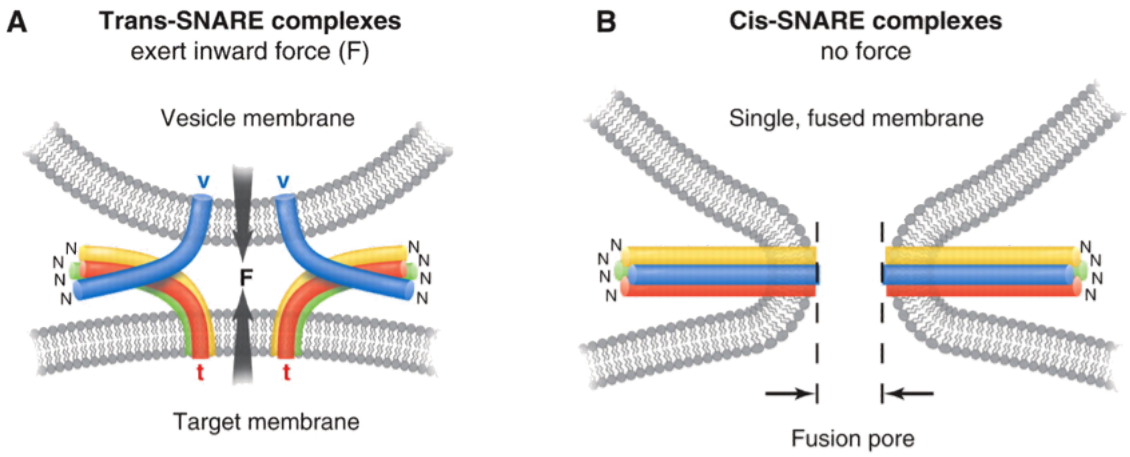

Figure 6: **A** Formation of a trans-SNARE complex. 3 helices from the t-SNARE and 1 from the v-SNARE 'zip' together to form a 4 helix bundle. This brings the vesicle and plasma membrane into close apposition and provides the energy from pore formation. **B** Fully 'zipped' cis-SNARE complex with open fusion pore. From [105]. Reprinted with permisstion from AAAS.

the energy liberated by formation of trans-SNARE complexes drive fusion.

Two v-SNARE proteins, VAMP3 and VAMP8 (vesicle associated membrane protein, table 1), have been identified as co-localising with WPBs [84]. Of these v-SNAREs, VAMP3 has been shown to form a complex with the plasma membrane t-SNARE proteins syntaxin 4 and SNAP23 in endothelial cells [84]. Therefore it is likely that these are three of the trans-SNARE complex components responsible for membrane fusion during WPB exocytosis. To complete the trans-SNARE complex, the SM protein involved in WPB exocytosis is thought to be Munc18c [33].

A second SNARE system is also involved in WPB release, comprising STXBP1 (syntaxin binding protein 1 or Munc18-1), Slp4-a (synaptotagmin-like protein 4-a or granulphilin) with syntaxin-2 or -3 [111]. Slp4-a is another Rab27a effector protein, and is a positive regulator of exocytosis [5]. A third Rab27a effector protein is Munc13-4. Munc13-4 is a positive regulator of WPB exocytosis, acting through both Rab27a and Rab15 [140]. The presence of Rab15 on a secretory organelle is unusual as it is an endocytic Rab. This may reflect the status of WPBs as both lysosome-related organelles and secretory storage granules. Release or retention of

a given WPB is therefore controlled by shifting the equilibrium between these three positive and negative exocytosis effectors of Rab27a and Rab15.

Once the membrane has fused, there may be a further role for actin in expelling the VWF contents. An actomyosin ring has been proposed to form and localise to WPBs during exocytosis and help 'push' the VWF away from the cell [74, 72]. Such an actin structure around a fusing WPB has not been seen by cryo-EM ([4], in section 1.1.5, figure 7). The unfurling effect thought to be created by pH change ([68, 47], section 1.1.5) in combination with the elongational flow from blood whilst VWF is still attached to the cell [103] also contribute to expanding VWF from tubules to strings and expelling it from the cell.

There may also be multiple modes of WPB exocytosis. Selective exocytosis allows vesicles with multiple components, such as WPBs, to release some components but not others. In WPBs this allows both secretion of soluble proteins, such as IL-8, and delivers membrane proteins from WPB to plasma membrane [2], whilst retaining the main VWF cargo. Once WPBs are exposed to the extracellular environment, in particular pH, VWF tubules unfurl ([68, 47], section 1.1.5) leading to round WPBs without VWF tubules. As WPBs undergoing a 'lingering kiss'-type exocytosis also become round [2], it is possible that they also contain unfurled VWF.

Compound exocytosis means vesicles fuse with each other as well as the plasma membrane in the process of being released. WPBs may undergo a sub-type of compound exocytosis called multigranular exocytosis [110]. In this model, 6-7 WPBs undergo homotypic fusion to form a 'secretory pod', a larger, membrane-enclosed space containing VWF 'dots', where the VWF no longer consists of regular tubules, and are secreted as a mass [110, 70].

Both of these alternative modes of WPB exocytosis require the VWF tubules to be exposed to extracellular, neutral pH prior to release. Exposure to neutral pH breaks down VWF tubules by disrupting the non-covalent interaction between proregion and the mature VWF multimer [47, 68]. There is some uncertainty about whether VWF

unfurled pre-release can form strings upon release. Originally, it was thought that only tubular VWF is capable of forming VWF strings upon release [68], suggesting that the fate and function of post-lingering kiss WPBs was not the same as unreleased WPBs and was unknown. The VWF 'dots' in the homotypic fusion would be in a similar situation without tubules. However in a flow chamber, exposing the secreted VWF masses to subsequent flow causes them to form strings [70], and during constant flow there is a lag between secretion as a mass and string formation. This suggests that strings can form from a mass rather than solely from tubules, under the influence of flow, such as in a blood vessel.

1.1.5 Structural changes of WPBs during exocytosis

As VWF undergoes a large structural change upon secretion (section 1.1.2), so must the limiting membrane of WPBs. Immediately after pore formation, WPBs round up into a spherical shape [26]. As the characteristic rod-shape of WPBs is due to their tubular cargo [109, 4], the transition to a spherical demonstrates a loss of VWF tubules after exposure to blood (section 1.1.2).

A superficially similar rounding up effect can be achieved by treatment with monensin, NH_4Cl or chloroquine for 60 minutes, which breaks down the pH gradient and causes granules to round up by light microscopy [68]. EM of monensin treated cells shows round WPBs without VWF tubules [68]. This confirms not only the effect of pH on VWF tubules but the subsequent effect the VWF tubules have on the overall WPB shape.

Rounded up WPBs have also been imaged by cryo-electron tomography without any prior stimulation (figure 7, [4]), likely to be a basal secretion event [37]. The rounded, marrow-shaped appearance together with the membrane connection (figure 7, black arrow) and the distortion to the helical pattern in the Fourier transform suggest that this granule is at a stage of secretion where the VWF tubules are in the process of breaking down and presumably unfurling. The putative fusion pore has

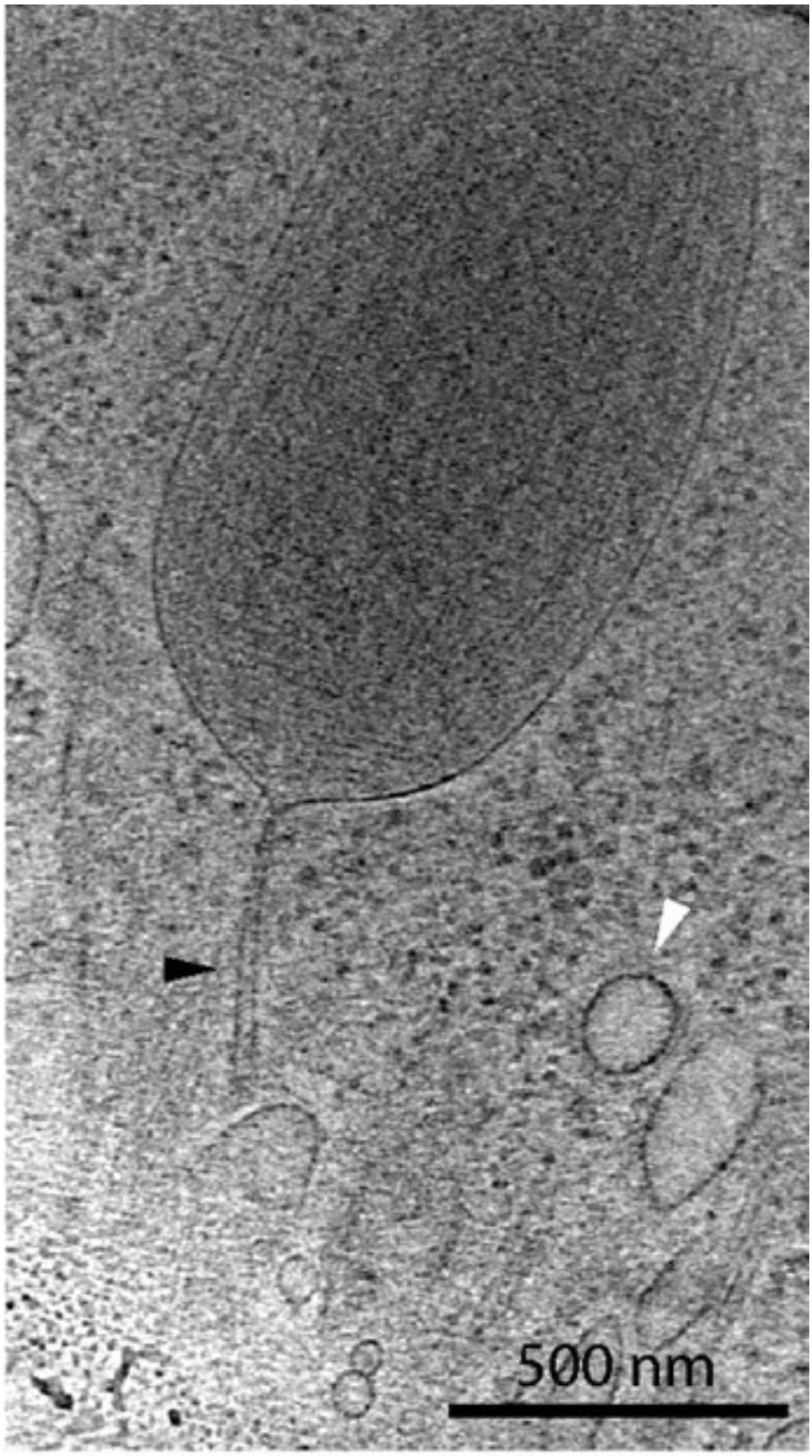

Figure 7: Slice through a tomogram showing a rounded, marrow-shaped WPB with stem-like connection to the plasma membrane (black arrow). A coated vesicle is also shown (white arrow). From [4].

a narrow, 'stalk' like appearance, suggesting the VWF content must pass through a width restriction rather than the total collapse of the WPB.

1.2 Cryo-electron microscopy

1.2.1 Introduction to cellular cryo-EM

Cryo-electron microscopy (cryo-EM) can be used to study many biological specimens (macromolecular assemblies, viruses and cells) in a frozen-hydrated state. The specimen must be preserved before entering the microscope in order to withstand the high vacuum within the column of the electron microscope. By keeping the specimen in a frozen-hydrated state, it is both protected from the harsh conditions of the microscope and imaged in the biologically relevant vitreous state, rather than a negative stained and dried, or plastic-embedded state.

Whilst the electron microscope has existed for over 80 years, the invention of which earnt Ernst Ruska the Nobel Prize in Physics in 1986 [90], the field of high-resolution biological EM was advanced by the development of methods to freeze the sample within a thin film of vitreous ice [24], as opposed the crystalline ice formed by slower freezing procedures. Consequently, the structural damage in the sample caused by ice crystal growth is eliminated. During imaging, the sample is maintained below the devitrification temperature by a thermal connection to an external Dewar of liquid nitrogen.

Images in the electron microscope are formed by electrons passing through the specimen, interacting with it and being detected by film, CCD or more recently by direct electron detectors. In this way, the beam path is similar to that in a light microscope. The interactions between electrons and sample can be classified as one of two types; elastic scattering or inelastic scattering.

Elastic scattering means that the electrons interact with atomic nuclei within the sample and undergo a change in direction with no loss of energy. It is these electrons that form the image. Inelastic scattering means that the beam electrons interact

with atomic electrons from the sample. This interaction causes the beam electrons to lose energy to the sample. Inelastic scattering is problematic in two ways; energy transmitted to the sample manifests as radiation damage and as these electrons have lost energy, they don't come to focus in the image plane, instead adding noise to the image. Energy filters aim to eliminate those electrons from the final image, increasing its contrast [96], however they still interact with the sample, contributing to the dose it receives and thus the radiation damage.

In the case of frozen-hydrated biological specimens, the low molecular weight atoms of ice and organic materials only weakly scatter electrons, yielding a low angular distribution. Low angular scattering gives limited oppotunities for an objective aperture to remove those electrons from the image and generate amplitude contrast. Instead, most contrast is contributed by the phase change of the electrons with the sample. Phase change itself cannot be measured, instead the contrast is formed by the relative phase shift between those electrons that did not interact with the sample and those that did. The difference between the phase of the unscattered electrons and the interacting electrons is a function of the spherical abberation of the lens system, the accelerating voltage of the electron gun and the defocus of the objective lens. This function is known as the contrast transfer function (CTF). As the focus value is set by the operator, the contrast of a given spatial frequency is operator determined and can be changed depending on the experimental requirements. A focus series, where the same field of view is imaged with multiple focus values, can be used to increase the information captured. Changing the defocus alters the frequencies at which there is no signal and the frequencies where signal is highest; a highly defocussed image gives mainly low-resolution contrast and an image closer to focus includes more high-resolution contrast.

An alternative to generating contrast by defocusing the electron beam is the use of a phase plate. This may take the form of a uniform, thin carbon film with a central hole, placed in the back-focal plane of the objective lens [15]. The unscattered

electrons will pass through the central hole, whereas the scattered electrons must pass through the carbon film. The scattered electrons will therefore undergo a phase shift compared to the unscattered electrons, creating contrast. This technique has already been used for in-focus cryo-electron tomography of whole mounted frozen cells [34], although its use is not routine due to various challenges such as the fabrication and longevity of the phase plates [14].

1.2.2 Vitrification and imaging of whole cells

Techniques such as negative staining and freeze-drying, where the sample is dehydrated, are known to induce crushing and collapse of the structures [42, 51]. Cryo-sectioning, where a sample is frozen in a vitreous state and subsequently sectioned using a cryo-ultramicrotome, also introduces artifacts from imperfect cutting, such as cravasses and knife chatter [23]. With a dual beam microscope containing a scanning electron microscope (SEM) and focussed-ion beam (FIB), areas of sample can be removed by the FIB, making areas that were too thick to image into possible areas for investigation, whilst avoiding some of the artifacts associated with cryo-sectioning [88].

It remains true that vitrification alone leads to the closest to native preservation of biological materials, although it is not without its own disadvantages. In the case of cells, particularly mammalian cells, the primary problem is sample thickness. Thick samples such as whole cells present two problems; achieving complete vitrification, because as the sample thickness increases, so does distance from the cryogen, decreasing the cooling rate and secondly, the transmission of electrons through the sample becomes much less likely as multiple scattering events become more common. High-pressure freezing can solve the problem of acheiving vitrification for thicker samples, but the problem of imaging the sample without cryo-sectioning still remains. For tomography, where effective sample thickness increases with tilt angle, there is great pressure to reduce sample thickness. Therefore, imaging of whole cells is restricted

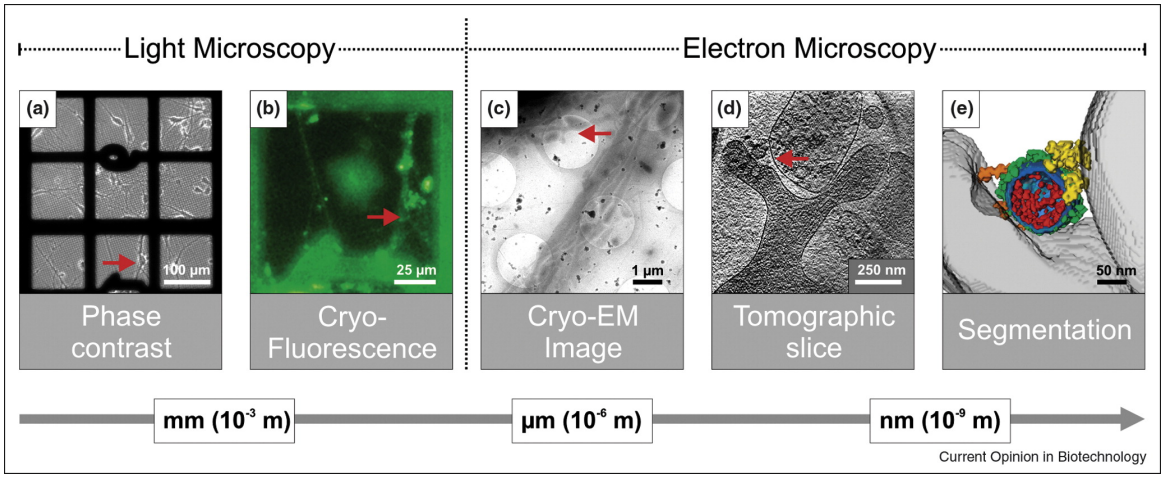

Figure 8: Overview of a correlative microscopy experiment. The experiment progresses from left-to-right; locating an individual neuronal cell and subsequently imaging individual processes within it. Reprinted from [81], with permission from Elsevier.

to the thin edges of spread, flat cells, such as HUVECs [4], *Dictyostelium discoideum* [65], PtK2 cells [34] and Goldfish fin fibroblasts [107], where sample thicknesses in each case are estimated to be under 600 nm, and as low as 100 nm in some cases.

1.2.3 Correlative light-electron microscopy

Correlative light and electron microscopy (CLEM) images the same sample using both light and electron microscopes, in order to combine the advantages of both methods. Generally this means combining fluorescence microscopy with its ability to specifically label proteins by genetic tags or immunocytochemistry, with the high resolution imaging from the electron microscope [9]. Combination of electron microscopy with phase-contrast light microscopy can also be useful in both providing an overview of unlabelled areas of the specimen and, in the case of cryo-light microscopy, assessing the quality of sample preparation and freezing [56]. An overview of the correlative process is shown in figure 8.

By harnessing the power of fluorescent labelling, CLEM can help with two different but related challenges in cellular electron microscopy; locating objects of interest and identifying them. Given the limited field of view in a typical EM experiment compared

to the area of even a single cell, re-locating areas of interest can be challenging. Even after imaging the location of the object, identifying it within a crowded cell can be difficult unless it has known or prominent structure (such as the WPBs).

Imaging a single sample by both light and electron microscopy requires additional technical considerations about how to prepare the sample and transfer the sample between instruments, especially if one or both imaging methods are under cryo conditions. To this end, a number of devices for cryo-CLEM have been constructed. The first group of these modify a standard light microscope to accomodate a specimen at liquid nitrogen temperatures and maintain it there [93, 97, 112]. This sample can then be transferred to the electron microscope as in stand-alone EM. A second approach has been to install a light microscope objective within the column of the electron microscope, with the light path perpendicular to the electron path [1, 29]. This system can only be used for fluorescence or reflected light imaging as there is no transmitted light capability, but it does mean the sample only has to be loaded in a single instrument, eliminating extra handling of the cryo-specimen.

1.3 Cryo-electron tomography

1.3.1 Introduction to tomography

Cryo-electron tomography is an application of cryo-electron microscopy that allows 3D structures to be reconstructed from their 2D projections collected over an angular range (figure 9a). Electron micrographs can essentially be regarded as 2D projections because of the large depth of focus [44]. The power of cryo-ET lies in its ability to reconstruct single-copy, individual objects instead of using a homogeneous population of differently oriented copies to obtain views from different angles. In the biological context, this allows the study of large, unique objects such as organelles, viruses and the cytoskeleton.

In order to perfectly reconstruct a 3D object from projections, two conditions need to be satisfied: the volume must be identical in each projection and an infinite

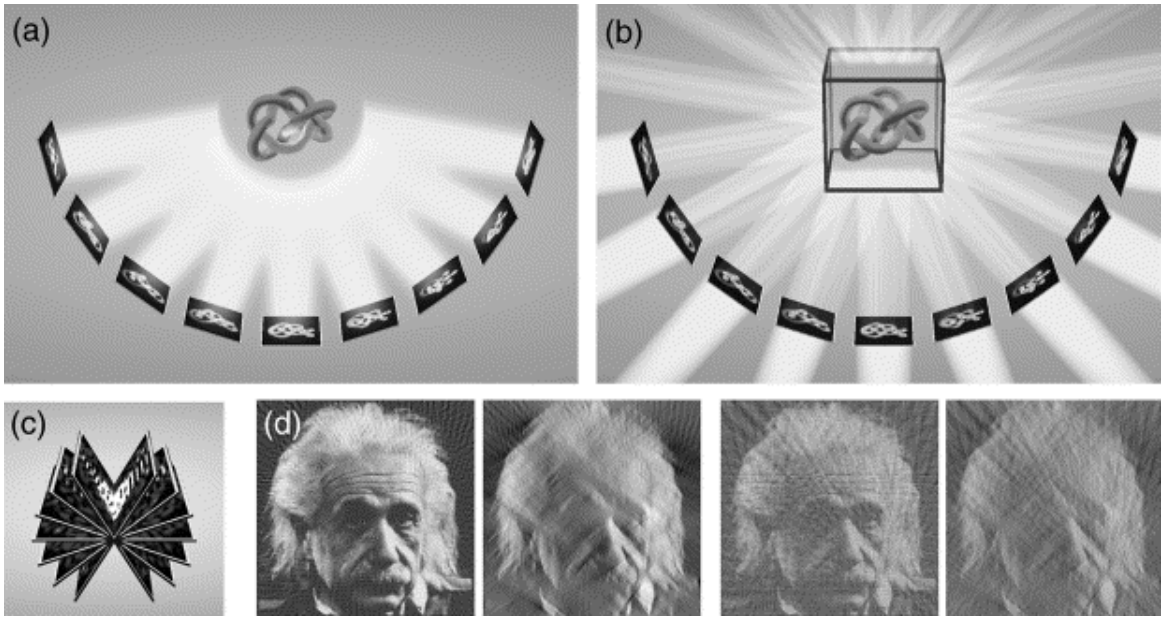

Figure 9: **A** Data acquisition of single-tilt series showing projections taken at different angles. **B** Calculation and summation of back-projection bodies to reconstruct the original object within the 3D volume. **C** Tilt-series transposed to Fourier space. The missing wedge can be seen at the top and bottom of the figure. **D** First image; $\pm 90^\circ$ with 2° increment. Second image; $\pm 60^\circ$ with 2° increment. Third image; $\pm 90^\circ$ with 5° increment. Fourth image; $\pm 60^\circ$ with 5° increment. Reprinted from [3], with permission from Elsevier.

number of projections must cover all possible orientations (±90°). In the electron microscope, neither of these are satisfied, which together with the noisy projections from the microscope, limit the resolution of the reconstruction. The projections are noisy due to the inelastically scattered electrons, which are not in the focal plane of the detector, and detector noise, inherent noise in measuring the signal. The volume is not identical in each image due to small stage translations whilst moving from angle to angle, and the accumulated dose over an experiment will also alter the sample via beam damage. A full angular range cannot be collected because of the increase in effective specimen thickness with angle. This change is given by the formula $thickness_{tilt} = thickness_{untilted}/\cos\theta$, where θ= tilt angle. The increase in thickness beyond the penetrating power of the electron beam combined with the geometry of the specimen cryo-holder limit the tilt angle to ~±70°. In the central slice theorem, the Fourier transform (FT) of each projection represents a slice through the origin of the 3D FT, shown in figure 9c. The uncollectable data from ±70°– ±90° forms a 'missing wedge', shown by the lack of a vertical slice in figure 9c, corresponding to the lack of a 90° tilted image. The consequence on the final reconstruction of not being able to collect projections covering the entire angular range is shown in 2D in figure 9d. In real space, the Fourier space 'missing wedge' manifests as resolution anisotropy, meaning that the point spread function is greater in the z-axis than in the x or y axes. This gives objects the appearance of being elongated and smeared in z.

The angular increment is limited because of the need to minimise the electron dose delivered to the sample, and thus minimise the radiation damage the sample develops during imaging. The total dose the sample can tolerate must therefore be rationed across all the exposures needed for the tilt series. Two conflicting needs must therefore be balanced; more images across the tilt-series will increase the amount of information in the reconstruction (more slices in Fourier space, figure 9c), but each image adds more dose to the sample. The dose in each individual image can also be reduced, but this will then reduce contrast, making the tilt series harder to process

and possibly introducing alignment errors. In the case of WPBs, they show signs of visible radiation damage after 85 $e^-/Å^2$ at 300 keV [4]. Tilt series with minimal dose to the sample can be collected automatically using programs such as SerialEM [63]. This ensures the region of interest is exposed to the minimal electron dose by carrying out all background procedures (eg. focussing and tracking) over other areas of the sample, thus delivering only the necessary imaging dose to the region of interest.

1.3.2 Data processing and tomogram generation

After tilt-series collection, the data is processed into a tomogram. This can broadly be described as a two-step process; alignment and reconstruction, and there are many software packages to carry out these procedures [10, 11, 46, 54, 62, 71, 130].

Alignment allows for correction of movement occuring during the data collection process, as the goniometer can often translate the stage in addition to moving about the tilt axis (section 1.3.1). For cryo-ET, this is most often done by adding spherical gold fiducials to the sample before freezing. The high molecular weight of the gold gives them good contrast in the images, making them easy to locate in each tilted image, and by marking known points in each image, they can be bought into registration. Fiducial-less alignment is also possible, in which case cross-correlation alone is used to align the images [10]. Fluctuations in the related parameters of defocus, magnification and eucentric height across the tilt-series and changes in the specimen from the beam all conspire to make the alignment process more problematic than at first glance.

After alignment, the tilt series must be reconstructed into a tomogram. A schematic for one method of reconstruction, back-projection, is shown in figure 9b. This can either be thought of in Fourier space, due to the central slice theorem as in section 1.3.1, where the FT of each aligned slice intersect on a line through the centre of the 3D FT, or in real space. In real space, as in figure 9b, the density from each projection in 'smeared' linearly through the 3D box that will be the reconstruction, at the angle at

which the projection was taken at - quite literally projected backwards. By summing up as many 'smeared' projections as possible, an reconstruction of the object is built up. The effect of various sampling intervals for these 'smeared' projections is shown for the 2D case in figure 9d.

Another commonly used reconstruction algorithm is SIRT (simultaneous iterative reconstruction technique, [38]). This algorithm iteratively changes a starting model to improve the reconstruction, comparing model reprojections to the original projections to calculate the required changes. The algorithm is 'simultaneous' as it considers all projections at once, rather than on a sequential, projection-by-projection basis, before making the required changes to the model. This process of comparing and changing continues until the projections and reprojections converge.

1.3.3 Interpretation and analysis of reconstructions

Once a reconstruction has been calculated, the next step is to interpret the data for biological conclusions. Tomograms are generally interpreted and further processed in two ways; segmentation or sub-tomogram averaging. This must be done carefully, being mindful of the possible artefacts introduced during calculation, such as the resolution anisotropy in the z-axis.

Segmentation is the process of assigning voxels as belonging to a particular structure. For example, in a cellular context, all voxels making up a mitochondria or within a membrane-enclosed space might be segmented. Building up models of tomogram contents allows us to calculate volume or look at the overall shape of a complicated structure that is not clear from 2D slices alone, as well as the interaction between different objects.

Subtomogram averaging is analogous to the single particle analysis approach of using extracted individual projections to calculate a 3D structure, but rather than averaging projections, 3D volumes of identical copies of a complex are extracted from a tomogram and averaged together. As the extracted particles are already three-

dimensional, this approach does not require the *ab initio* determination of the angles between projections, however it does require three-dimensional alignment of the extracted volumes. The advantage of this over single-particle analysis is that subtomogram averaging can deal with calculating structures without extraction or purification of the sample, for example, extracting ribosomes from within a tomogram of a whole cell, or ATP synthase molecules from mitochondrial cristae [16].

1.4 Aims for this project

The overall aim for this project is to image and understand the shape change of WPBs during exocytosis, and how the VWF tubules within them change; both in their distribution and structure. Electron tomography of frozen-hydrated, whole mount HUVECs will be used as it is the only technique which enables both the overall WPB shape and the 3D distribution of VWF within WPBs to be ascertained. In order to obtain images of different WPB shapes, several approaches will be taken.

Firstly, HUVECs that are releasing their WPBs will be frozen and imaged, looking for WPBs mid-fusion. This requires determination of the parameters for stimulation and release of WPBs from HUVECs so that cells are frozen with the greatest possible number of fusion events occuring. Images of WPBs mid-release will show the WPB fusion pore and disassembly of VWF tubules into strings.

Fluoresence microscopy experiments from other human endothelial cell lines show that these cells endogenously synthesise round WPBs. Images of these rounded WPBs, particularly the state of their VWF cargo may show similarities to WPBs rounded before fusion. The presence of VWF tubules in these cells would demonstrate that whilst tubules are necessary for WPB elongation, they may not be the sole factor determining WPB length.

WPBs within HUVECs can be forced to become round by altering the internal pH of the WPBs. Subjecting the cells to hypotonic stress also causes the WPB to become round, and the WPBs can not recover when subsequently returned to cell

growth media. Similar to the WPBs from other cell lines, artifically rounded WPBs give an insight into the different shapes and structures WPBs can take. Understanding the possible different WPBs shapes and VWF distributions will help interpret events at the fusion pore.

The final two chapters of the thesis deal with an observation made whilst collecting data on WPB shape; that some WPBs contain a membrane-enclosed vesicle in addition to their WPB cargo. Experiments to find out the content and prevalance of this vesicle were then conducted, and the development of a sample preparation method which would immobilise the WPBs before plunge-freezing in order to carry out light microscopy experiments for correlative light and electron microscopy experiments.

2 Materials and Methods

2.1 Preparation of grids for EM

Gold Quantifoil (Quantifoil Micro Tools) or C-flat (Protochips) grids of various mesh sizes were examined by light microscopy to check integrity. Some had additional carbon added (using an Emitech K950X (Quorum Technologies)) and all were glow discharged (25 mA, 30 seconds using an Emitech K100X). When indicated, grids were pre-washed with ethyl acetate before having additional carbon added, to remove any residual plastic from the fabrication process. Some grids were also incubated at room temperature with 70-150 kDa poly-lysine hydrobromide (Sigma-Aldrich), 0.1 mg/ml for 30 minutes.

2.2 Cell culture and transfection

HUVECs (Human umbilical vein endothelial cells, PromoCell) were cultured in M199 (Invitrogen) supplemented with 20 % fetal calf serum, 50 µg/ml gentamicin, 30 µg/ml endothelial cell growth supplement and 10 U/ml heparin at 37°C and 5 % CO_2. Cells were trypsinised and reseeded at different densities (mostly ~50,000 cells/ml) into 35 mm tissue culture dishes (Nunc). Immediately following this, prepared EM grids were inserted, carbon-side up into the tissue culture dishes and cells grown on the grids overnight [4].

For live-cell imaging, HUVECs were transfected with proregion-EGFP (as in [41], pEGFP-N2 (Clontech) from the group of Dr Tom Carter) using the Amaxa HUVEC Nucleofection system (Lonza).

HHMECs (human heart microvasculature endothelial cells) were cultured using the same procedures as for HUVECs. The cells were obtained as described in [64, 66].

2.3 Freezing grids for electron microscopy

Grids with cells grown on them were removed from the culture media and washed briefly in PBS. Grids were frozen by plunging into liquid ethane using either a manual plunge-freezer or an FEI Vitrobot Mark III (FEI Company). Grids frozen on the manual plunger were frozen under room temperature and humidity and blotted from the front with filter paper by hand. Those frozen on the Vitrobot were subjected to various conditions for initial experiments, using the built-in environment chamber which controls for temperature and humidity. The final protocol used room temperature (with the chamber set to 22°C) and room humidity (with the humidifer switched off). Room conditions were used in order to make the Vitrobot and manual plunge-freezer experiments directly comparable. The Vitrobot automated the blotting procedure and grids were blotted for various durations from both sides using a double layer of filter paper. Once frozen the grids were placed in liquid N_2 for storage until needed.

When indicated, 4 µl 40 % protein A conjugated 10 nm gold colloid (BBI Life Sciences) in PBS was added between washing and blotting to act as fiducial markers. For stimulation of WPB exocytosis, the stimulant was mixed with the fiducial markers to total 4 µl and added at the same point. Stimulants used were 300 nM ionomycin, 1 µM ionomycin (*Streptomyces conglobatus*, Sigma) or 100 µM histamine dihydrochloride (Sigma) in PBS.

2.4 Fixing grids for electron microscopy

Grids for imaging fixed HUVECs were prepared as in section 2.1 and section 2.2. Cells were fixed in 3 % PFA (paraformaldehyde) for 15 minutes and washed with PBS, as for immunofluoresence (section 2.7). Initial experiments continued with the immunofluorescence protocol and permeabilised with 50 mM NH_4Cl and 0.2 % saponin in PBS, also for 15 minutes (section 2.7), however this was unsucessful (Chapter 6) and discontinued. An experiment using 2 % gluteraldehyde in PBS for fixation was

also done, incubated at 4°C overnight. Post-fixation, grids were kept hydrated in PBS until freezing. The grids were frozen as per live-cell grids in section 2.3, however initial experiments indicated that fixed grids required considerably shorter blotting times.

2.5 Electron microscopy

Frozen grids were imaged using either a Spirit TWIN microscope (FEI) operating at 120 kV and equipped with an Eagle 2k camera (FEI) using a Gatan 626 cryo-tomography holder or a LN_2 cooled Polara microscope (FEI) operating at 200 kV and equipped with a F224 CCD camera (TVIPS). Both TIA (FEI) and SerialEM [63] image acquisition software were used, and low-dose procedures were used in both packages. SerialEM was used to collect whole grid montages at ~140x magnification, which were used for locating areas of interest for further imaging using low-dose procedures.

Single-axis tilt-series were collected automatically using SerialEM, with an angular range of –60° – +60° and increment of 2° or 3°. Total dose for tilt-series were limited to 50 – 70 e^-/A^2, giving individual images with a dose of 1.2 – 1.7 e^-/A^2. The dose per image was kept constant for each tilt angle in a series. The target defocus was set at -8 µm.

2.6 EM image processing

2.6.1 Tomographic processing and analysis

Tilt-series were processed using Etomo from the IMOD package [54, 62]. Images were aligned using cross-correlation followed by manual tracking of fiducials. Initial reconstructions were calculated using back projection and subsequently using the SIRT method available within Etomo. Volumes were viewed and exported for use in figures and movies using IMOD and ImageJ (*http://www.rsb.info.nih.gov/ij*).

Amira (FEI Visualization Sciences Group, [104]) and IMOD were used to generate

3D models. VWF tubules were manually traced in IMOD, using both XY and cross-section views to find the centre in 3D at each point (start, end and intermediate kinks). Tubules were modelled as individual contours in IMOD; straight sections joined by kinks. Analysis of the distances between tubules in the VWF tubule models used MATLAB (MathWorks) scripts provided by Dr Sebastian Wasilewski [4].

2.6.2 2D image analysis

Measurements of granule lengths and widths were made using IMOD [54] and analysed using Prism 6 (Graphpad). Granule length was measured as the maximum length along the axis of the VWF filaments. The width was measured as perpendicular to this, ignoring any perturbations such as clubbed ends, internal vesicles and fork points. The length and width distributions for each condition were compared using Welch's t-test for populations with unequal variances.

Simple image processing tasks such as crop, pad and rotate were performed in Ximdisp [99], and FFT calculations were performed using Ximdisp and fftrans from the MRC suite [13] and fftavg from EMAN [58]. Figures were prepared using Photoshop CS4 (Adobe).

2.6.3 Calculation of a VWF tubule structure

VWF tubules were cut from tomograms as a cylinder with radius of 31 nm (20 px) using the program Cylinder (provided by Dr Sebastian Wasilewski) and projected to give a 2D image. Each projection was boxed into a 40×40 px box using the EMAN program Boxer [58]. A reconstruction was calculated using the IHRSR algorithm [25], using the image processing programs IMAGIC-5 [113] and Tigris (Dr Tim Grant).

Briefly, a random γ angle was assigned to each projection to create an initial 3D model. The model was symmetrised using the parameters found in [4]. Reprojections of this initial model were used as references for multi-reference alignment, in order to assign new angles to the projections. The updated angles were used to calculate a new

3D model and a new symmetry searched for. The new symmetry was imposed and reprojections calculated. This process could then be iterated; projection matching, calculate new 3D model, search and impose symmetry. Surfaces were viewed using UCSF Chimera [79].

2.7 Immunocytochemistry and imaging

Cells were cultured onto grids as in section 2.2 or on to 9 mm glass coverslips coated in 1 % gelatin (porcine skin gelatin, Sigma). The cells were then fixed in 3 % paraformaldehyde (PFA) for 15 mins before being permeabilised and quenched using 50 mM NH_4Cl and 0.2 % saponin in PBS, also for 15 mins. The cells were washed in a PGAS buffer (0.2 % gelatin, 0.02 % saponin, 0.02 % NaN_3 in PBS) before applying the primary antibody. The primary antibody used was rabbit anti-VWF at a dilution of 1:10000, incubated at room temperature for 1 hour. A fluorescently-conjugated wheatgerm agglutinin was used with the secondary antibodies to delineate the plasma membrane of the cells. Secondary antibody incubation was for 30 minutes in a dark environment at room temperature. Coverslips and EM grids were mounted onto slides using Mowiol (Harco). The slides were imaged using 10x HC PL APO 0.4 dry, 40x PL APO 1.25 oil and 100x HCX PL APO CS 1.40 oil objectives on a Leica SP1 and SP2 confocal system.

For seeding density and timecourse experiments (section 3.2), VWF was labelled using a rabbit anti-VWF antibody at a dilution of 1:10000 for 1 hour, followed by Cy2 anti-rabbit secondary antibody at a dilution of 1:100 for 30 minutes in a dark environment. DAPI and a fluorescent wheatgerm agglutinin (dilution 1:200) were also mixed in with the secondary antibody as markers for the nucleus and cell membrane respectively. A 20x montage of each grid was made, with 5 – 7 Z-sections in all 3 channels, using an Olympus VS120 slide scanner. Using ImageJ, a macro was written that extracted the DAPI channel and calculated a max projection. After manual thresholding, the macro converted the image to binary, applied a watershed function

and counted the number of nuclei and therefore cells per grid.

In order to count granules per cell in the seeding density and timecourse experiments, 40x Z stacks of 4 cells on each grid were collected. Granules were counted by first calculating a maximum projection for both channels and manually determining the extent of a single cell, using the membrane dye and the extent of the granule population. From a single cell, granules were counted in the same way as nuclei above; thresholding, binarising and applying a watershed function and counting all the objects.

2.8 Live-cell imaging and analysis

Grids were placed into cell medium containing cells that had been nucleofected with proregion-EGFP (according to manufacturer's instructions, as [41]. pEGFP-N2 (Clontech) from the group of Dr Tom Carter) and grown as above. After 24 hours, the grids were placed into a 35 mm glass-bottomed dish (MatTek Corporation) with 1 ml physiological saline (140 mM NaCl, 5 mM KCl, 1.8 mM $CaCl_2$ 2 mM $MgCl_2$, 10 mM HEPES-NaOH, 10 mM glucose, pH 7.4) and imaged by wide-field fluorescence microscopy on an Olympus IX70 inverted microscope/DeltaVision system (Applied Precision Inc.). Preliminary experiments included cells incubated in the dark with 0.1 µM Fura Red (Molecular Probes) in physiological saline for 20 minutes before washing away excess dye with physiological saline and imaging. Fura Red is a calcium-sensitive dye, showing the frame at which intracellular calcium levels rose.

The microscope was contained in an incubation chamber allowing the temperature to be controlled to 32°C – the minimum controllable temperature. However, before being moved to the microscope chamber, cells and saline solution were kept at 27°C. 27°C was chosen as the target temperature for stimulation because previous reports [45] have shown that ionomycin applied at this temperature will slow down exocytosis events to a time range that will be accessible by plunge-freezing experiments, whilst still maximising the extent of degranulation. This temperature is also close to room

temperature, so the results are relevant when using a manual-plunge freezer with an uncontrolled environment for manual plunge-freezing experiments or the Vitrobot when set to 22°C for room temperature.

HUVECs were stimulated to release WPBs using 300 nM ionomycin, 1 µM ionomycin (*Streptomyces conglobatus*, Sigma) or 100 µM histamine dihydrochloride (Sigma) in physiological saline. Stimulation was delivered in 50 µl from a pipette, into the dish containing the grid and saline solution, to achieve the desired final concentration. In addition to the stimulant, this solution also contained 0.5 µM Alexa 647 (Cy5) dye (Molecular Probes), in order to visually indicate the moment of stimulant addition in the recorded stacks.

Images were acquired using a QuantEM 512SC EMCCD (Photometrics) driven by Softworx imaging software (Applied Precision Inc.). Images were collected using a 100x PLANAPO 1.4 oil objective.

Multi-channel stacks were separated using ImageJ and granules tracked using the plug-in Speckle TrackerJ [100]. The increase in EGFP fluorescence corresponds to the fusion pore opening [26] and so the first frame this occurs in is taken as the moment of fusion. The times of these frames for each exocytic event were extracted and analysed in Prism 6 (Graphpad).

2.9 Inducing round granules

Cells were cultured as in section 2.2. After 24 hours, cells were given a hypotonic shock by incubating with 0.1x PBS (a 10-fold dilution in distilled water) for time periods ranging from 0.5 to 20 minutes. The cells were allowed to recover in fresh, pre-warmed media in a 37°C, 5 % CO_2 incubator for 2 hours before proceeding with either freezing for cryo-EM or immunocytochemistry.

In fluoresence experiments, the cells were stained with anti-VWF and wheatgerm agglutinin as in section 2.7. Images were collected using a Leica SP2 confocal microscope using a 100x HCX PL APO CS 1.40 oil objective lens. 6 exposures were

averaged for each image, and images were collected at 5 z heights per location in each channel.

Images were processed in ImageJ. The VWF channel was extracted and maximum projection of the 5 z heights calculated. The resulting image was thresholded to remove the background of perinuclear VWF within the ER but leave the WPBs. This was determined individually for each image. The '*Analyse particles*' command was used to report on all objects with an area $\geq 10\,\mathrm{px}^2$, and output their circularity. The average circularity of all counted objects in the field of view was used as the value for that condition.

2.10 Correlative light and electron microscopy

2.10.1 Sample preparation

Quantifoil Au Finder NH2 R2/2 grids were prepared for correlative experiments as in section 2.1, with additional carbon deposited and 30 s, 25 mA glow discharge. Cells were cultured as in section 2.2 and nucleofected with EGFP-CD63 (as in [2], pEGFP-C2 (Clontech) from the group of Dr Tom Carter) or CFP-CD63 (recloned from the EGFP variant in the lab of Dr Tom Carter). Cells were fixed but not permeabilised, as in section 2.4 and incubated with 1:2000 DAPI for 5 minutes. Grids were transferred cell-side-down to 35 mm glass-bottomed dishes (MatTek Corporation) containing 2.5 ml PBS for imaging.

2.10.2 Light microscopy imaging

Grids were imaged using procedures adapted from imaging live-cells on grids (section 2.8), as the cells remained hydrated in PBS throughout. The imaging strategy was to capture 10x magnification DAPI and phase contrast montages of complete grids, using an Olympus 10x 0.4 UPLANAPO Ph1 lens. These gave an overview of the EM grid for determination of its orientation and size and location of cells for further imaging.

Cells of interest were subsequently imaged at 100x magnifcation, collecting DAPI, EGFP/CFP and phase contrast images of all grids squares with well spread cells. Images were collected using an Olympus 100x 0.5–1.35 UPLANAPO Ph3 lens.

2.10.3 Electron microscopy imaging

EM procedures were similar to the standard procedures in section 2.5. An addition was to take an intermediate magnification montage, nominal magnification 2700x of a single grid square, using SerialEM [63].

2.10.4 Correlation and image processing

ImageJ was used to assemble and overlay the 10x DAPI and phase contrast montages, using a macro provided by Andrew Howe.

Low magnification EM images and intermediate magnification images were blended into single montaged images using the etomo command *'blendmont'* [62] for comparison with the 100x images from section 2.10.2.

The FFTs of the EM montage and the phase contrast microscopy images were used to calculate the scale factor and rotation angle between the images. The phase contrast light microscopy images was extracted in ImageJ and converted to IMAGIC format for calculation of the FFT. The EM montage was cropped to the same size as phase contrast image (512×512 px), in order to give a comparable FFT, and converted to IMAGIC format. FFTs were calculated and displayed in IMAGIC-5. Peaks in the FFT arising from the repeating pattern of the Quantifoil holey carbon film were used to calculate the scale and rotation factors. Measurements of distance and angle were made using GIMP (GNU Image Manipulation Program, *http://www.gimp.org*).

Scaling and rotation tranformations were made to the EM image to bring it into registration with the unaltered light microscopy images. Transformations and subsequent overlay images were made using GIMP.

3 Growth and stimulation of HUVECs on holey carbon supports for cryo-electron microscopy

3.1 Introduction

The first step for the project was to establish a protocol for reliably culturing HUVECs onto EM grids for imaging. A previous study in the lab [4] had sucessfully prepared HUVECs for cryo-EM, so that protocol was used as the starting point for the experiments in this chapter. Other cell lines have also been sucessfully vitrified and imaged whole-mount, as discussed in the introduction, section 1.2.2.

The rate of WPB exocytosis from HUVECs in response to ionomycin and histamine and at different temperatures has been previously published [26, 45], with temperature having an effect on both the timecourse of WPB exocytosis and the extent of WPB release from the cells. Experiments in this chapter seek to confirm those results and ensure they are applicable for the exact sample preparation protocol used for the cryo-electron microscopy experiments.

3.2 Preparing HUVECs containing WPBs for electron microscopy

To investigate the effect of seeding density and incubation time on HUVEC growth on EM grids and subsequent WPB number, experiments using serial dilutions of cells over varying incubation times were carried out, as per table 2. Seeding density is calculated based on a 14cm tissue culture dish containing ~10 million cells at confluency.

Montage images of each grid were made from 78 images taken at 20x magnification

	12hrs	24hrs	36hrs
100k cells/ml	4 grids, 2 per dish	4 grids, 2 per dish	4 grids, 2 per dish
50k cells/ml	4 grids, 2 per dish	8 grids, 2 per dish	8 grids, 2 per dish
25k cells/ml	4 grids, 2 per dish	4 grids, 2 per dish	4 grids, 2 per dish

Table 2: Table showing conditions examined by fluorescence microscopy.

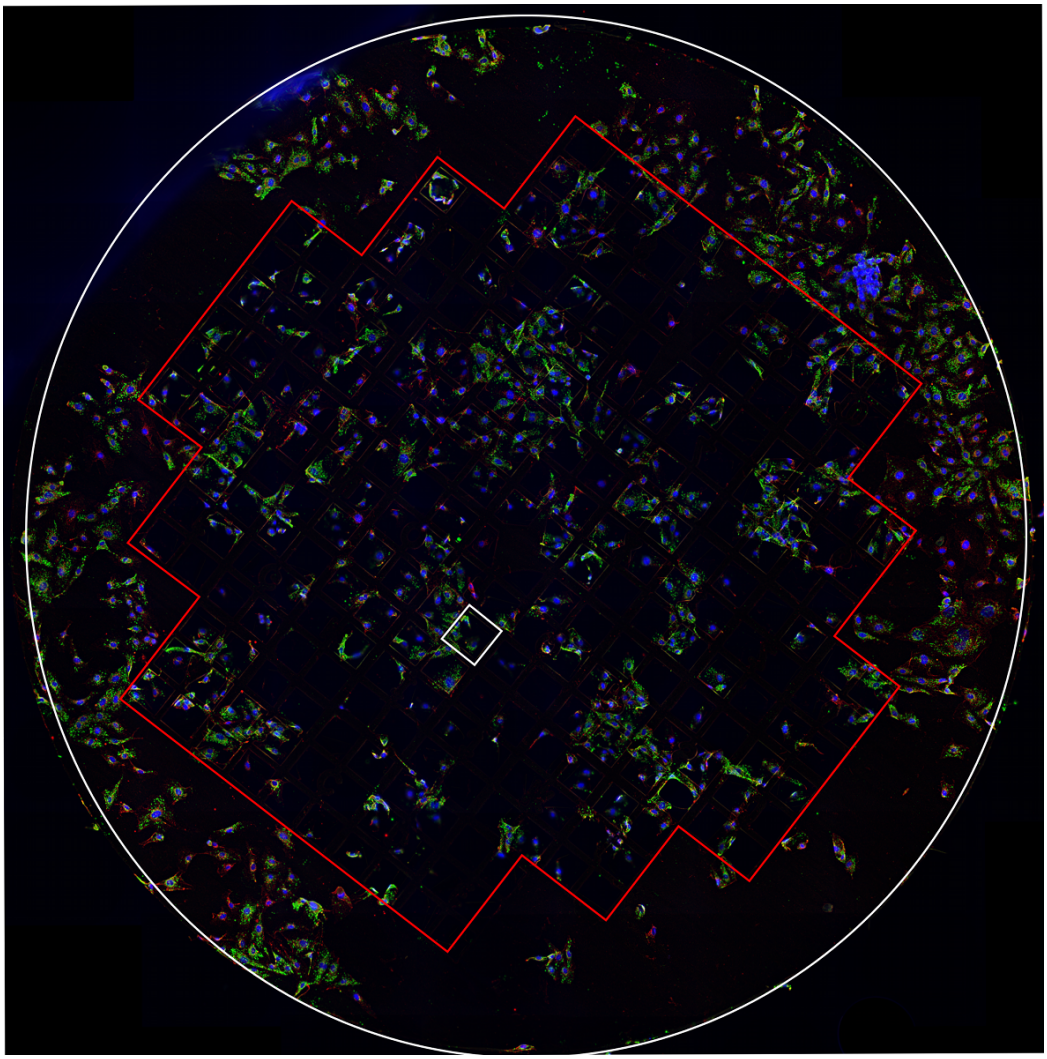

Figure 10: HUVECs grown for 24hrs on an EM grid from a seeding density of 50,000 cells/ml. Maximum projection of 5 slices. Blue: nuclei; Green: vWF and Red: plasma membrane; White circle: perimeter of the EM grid; White square: single grid square; Red line; perimeter of the grid mesh.

(figure 10). From these images, the DAPI channel was extracted and binarised, and nuclei automatically counted. The average number of cells per grid in each condition is compiled in table 3.

To allow the cells room to spread and have minimal thickness, in line with literature values [87], 1-2 cells per grid square was identified as the cell density target. This indicates that 50,000 cells/ml for 24 hours are the most suitable seeding and incubation conditions, with 1.49 cells per grid square (table 3, in bold).

This sample was re-imaged at a higher magnification so that individual WPBs

Seeding density (cells/ml)	Incubation time (hrs)	Cells/grid	Cells/mm^2	Cells/grid square
25000	12	295.25	40.41	0.47
25000	24	209.25	28.64	0.33
25000	36	347.50	47.56	0.55
50000	12	610.75	83.60	0.98
50000	**24**	**934.00**	**127.84**	**1.49**
50000	36	1205.00	164.93	1.92
100000	12	2361.75	323.26	3.77
100000	24	2688.00	367.92	4.29
100000	36	2513.00	323.96	4.01

Table 3: Average number of cells per grid, per mm^2 and per grid square for different seeding conditions and incubation times.

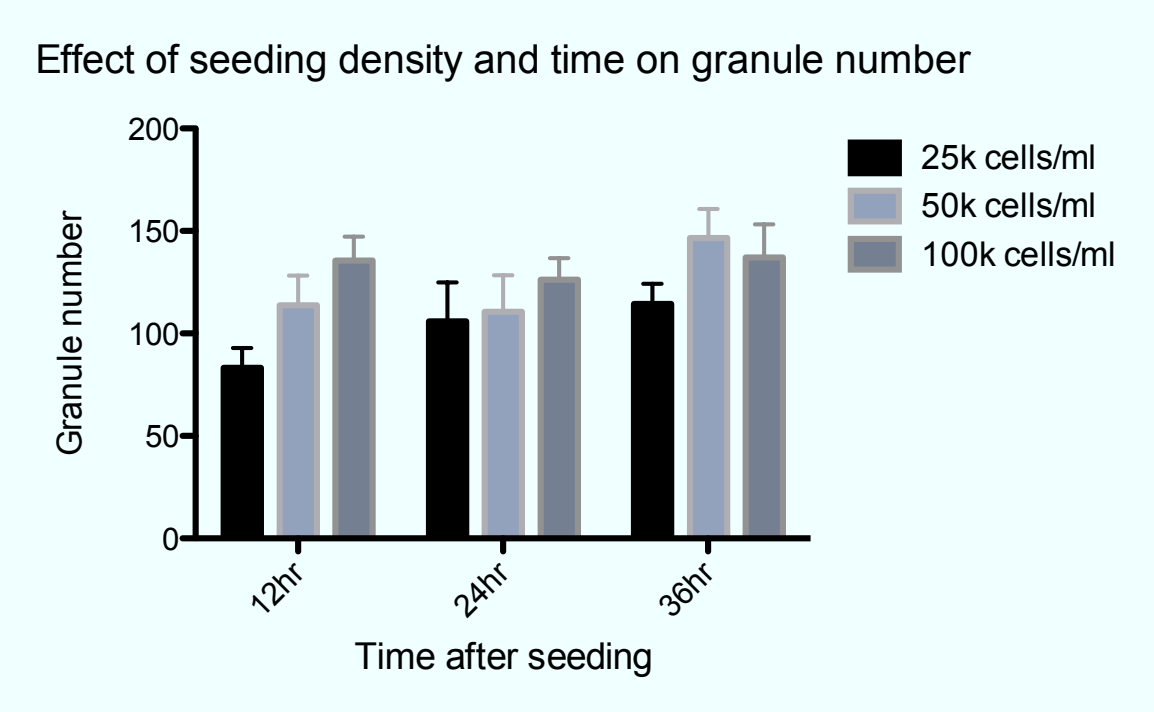

Figure 11: Effect of seeding density and incubation time on WPB number. The average number of granules per cell at each time point and seeding density is shown.

	25,000 cells/ml		50,000 cells/ml		100,000 cells/ml	
	Mean	n=	Mean	n=	Mean	n=
12hr	83	16	114	16	136	16
24hr	106	12	111	12	126	14
36hr	114	16	147	16	137	13

Table 4: Average number of WPBs per cell for different seeding conditions and incubation times.

within cells were visible. These images were used to investigate the effects of the same parameters (seeding density and incubation time) on the number of WPBs per cell (figure 11 and table 4). The effect of seeding density and incubation duration on WPB number is minimal beyond the first 12 hours, meaning that the overriding parameter to consider is achieving the correct cell distribution on the grid.

Determination of plunge-freezing conditions was done by scoring grids on the number of regions where it was possible to image through the thin edge of cells and secondly, the number of WPBs present in the images, until conditions where both could by imaged routinely were found. Humidity, temperature and blot time were varied

using the Vitrobot. Final conditions, determined in conjunction with the light microscopy experiments in section 3.3, used room temperature and humidity combined with a 20 second blot on the Vitrobot and 4 µl gold fiducials added immediately prior to blotting.

A typical EM montage of HUVECs grown on a carbon coated EM grid is shown in figure 12. A variability in cell distribution can be seen, with areas towards the bottom of the image having many more cells than the centre. The distribution towards the top left of the figure shows the desired number of cells. The irregularity in cell deposition onto the EM grids means that even with an appropriate number of cells per grid, many areas are unimagable. The same variability also means that total cell number need not be too strictly controlled as the variability across a single grid and between grids from the same tissue culture dish may eclipse differences between different seeding densities. The grid in figure 12 has regularly spaced letters, numbers and symbols included in the grid bars. These grids are used for correlative microscopy experiments, such as those in chapter 6.

EM montages of individual grid squares (figure 13) show HUVECs grown on the holey carbon Quantifoil film. Both dense regions of cell that cannot be imaged, presumably due to thickness, and thinner peripheral regions are visible. In those thin areas, such as in figure 13b, organelles can be seen, both in the carbon regions and within the holes of the carbon film. It is these thin areas with visible organelles at low magnification that are have their co-ordinates saved to be used for further imaging.

3.3 Determination of exocytosis rate after stimulation

In order to develop a protocol for freezing HUVECs at the moment of WPB exocytosis, live-cell fluorescence imaging experiments were done to determine the time period between addition of secretagogue to the EM grid and the window of maximal WPB release. Alexa 647 dye was added to the stimulant solution as a visual marker for when the stimulant appears in the field over view during records. By subtracting the

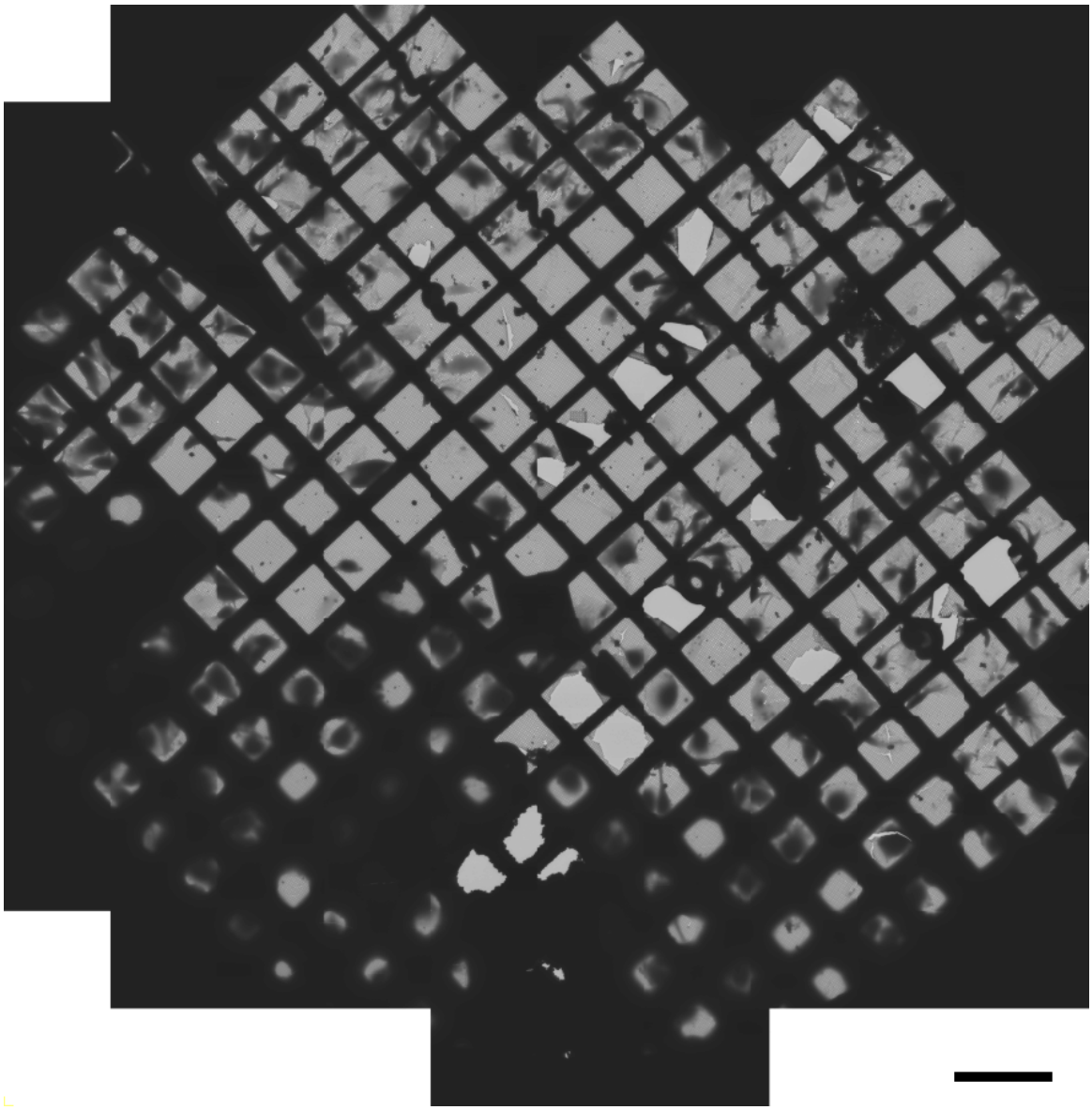

Figure 12: Frozen-hydrated EM montage of a whole grid, showing cells growing on a holey carbon support film. Letters, numbers and symbols are built in to the grid bars of this "Finder" grid to enable correlative microscopy. Scale bar: 200 µm.

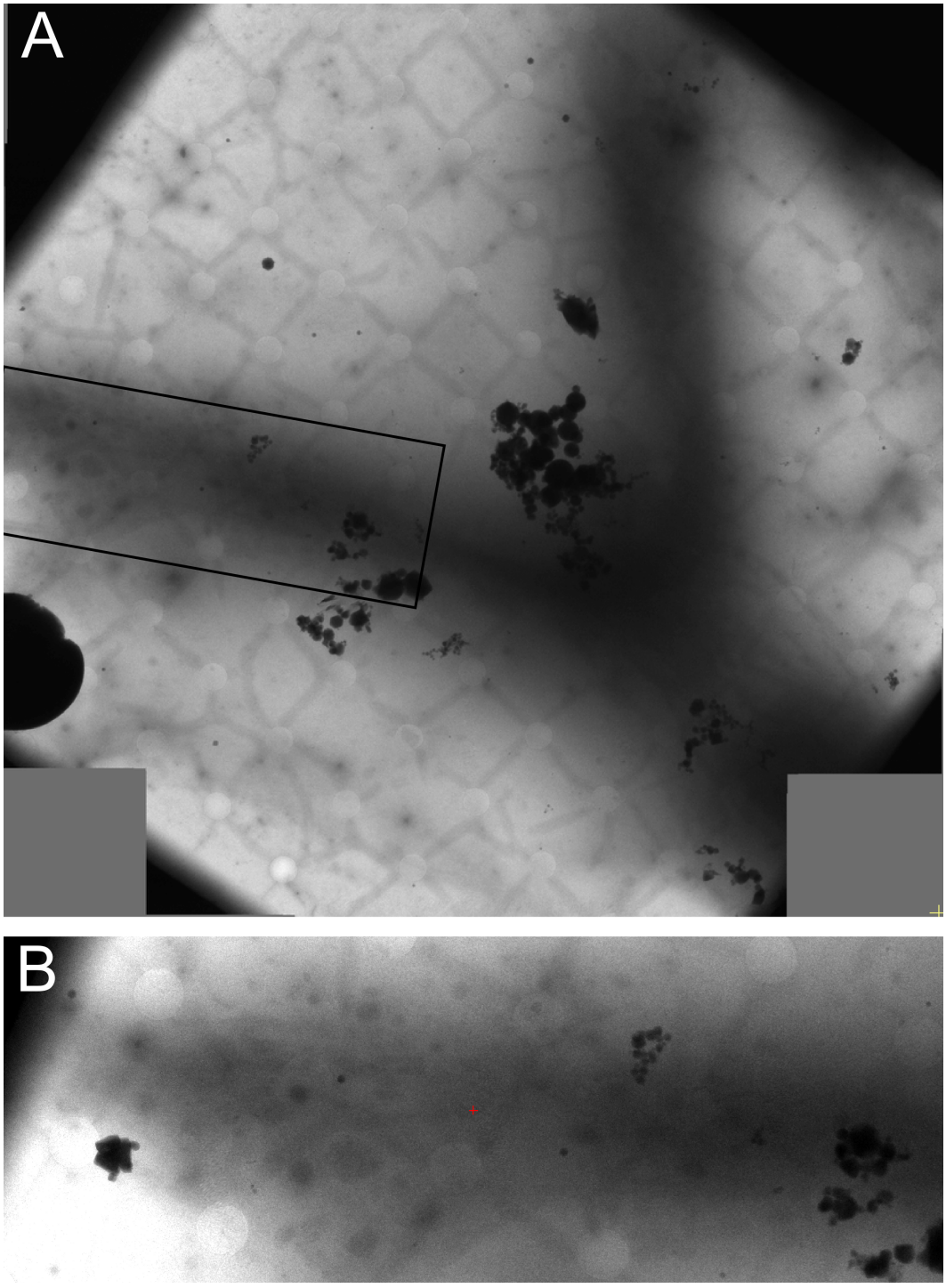

Figure 13: **A**: EM montage of a single grid square, containing a "Y-shaped" HUVEC over a Quantifoil holey carbon film exposed to 300 nM ionomycin. The left "limb" of the cell contains visible vesicles and mitochondria. **B**: Zoomed-in view of the boxed region in A, showing dense features in the cytoplasm at the thin edge of this cell.

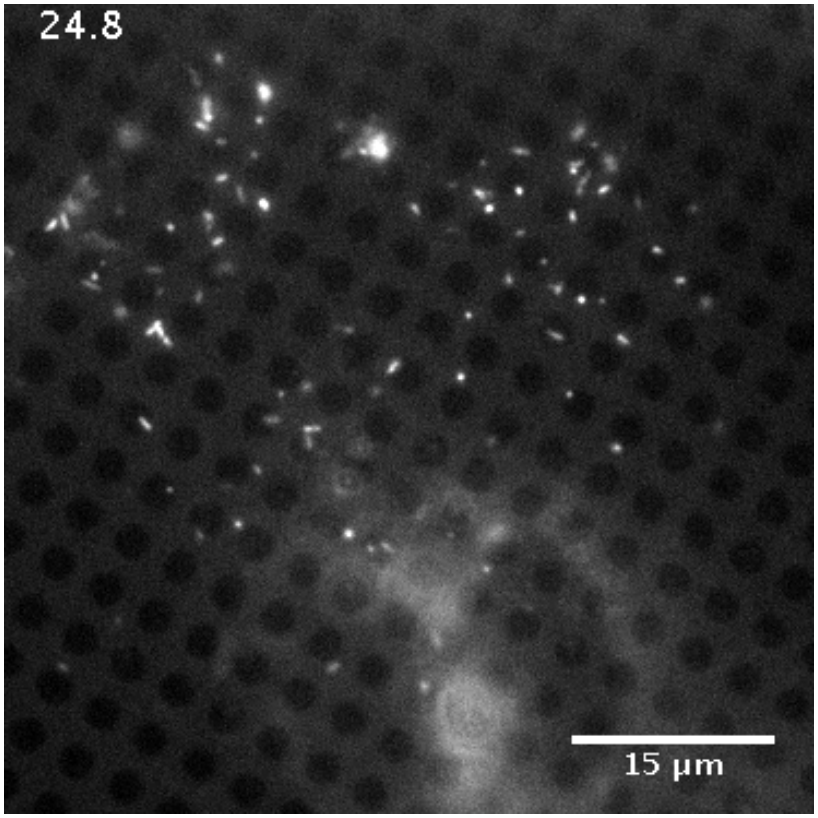

Figure 14: Sample frame from a live-cell microscopy recording of a secreting HUVEC cultured on an EM grid. Time after stimulation, in seconds, is shown on the top left.

frame in which the dye appears in the time-lapse from the time of the frame in which release occurs, stimulation times and rates were recorded. The addition of stimulant with fluorescent dye and the release and subsequent dispersal of EGFP-proregion were clear in the recorded movies. A sample frame from a recording is shown in figure 14. As previously [26], the moment of release was taken as the frame in which EGFP fluorescence increased, corresponding to the moment the pore was formed and the fluorophore exposed to pH change from the acidic WPB pH to neutral extracellular pH, increasing its brightness. This rapid increase in brightness is shown in a time-lapse of a single, fusing WPB (figure 15). The fluorescence intensity jumps between frames, indicating the opening of the fusion pore.

121 events from 6 cells were tracked, each cell from a different EM grid. In this instance, stimulation time includes a small lag period whilst the stimulant and dye

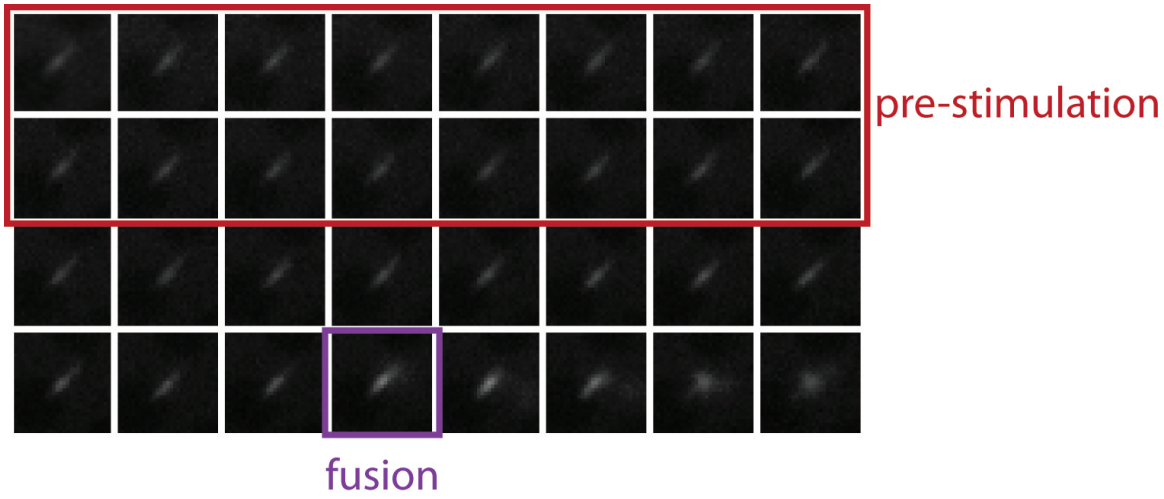

Figure 15: Time-lapse montage of a single WPB through pre-stimulation to post-fusion. The fluorescence peak can be seen in the fusion frame, where the intensity increases.

diffuse through the saline to the cell and takes its effect, rather than measuring the time between intracellular Ca^{2+}concentration increase and WPB release as has been done previously [26]. This is desirable as the grids were prepared in a similar fashion for EM, however without the possibility of measuring increased intracellular Ca^{2+}concentration, so time from application was a more important factor. The histogram showing event frequency after stimulation with 300 nM ionomycin is shown in figure 16.

The histogram indicates that the peak fusion time is the 17.5 – 22.5 s, the bin centred on 20 s. This is in line with previous data collected at over multiple temperatures from 7°C – 37°C using 1 µM ionomycin, where values reported are 10 s at 37°C and 70 s at 17°C, using a bin width of 10 s [45], and with a delay of 1.67 s between raised intracellular Ca^{2+}concentration and WPB release, again for 1 µM ionomycin [26].

3.4 Conclusion

In this chapter, experiments leading to a reproducible procedure for the culture and plunge-freezing of HUVECs for cryo-EM have been shown. The addition of gold fiducials improved the method in [4] and simplified subsequent tomographic processing.

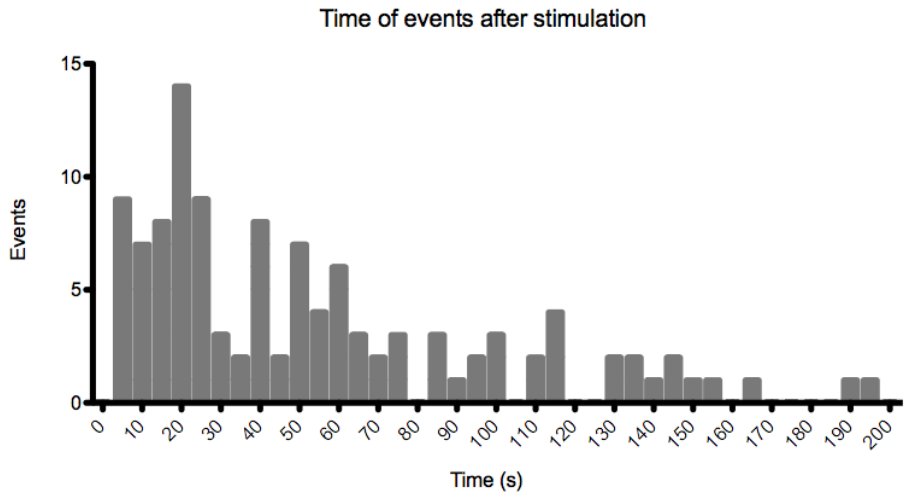

Figure 16: Histogram showing frequency of WPB release events after stimulation with ionomycim. Events are binned in 5 s intervals.

Collection of low and intermediate magnification montages helps to locate areas of interest within the cell and gives further cellular context for individual images. This method has been used to generate the results shown in the rest of this thesis, including the EM imaging of 591 WPBs and 45 WPB tomograms. Images and tomograms of mitochondria and cytoskeletal elements, such as filopodia and lamellipodia, were also collected.

Light microscopy experiments on EM grids were used to confirm that previously published determinations of exocytosis rate and kinetics were applicable on an EM grid as part of the sample preparation protocol prior to plunge-freezing. The difference is that the rise in intracellular calcium concentration, which is easily determined by light microscopy with a calcium-sensitive dye, cannot be determined in the Vitrobot immediately before plunge-freezing. Instead, an alternative measurement was made, from the time the stimulant appears in the field-of-view of the microscope. This mimicked the addition of the stimulant directly on the grid prior to blotting and plunge-freezing and gave a timescale of ~20 seconds for peak release; a timescale accessible within the sample preparation protocol.

4 Structural analysis of WPBs in 3D by cryo-electron tomography

4.1 Introduction

The size and shape of WPBs is commonly described as "rod-shaped" and up to 4 µm in length, to use terminology from their original discovery [129, 91, 109]. The driving force behind WPBs taking up this elongated shape is the shape of their primary cargo, VWF, which is stored within WPBs as helical tubules [109, 4]. If VWF tubules are disrupted, either by a truncation mutant removing the helical domains [68] or a disease-causing mutation forming shorter tubules [126], then round rather than elongated WPBs are formed.

WPBs are also known to become round after the fusion pore opens upon stimulated exocytosis [26]. The VWF tubules are maintained by a non-covalent interaction with the proregion domains D1 and D2 at acidic pH [68, 47]. Pore formation exposes the VWF tubules to neutral pH, causing loss of the proregion [41] and tubule structure to disassemble, eventually unfurling into strings capable of binding platelets [21]. This loss of cargo and cargo structure causes the WPB to become round, even if it is subsequently retained by the cell [2].

The width of WPBs (in 2D projections, equivalent to their 3D diameter) has also been proposed to indicate the maturation state of the WPB, with thinner and more electron dense WPBs being located further into the cell periphery than immature WPBs [134]. The increase in electron density is caused by the intertubule distance reducing as part of the maturation process. The length of WPBs is thought to be determined by the size of the Golgi stack it buds from, as WPB length can be varied with the addition of drugs to alter Golgi stack size [30]. A survey of the lengths of ~2 million WPBs by immunofluorescence microscopy suggests that WPBs preferably form in ~0.5 µm length increments which are visible components within longer WPBs [30]. Around 80 % of non-stimulated VWF comes from the basal secretion of WPBs

[37] and treatments to reduce the size of WPBs (either by lowering VWF levels or manipulating the Golgi) give rise to small WPBs with an increase in basal secretion and reduction in regulated secretion [30], indicating that small WPBs are preferentially released under basal conditions. Therefore, the length of a WPB influences its release properties.

The geometry of VWF packing and the intertubule distance is of interest because the VWF tubule can be formed by only 44 % of the VWF protein, at the N-terminus [47]. Therefore, the 'space' between the tubules is most likely to be occupied by the C-terminal domains of VWF, giving rise to the minimum possible distance between tubules. The parallel orientation of the tubules is certainly important for the elongated shape of the WPBs and the C-terminal domains must be accomodated around this. By negative stain EM, the C-terminal domains of VWF form a dimeric bouquet with each half of the dimer "zipped up" [137]. Combined with the early EM of VWF strings [32], this has lead to the proposal of various schemes for accomodation of the C-terminal domain as radially protruding arms from the VWF tubules that may intercalate in the intertubule space [36, 47, 137]. These arms have not been seen between VWF tubules within the WPB.

Rounded WPBs must contain either; non-parallel tubules, with an increased intertubule distance to account for non-ideal packing of the C-terminal domains or VWF that is no longer tubular but in string or unfurled form. WPBs containing predominantly VWF in string form would be hard to distinguish by cryo-EM as they would lack both the distinctive rod-like shape of the organelle and signature helical parameters of the VWF tubules.

In this chapter, the baseline size and shape of WPBs in HUVECs is established and compared with granules from other conditions which are predicted to have other geometeries; HUVECs stimulated to release their WPBs, HUVECs subjected to hypotonic shock and from HHMECs (human heart microvasculature endothelial cells). Rounded WPBs with a stalk imaged in stimulated HUVECs are also shown. Cryo-

electron tomography of WPBs has enabled the building of 3D models for the packing and alignment of VWF tubules in ordered and disordered WPBs. The C-terminal arms protruding from VWF tubules have been visualised within the WPB for the first time.

4.2 Comparison of WPBs from stimulated and unstimulated cells

In the process of imaging HUVECs, a large library of WPB images has been collected. Low dose images are collected prior to tilt-series for tomography. Not all areas are appropriate for collecting tilt-series, either for image quality reasons or an obscured tilt-range, but these images form an rich data set for measuring the basic geometric parameters of WPBs in a way not possible with fluoresence microscopy or electron microscopy of sections where a single WPB may span multiple sections.

2D projections of 535 WPBs have been collected across all the stimulation conditions used. The breakdown of each condition is shown in table 5. Examples of 2D projections of 5 WPBs from HUVECs stimulated with 300 nM ionomycin are shown in figure 17. In each of these images the WPBs were identified by their characteristic rod-like shape and electron density and where possible, the signature Fourier transform of the VWF tubules [4]. However, tubules were not visible in all images - this is one of the reasons that an image may not have been suitable for tomography. Identified WPBs had their maximum length (parallel to the VWF tubules, including at any bent/hinged regions) and width (perpendicular to the VWF tubules and ignoring any clubbed ends) recorded. The width in 2D is equivalent to the diameter of the cylindrical portion of the WPB in 3D. The lengths and widths of WPBs from unstimulated cells are shown in figure 18 and figure 19.

The range of lengths are between 268–2883 nm, comfortably within the often quoted range of "$< 4\,\mu m$" [91, 129], and approaching the upper limit for measuring, based on the field of view at the most commonly used magnifications that allow

Condition	WPB number
Unstimulated	105
300 nM ionomycin	154
1 µM ionomycin	225
100 µM histamine	51
Total	**535**

Table 5: Number of 2D images of WPBs from HUVECs in each condition.

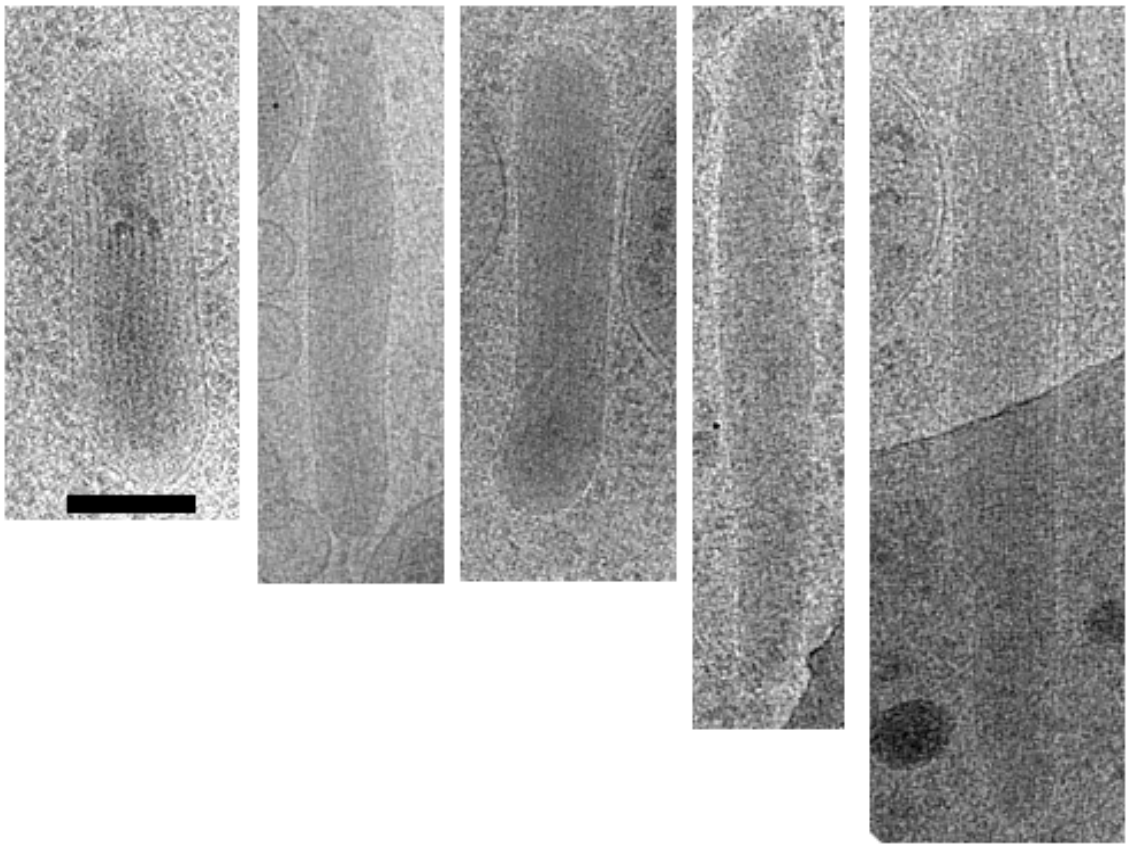

Figure 17: Examples of 2D projections of WPBs from the same grid containing HUVECs stimulated with 300 nM ionomycin. Scale bar: 200 nm

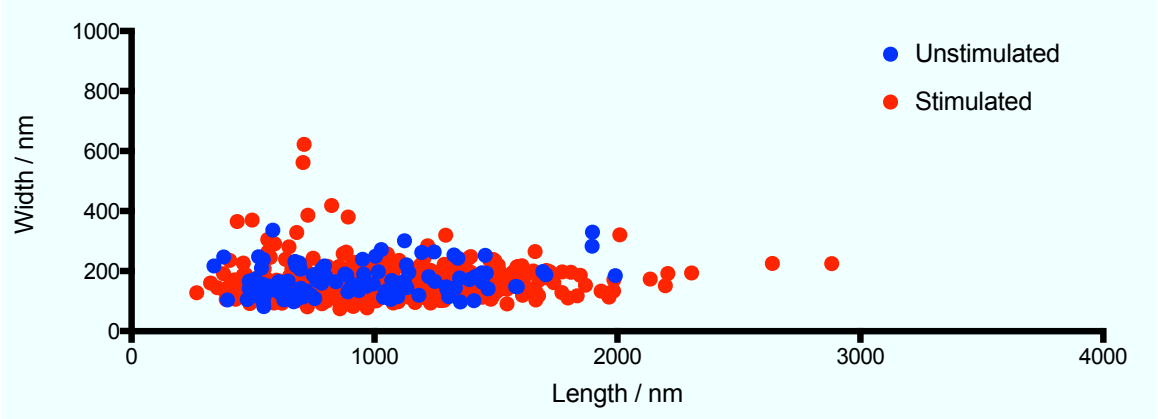

Figure 18: Scatter plot showing the lengths and widths of 535 WPBs. Results from unstimulated cells are in blue, stimulated cells are in red. All 3 stimulated conditions have been pooled together.

unambiguous WPB identification via the VWF helices. The mean length is 951 nm, indicating that the observed lengths are very much skewed towards the shorter end of the range, across both unstimulated and stimulated cells. The widths are more tightly distributed, with a range of 82–336 nm for the unstimulated and 75–622 nm for the stimulated data, but a mean of 160–170 nm for each population. WPB width does not change with length, with WPBs of all widths present across the entire length range, shown as a horizontal clustering of the points in figure 18. This could be indicative of a 'preferred' width for WPBs, either due to the availibility of VWF as the nascent WPB emerges from the trans-Golgi (figure 2), an optimal arrangment for packing of VWF tubules within the WPB or a function of the AP-1/clathrin coat formed around emerging WPBs at the Golgi and required for WPB elongation [59], or some other factor. Recent evidence suggests that WPB size is dependent on the size of the Golgi stacks in which VWF condenses before reaching the TGN and budding into a nascent WPB, and that WPB size can be manipulated by unlinking the Golgi ribbon by nocodazole treatment, lowering the pH or knockdown of the Golgi protein giantin [30].

Assessment of organelle size using high throughput confocal morphometry and super-resolution light microscopy (using STORM (stochastic optical reconstruction

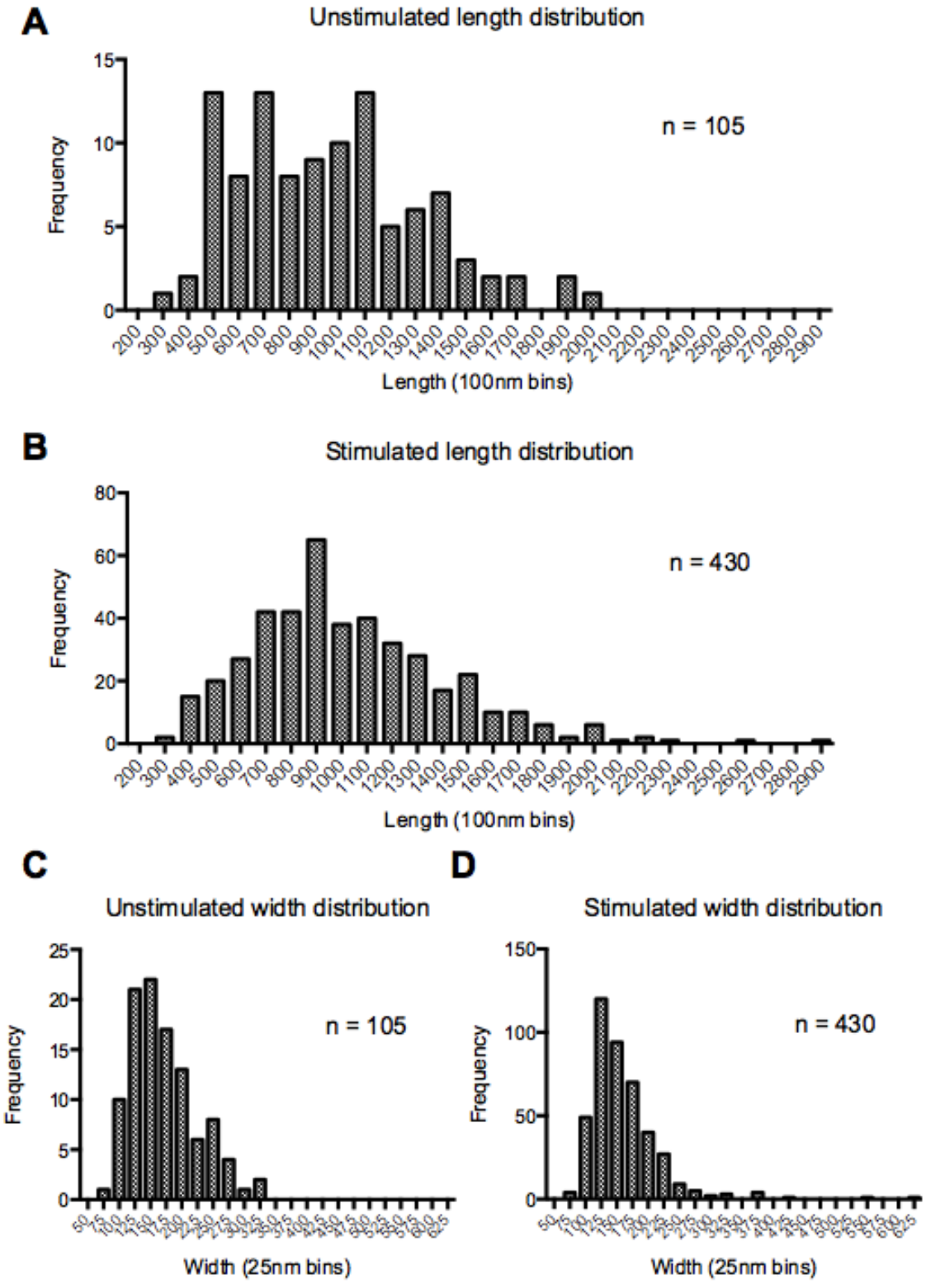

Figure 19: Histograms showing measured WPB lengths and widths for stimulated and unstimulated populations. Again, measurements from all 3 stimulated conditions have been combined. n indicates number of measurements in each condition.

microscopy)) has suggested that WPBs contain a repeating length unit of ~0.5 µm. WPBs would then be formed by multiple units joining together [30]. The current dataset (figures 18 and 19) shows a peak at the mean length of approximately 1 µm, but not at further multiples of 0.5 µm. This could be due to the small number of measurements compared with 2×10^6 that STORM and high throughput techniques were able to image, and the short lengths of the WPBs observed by cryo-EM (only 10 % >1.5 µm). It is possible that longer WPBs are formed from smaller subunits before leaving the Golgi, however, the raw WPB cryo-EM images show no discontinuity of the VWF tubules within WPBs to suggest they consist of multiple, 0.5 µm VWF units. The WPB width measurements shown here are consistant with those obtained from high-pressure freezing and cryo-sectioning experiments [134], although in this case electron density was not used to distinguish between mature and immature WPBs: all are thought to be mature as they are at the thin edge of the cell. The minimum width observed both here and in [134] is similar and corresponds to between 1 and 2 VWF tubules at their widest.

Both figure 18 and figure 19 also show a handful of outliers from the main cluster of points in the stimulated condition, that have a considerably larger width. Two of these WPBs are approaching spherical, with width:length ratio of 0.88 and 0.80 respectively, and several others lay with widths ~ 400 nm. As these occur only in the stimulated state, it is likely they represent rounded WPBs which are fusing or have fused and retreated in the 'kiss-and-run' or 'lingering kiss' fashion observed by light microscopy [2]. However, the majority of the WPBs from cells exposed to stimulant have lengths and widths consistent with the WPBs from unstimulated cells, sitting in the same region of the graph in figure 18 and showing no significant difference between the populations (p=0.44 for length and 0.34 for width, Welch's t-test for populations with unequal variances). This is probably because although the cells have been exposed to stimulant, not all cells will have been sufficiently stimulated to release at the time of plunge-freezing, and even in releasing cells, < 50 % of granules

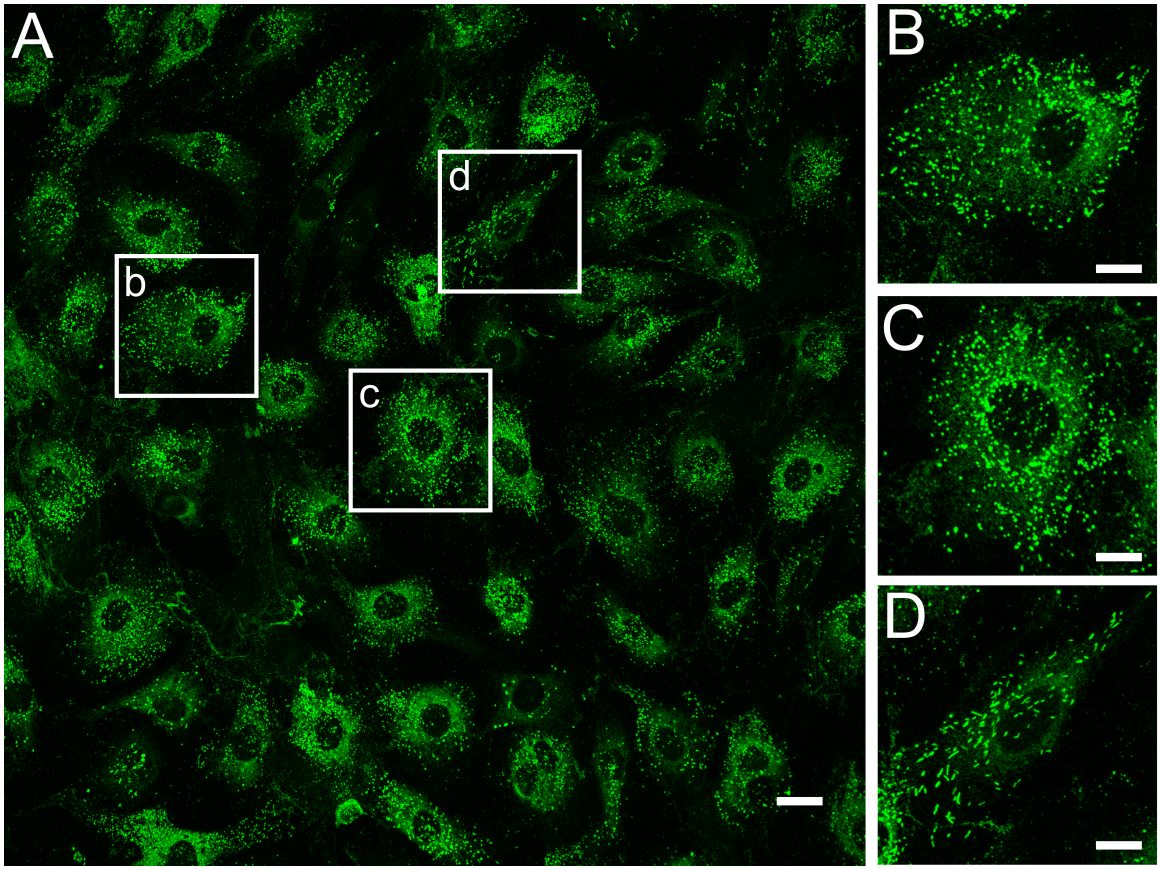

Figure 20: **A**: Immunofluorescence image of HHMECs grown on a glass coverslip and stained for VWF, showing round WPBs and characteristic ER staining. Scale bar: 20 µm. **B, C and D**: Zoomed images corresponding to the boxed areas in A. B and C show cells with exclusively round WPBs. D shows a cell containing elongated, rod-shaped WPBs. Scale bars: 10 µm.

are released at this temperature [45], as in section 3.3.

4.3 Comparison of WPBs across different cell types

Light microscopy of HHMECs shows that most of these cells store VWF in round WPBs (figure 20). 1 run of 2 grids of HHMECs were prepared for imaging by cryo-electron microscopy resulting in 39 WPB images with the aim of comparing endogenously round WPBs to rod-shaped WPBs and the rounding of rod-shaped WPBs during fusion and VWF release.

Firstly, the lengths and widths for the HHMEC WPBs were measured as for the HUVEC WPBs in section 4.2. The lengths and widths of the HHMEC WPB are

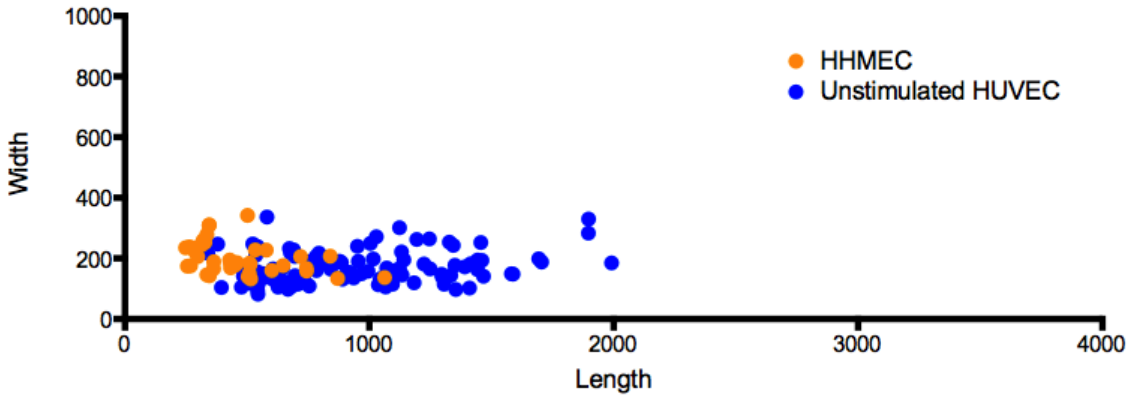

Figure 21: Scatter plot showing the lengths and widths of WPBs from HHMECs compared with HUVECs. Results from HUVECs are in blue, HHMECs are in orange. The axes have been kept the same as in figure 18.

shown compared to the WPBs from unstimulated HUVECs in figure 21. The axes have been kept the same as figure 18 for comparison. HHMEC WPBs are clustered towards the bottom left of the graph; they have a slightly increased width to HUVEC WPBs, but are considerably shorter in length, making them rounder in appearance. The observation of small, round WPBs by EM concurs with the light microscopy of HHMECs in figure 20.

To further investigate the structure of rounded WPBs in HHMECs, 10 tomograms were calculated. 3 slices from a tomogram of a HHMEC WPB are shown in figure 22. Despite its small, round appearance, VWF tubules can clearly be seen in all sections of figure 22. As the VWF tubules are thought to define the elongated, rod-shape of WPBs and sufficient to drive the formation of rod-shaped pseudo-WPBs in non-endothelial cells expressing the tubule-forming domains of VWF [124], it is interesting to observe tubules in non-elongated WPBs. That these cells endogeneously form round WPBs gives more evidence for the idea that VWF expression is not the only factor regulating WPB size, and other factors such as the influence of the Golgi ministack size are important [30]. The effect of size on the functional properties of WPBs indicates that short WPBs are preferentially released through basal secretion and have a different balance of properties, tending towards proinflammatory rather than haemostatic [30].

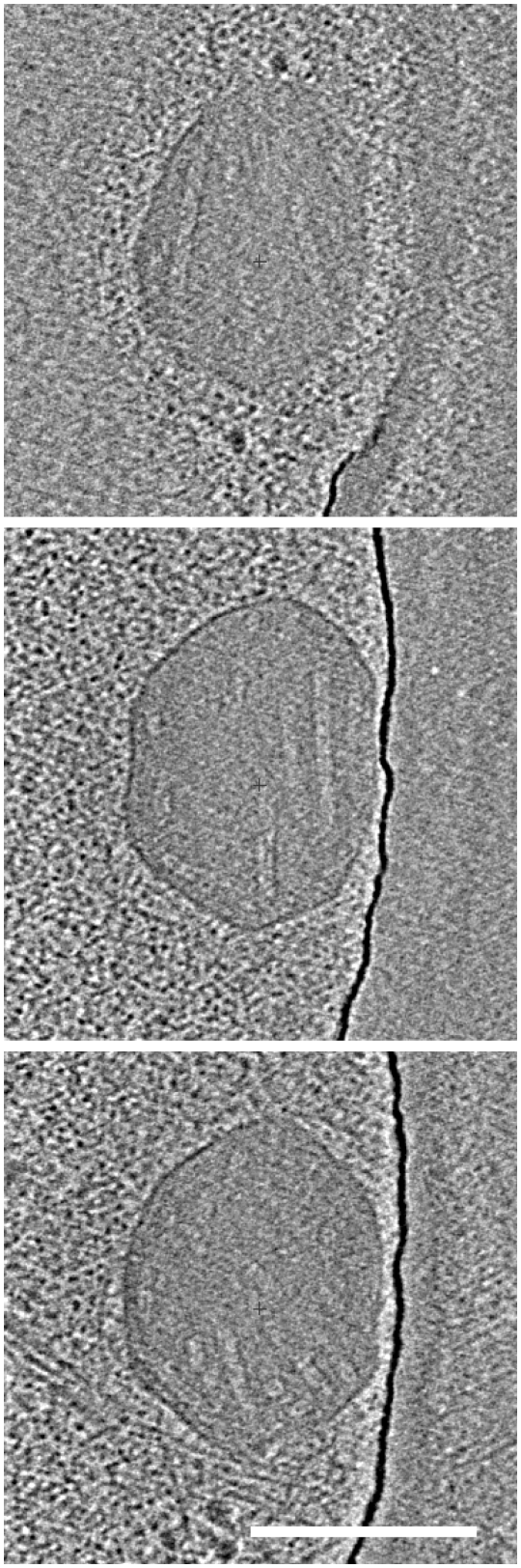

Figure 22: Slices from a tomogram of a HHMEC WPB with visible VWF tubules in running in different directions. The edge of the carbon can be seen on the right-hand side of each slice. ±51° tilt-series collected on an FEI Polara operating at 200 kV, -8 µm defocus. Scale bar: 200 nm.

Similar round WPBs containing VWF tubules have also been observed in HEK293 cells (a non-endothelial cell line) transfected to express the disease-causing mutations C1149R and C2754W [126]. These mutations disrupt proregion binding in the D3 domain and C-terminal dimerisation at the CK domain respectively, causing quantitative (types 1 and 3) VWD. As these round, tubule-containing WPBs are implicated in disease, it suggests an impaired haemostatic ability from them. Small, round WPBs in HHMECs may also have an impaired haemostatic ability, delivering fewer and shorter VWF strings due to their size, but with no change in their membrane protein mediated proinflammatory role [30]. The different behaviour of small WPBs could explain why cells from different vessels exhibit different sized WPBs. However, such a link may be confounded by the source of the HHMECs from diseased heart tissue collected during transplant procedures [64, 66].

In some views of HHMEC WPBs, such as the middle slice in figure 22, 4 VWF tubules are parallel to each other and aligned to the long axis of the WPB. There is some deviation from parallel on the left hand side of the WPB in this slice, but it otherwise looks similar to a shortened WPB. However, the top and bottom slices of figure 22 show tubules orientated in a different direction, running diagonally across the long axis. These rotated tubules are responsible for the round appearance of the WPB by deforming its width. Similar distributions of tubules are observed in the other HHMEC WPB tomograms, but not in rod-shaped WPBs from HUVECs in the absence of stimulation or the presence of an internal vesicle (discussed in chapter 5) to disturb the paracrystalline packing. Therefore, HHMEC WPBs cannot simply be described as truncated rod-shaped WPBs because the VWF tubules do not run in a consistant direction along the longest axis. Instead, the WPB is comprised of many short tubules which can run in different directions.

Although the imaged rounded HHMEC WPBs contain VWF tubules, it is hard to say if there is also a second population of round WPBs that neither contain tubules nor have the typical dense and aspherical appearance - the primary signs for identifying

WPBs - as they wouldn't be identified in the images. Other vesicles may also contain VWF in an expanded, less densely packed form and without tubules.

4.4 Imaging artificially rounded WPBs

WPBs within HUVECs can be made round by exposing the cells to hypotonic shock and then allowing the cells to recover. In these experiments, hypotonic shock was delivered by replacing the cell culture media with a 10-fold dilution of PBS in distilled water and allowing the cells to recover for 2 hours in pre-warmed media in an incubator before preparing for imaging. Whilst the HUVECs recover, the WPBs within the HUVECs remain permenently rounded.

To ascertain the optimal exposure time to hypotonic shock for preparing HUVECs with round WPBs, an immunofluorescence experiment was set up. HUVECs were grown to confluency on 24 coverslips in a single dish overnight. 3 coverslips per condition were exposed to the following durations of hypotonic PBS: 30 seconds, 1 minute, 2 minutes, 4 minutes, 8 minutes, 12 minutes, 20 minutes and control (8 minutes of stock PBS) before the PBS was replaced with prewarmed media for recovery. Cells were allowed to recover for 2 hours before preparing for immunofluorescence as in section 2.7.

An image from each coverslip was collected, showing the WPBs within several cells. Example images from some conditions are shown in figure 23. The rounding effect was quantifiably assessed in ImageJ by thresholding the maximum projections of each image to remove the background and leave the WPBs. The *'Analyse particles'* command was used to measure all objects $\geq 10\,\mathrm{px}^2$ in area and output their circularity ($4\pi\left(\frac{area}{perimeter^2}\right)$), where a value of 1.0 is a perfect circle. The average circularity across 3 images from each condition is tabulated in table 6.

Both table 6 and figure 23 show that even the shortest exposure time to the hypotonic shock solution causes the WPBs to become rounder than the control. The trend is for the average circularity to increase with increased exposure to hypotonic shock throughout the time periods examined. The longer time periods appear to

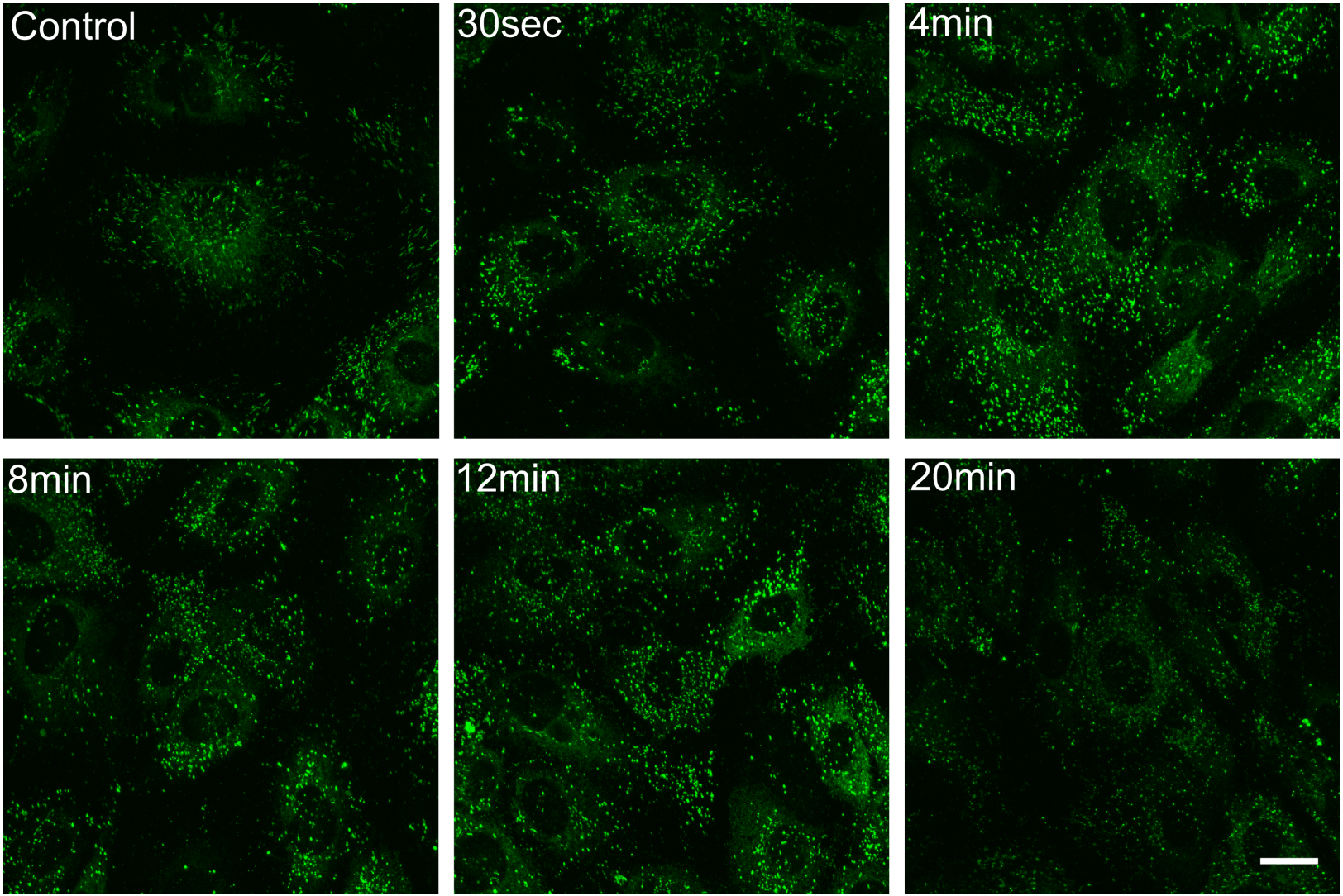

Figure 23: Fluoresence micrographs showing rounded WPBs in HUVECs after exposure to hypotonic shock for different time periods. Scale bar: 20 µm.

Hypotonic exposure time	Circularity
Control	0.540
30 seconds	0.659
1 minute	0.622
2 minutes	0.679
4 minutes	0.723
8 minutes	0.702
12 minutes	0.758
20 minutes	0.755

Table 6: Average circularity of WPBs after exposure to hypotonic shock.

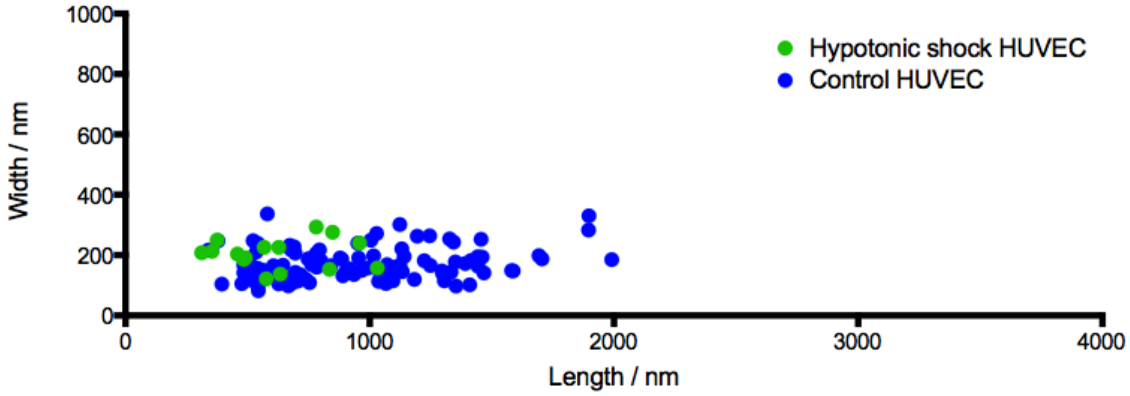

Figure 24: Scatter plot showing the lengths and widths of WPBs from hypotonic shock HUVECs compared with control HUVECs. Results from control HUVECs are in blue, hypotonic shock HUVECs are in green. The axes have been kept the same as in figure 18.

adversely affect the HUVECs and WPBs, in addition to becoming round. In the 20 minute condition, the fluorescent spots appear smaller and dimmer, indicating WPBs that have been released. Some release was also observed in the 12 minute condition, so the 8 minute condition, as the longest period without any sign of adverse effects was used for the cryo experiments.

For cryo-EM, 1 run of 16 grids of hypotonic shock HUVECs were prepared using the parameters obtained in the light microscopy experiments. From these grids, 15 WPBs were imaged. A scatter plot of their measurements compared to control HUVEC WPBs, showing their shortened, rounded nature is shown in figure 24. Like the HHMEC WPBs, the hypotonic shock WPBs are clustered to the bottom left of the graph, being considerably shorter and slightly wider than HUVEC control WPBs.

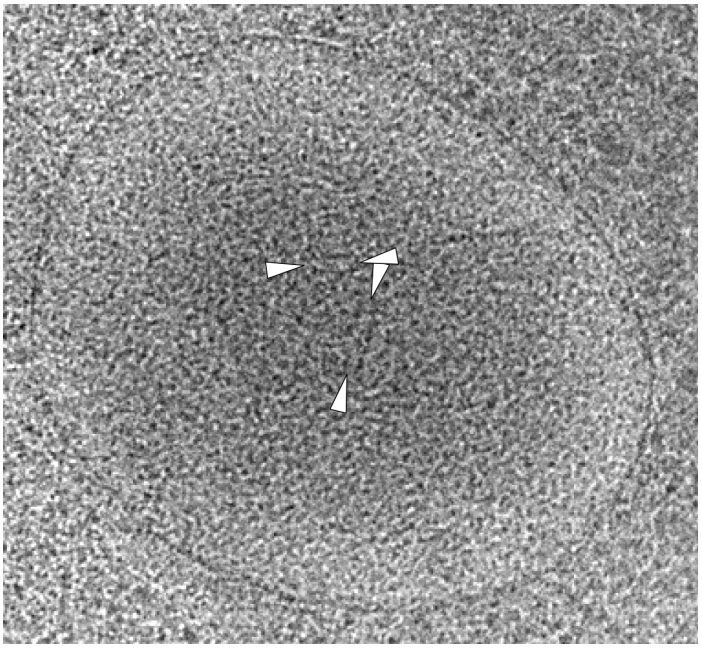

Figure 25: A round dense granule with few visible tubules, marked with arrowheads at either end. The tubule segments are consistant in size with VWF.

This shift in dimensions is predicted, as WPBs of all sizes become round due to the treatment, but if the 2D width is indicative of 3D diameter of the organelle and the total organelle volume remains constant then a modest change in width is able to compensate for a larger change in organelle length as the volume is proportional to the square of the radius. This may explain why there are no larger, round objects reported. As VWF tubules often run the length of a WPB, any change in length must be accompanied by a breakage of the VWF tubule.

However, if objects have become round due to a loss of VWF tubules into a disordered form and have expanded into a less densely packed vesicle, then they would not be identifiable as WPBs. An example of a possible WPB is shown in figure 25. This large vesicle is 630 nm×517 nm, and less electron dense than the WPBs with more visible tubules, which may indicate an increase in volume if it was originally packed to the same density with VWF tubules. The overall texture of the vesicle contents is mottled, giving the appearance of filaments. Some short sections of tubule, consistant with VWF are indicated, running between the arrowheads. Assuming this vesicle is a sphere with average radius of 287 nm, it would correspond to large WPB; average

(170 nm) width and 4.4 µm in length - larger than any observed. If this object is a WPB, it seems likely to have increased volume and decreased density as a consequence of rounding due to hypotonic shock treatment.

Aside from the possibility of large VWF containing vesicles, the hypotonic shock rounded WPBs are similar in both size and appearance to those from HHMECs. This is surprising as while the HHMECs are assumed to assemble at the Golgi with short VWF tubules leading to round WPBs, the VWF tubules in the hypotonic shock have been truncated from the lengths within the control HUVECs. This suggests a selective disassembly of the tubules, breaking the non-covalent contacts between the VWF multimers and the proregion. The disulphide bonds would not be broken, so the multimers would still be intact and connected by VWF in 'string' form, only tubulation would be affected. It is not clear if VWF tubules consist of a single multimer [17, 103, 47], and if not, loss of proregion at these sites would split tubules.

The factors causing tubules to deviate from parallel is unknown. Using the currently proposed VWF model from negative stain EM, of a helical tubule with arms radiating from it [137], parallel appears to be the most efficient way to pack the VWF tubules with the C-terminal portion allowed to interdigitate in the area between the visible tubules. Deviation from parallel would therefore require more space and so only occur with a 'swollen' WPB or a change in packing such as the possible loss of tubule structure in some locations.

4.5 Weibel-Palade body exocytosis

Of the WPBs images from stimulated HUVECs (table 5), 33 WPBs were imaged in 3D in 24 tomograms. 2 of these tomograms show rounder, 'marrow' shaped WPBs with a membranous protrusion at one end (figures 26 and 27), and others show disordered WPBs with non-parallel VWF helices (figures 28 and 29). The protruding membranes appear similar although shorter, to the previously observed connection between a fusing WPB and the plasma membrane [4], and coincide with wider, 'marrow' shaped

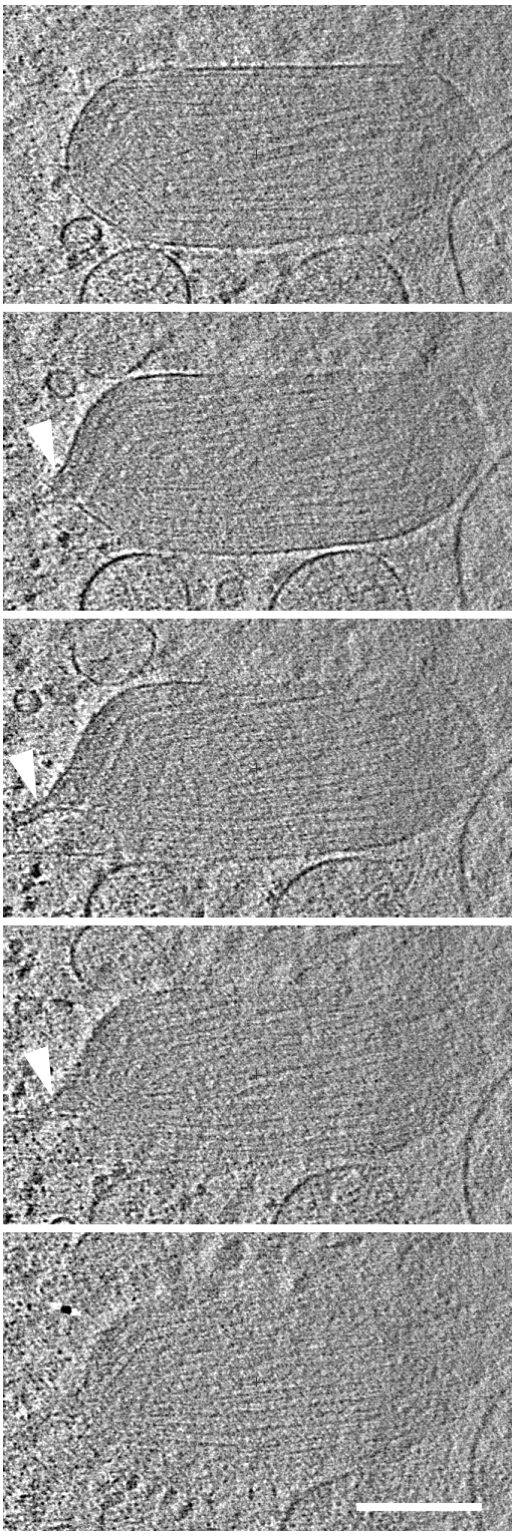

Figure 26: Slices through a tomogram of a WPB with a membrane fusion stalk in a HUVEC stimulated with 0.3 µM ionomycin. The second and fourth slice show the top and bottom, respectively, of the stalk emerging from the WPB and the third slice shows the centre of the stalk with wedge-shaped content. ±30° tilt-series collected on an FEI Polara operating at 200 kV, -8 µm defocus. Scale bar: 200 nm

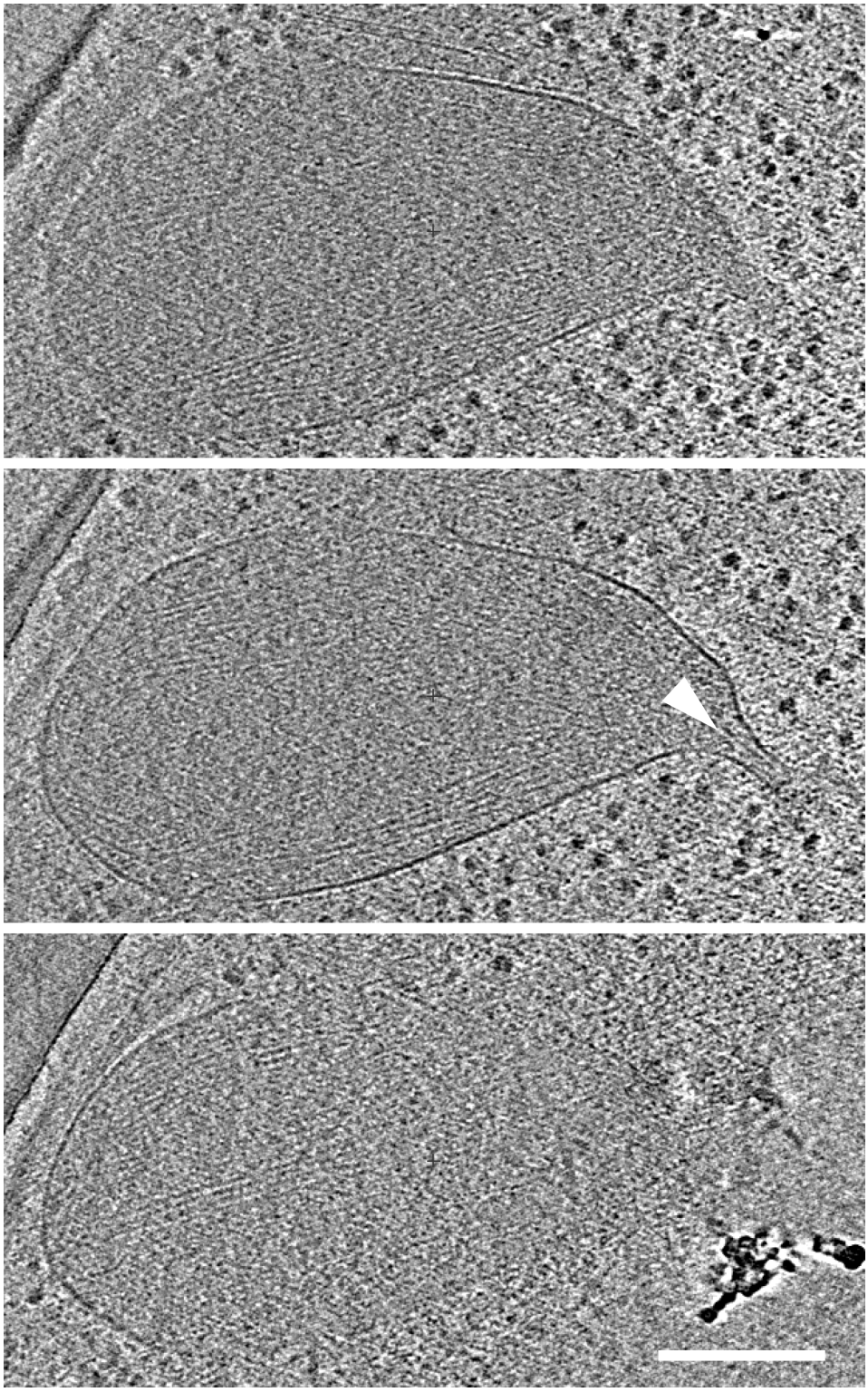

Figure 27: Slices through a tomogram of a WPB with a membrane fusion stalk in a HUVEC stimulated with 1 µM ionomycin. The first slice shows the top of the WPB, and the top of the fusion stalk. In the middle slice, a tubule (arrowhead) is within the stalk. ±60° tilt-series collected on an FEI Polara operating at 200 kV, -5 µm defocus. Scale bar: 200 nm

Figure 28: Slices through a tomogram of a disordered WPB in a HUVEC stimulated with 0.3 µM ionomycin. At all 3 heights, the right hand side of the WPB remains rod-shaped and the VWF helices are parallel although showing some signs of bending. On the left hand side, the VWF helices are no longer parallel and much shorter in length. In the middle slice, a protruding section of membrane with no VWF helix inside is indicated with an arrowhead. ±60° tilt-series collected on an FEI Spirit operating at 120 kV, -8 µm defocus. Scale bar: 200 nm

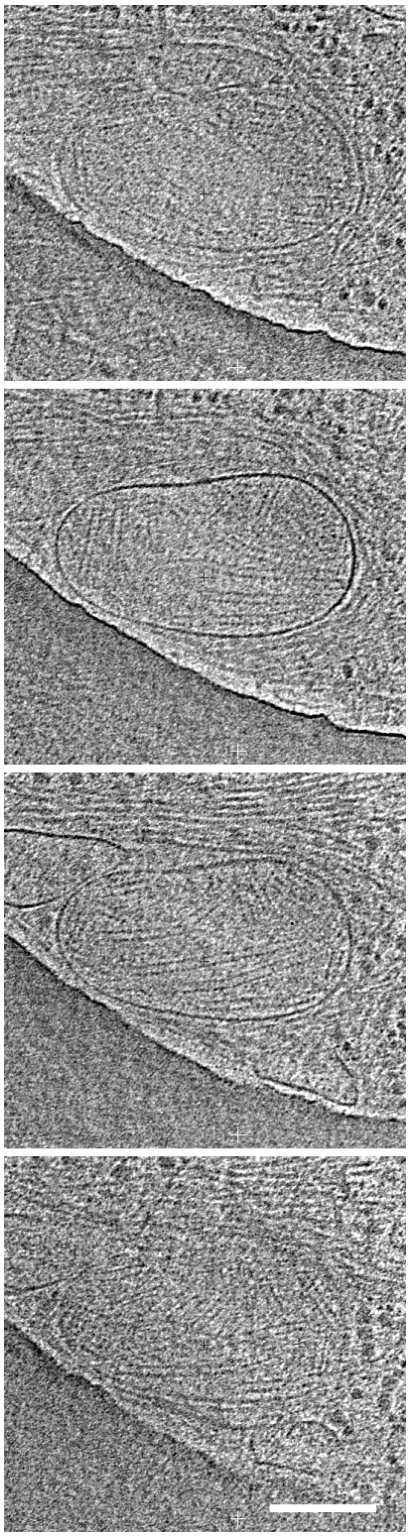

Figure 29: Slices through a tomogram of a disordered WPB in a HUVEC stimulated with 0.3 µM ionomycin. The VWF tubules within the WPB are oriented in all directions at each height. ±60° tilt-series collected on an FEI Spirit operating at 120 kV, -8 µm defocus. Scale bar: 200 nm

WPBs. As the protrusions appear to be involved in fusion and are longer than a simple pore between close membranes, they are termed fusion stalks.

Slices through a tomogram of a WPB with a fusion stalk are shown in figure 26. The features that identify the WPB as fusing are the wider, 'marrow' shape, as observed in [4] and the short, $17 \times 108\,\text{nm}$ stalk protruding from the left hand side. The tubules are predominantly parallel, with some deviation towards the stalk, which would be expected if the WPB was disassembling in response to pH change coming from the stalk. The stalk appears to contain a tubule with a wedge-like end. It is not clear where the stalk joins the plasma membrane and connects the WPB to the extracellular space. It is possible that the WPB is fusing parallel to the z-axis, meaning the plasma membrane and pore are perpendicular to the z-axis and therefore not seen due to the missing wedge. The position of this WPB on the EM grid was very close to the grid bar, limiting tilted data collection to $\pm 30°$ and meaning the tomogram has a substantial missing wedge. Proximity to the grid bar also means the WPB was in an area of thicker ice, also reducing contrast.

A second example of a fusing WPB with membrane stalk is shown in figure 27. This WPB is rounder than the previous example, indicating it is at a later stage of fusion and disassembly. The fusion stalk is considerably wider than in the previous example, with dimensions of $29 \times 108\,\text{nm}$, and also contains tubular content. Again, the junction between the fusion stalk and the limiting membrane is not clear.

Also observed in stimulated HUVECs are disordered WPBs with non-parallel VWF. On the right hand side of the WPB in figure 28, the VWF helices are running predominantly parallel and the WPB itself has a rod shape, whereas the left hand side of the same WPB becomes significantly wider and the tubules diverge from one another, giving them the appearance of "fanning out" from the more ordered section. Some tubules are orientated in parallel to the z axis, perpendicular to the other VWF tubules. Within the rod shaped region, the VWF tubules are broken into short, straight segments connected by kinks, rather than individual straight sections running

the length of the WPB, suggesting this region is also slightly disordered. From light microscopy of fusing WPBs, it has been reported that a transition state during fusion exists where the WPB is exposed to pH change, according to a pH-based increase in EGFP fluorescence, but still remains rod-shaped [26]. The low-level disordering and tubule bending and fragmentation seen in the rod-shaped part of the the WPB in figure 28 may represent the early stages of pH mediated disassembly before collapse. The local disruption suggests graduated disorder; becoming more disordered from right to left. The left-hand region, with greater disordered and shorter tubules would represent a more advanced stage of collapse. The proximity of the WPB to the edge of the carbon hole raises the question of whether the edge of the carbon plays a part in the WPB structure and subsequent collapse. This does not appear to be the case as the WPB is not constrained by the carbon, with disordered tubules both within the hole and over the carbon. In addition, the disruption of other cellular components by the carbon holes has not been observed, with the exception of filopodia extending away from the cell body and into holes.

In figure 29, a round WPB with few parallel VWF tubules is shown. Some tubules are running along the long axis, but there are also tubules perpendicular to this and at other angles in between. The visible parts of the membrane (not affected by the missing wedge) do not have any identifiable breaks or pores to suggest a fusion process. It is possible that it has fused and retracted, partially rearranging the VWF tubules. As EM images of pre-emergent and nascent WPBs post-Golgi [134] show rod-shaped organelles emerging from the TGN with parallel tubules, it seems unlikely that either of these WPBs were formed in a disordered way, and this disorder is most likely in reaction to fusion.

A candidate fusing WPB was also imaged in the HHMEC cells (figure 30). These cells were not stimulated to release WPBs, so like the inflated WPB in [4], this event is either basal WPB release or release in response to handling the cells before imaging. The WPB is unusual in that the VWF tubules are mostly running parallel to the z-

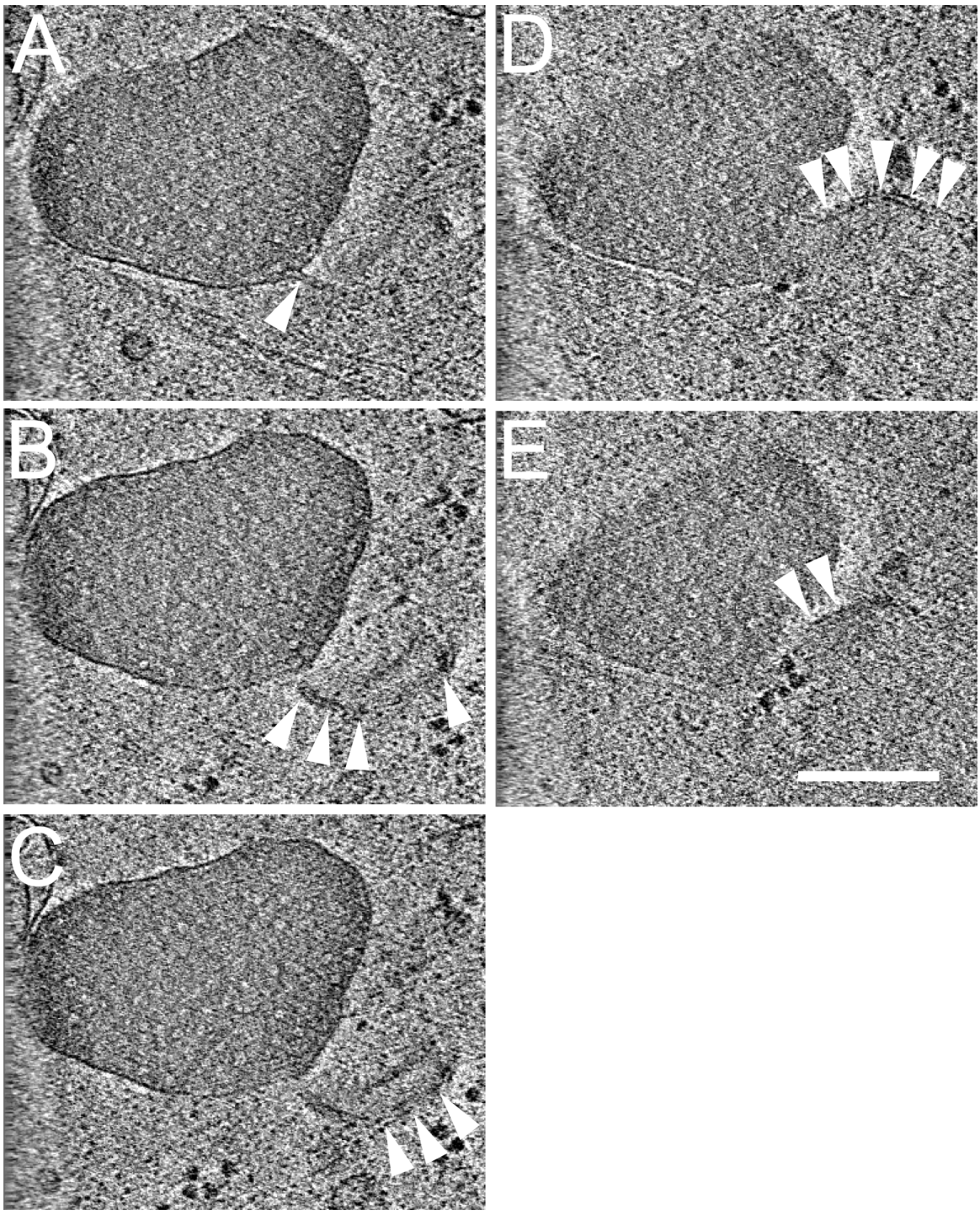

Figure 30: 5 slices through a tomogram of a HHMEC WPB with a stalk. The VWF tubules are predominantly "end-on", appearing as small, white circles. A long fusion stalk leaves the bottom of the WPB and loops back on itself, indicated with white arrowheads. ±60° tilt-series collected on an FEI Polara operating at 200 kV, -8 µm defocus. Scale bar: 200 nm.

axis and so are only observed in cross-section as circles. As in section 4.3, WPBs from HHMECs are expected to be rounded and disordered, so the determining feature for this WPB being involved in fusion is the long stalk protruding from the centre-bottom of the WPB. The stalk is very long, looping back on itself, making it more similar to the previously published WPB with a stalk (figure 7, [4]) than the WPB in figures 26 and 27. Again, it is not clear where the plasma membrane is in relation to the stalk. It is possible that, like the WPB in figure 26, the plasma membrane and fusion pore are in the XY plane and not visible in the tomogram due to the missing wedge.

Whilst cytoskeletal elements are present in the region of some of the fusing and disordered WPBs, none appear to be directly involved in the fusion process or forming a ring or coat around the WPB as previously proposed from fluorescence light microscopy experiments [74, 72], suggesting that additional force is not needed to expel VWF from fusing WPBs. In agreement with recent light microscopy experiments [30], the only method of fusion observed was the fusion of single WPBs. Neither compound fusion (multiple WPBs fusing at the same location) nor multigranular exocytosis [110] (multiple WPBs homotypically fusing into an intermediate secretory pod prior to relase from the cell) were observed, nor the homotypic fusion events prior to multigranular release.

4.6 Von Willebrand Factor helices within Weibel-Palade bodies

The packing of VWF within WPBs is interesting because the tubules make up only 44 % of the protein [4, 47]. In negative stain EM, the rest of the protein forms a dimeric bouquet, which is predicted to intercalate between the VWF tubules in the WPB ([137], figure 4).

To examine the relationship between the different tubules, models of the VWF helices within WPBs were manually built using IMOD (section 2.6.1). One ordered WPB that contained an internal vesicle (figure 31) and one disordered WPB (figure 32)

were modelled.

In figure 31, the ordered WPB model shows that in the rod-shaped region, the helices are closely packed. There is some tubule disorder in the clubbed-end containing an internal vesicle (discussed in chapter 5), with many short, fragmented tubules surrounding the vesicle.

In figure 32, a model for the VWF helices in the disordered WPB depicted in figure 28 is shown. Comparing this model with the model of the ordered WPB, the disordered region consists of many short, discrete tubules rather than the long tubules shown in ordered regions. In the bottom panel, where the model is imposed over a slice from the tomogram, the distance between the tubules and the membrane is also much greater than in the ordered model.

These models were used to analyse intertubule distances, using a MATLAB script from Dr Sebastian Wasilewski [4]. In the rod-shaped region of the ordered WPB, figure 33a shows a consistant intertubule distance of ~30 nm, corresponding with the large central peak in the histogram (figure 33b) for the bin 27.5–30 nm and the first 12 tubules plotted in figure 33c. These values are consistent with the previous 28.4 ± 3.13 nm mean measurement within an ordered WPB in [4]. In the area surrounding the vesicle, the tubules are disordered and fragmented, leading to larger intertubule distances. Within the disorder, it is also harder to trace the tubules, as there are many shorter segments and becauses the tubules aren't parallel, it is hard to view more than one at a time in cross-section. Omitted tubules will skew the measured distance, making the distance appear larger. Short, consecutive lengths of disordered tubules also distort some of the distance measurements as the ends of two tubules can come much closer together than their radial distance, and a model with many short tubules increases the number of tubule ends. The overall mean distance for the ordered model is 29.7 ± 4.4 nm.

In figure 34, the same parameters were calculated for the disordered model. Both the colour variation in panel a and the wide histogram peak indicate the large vari-

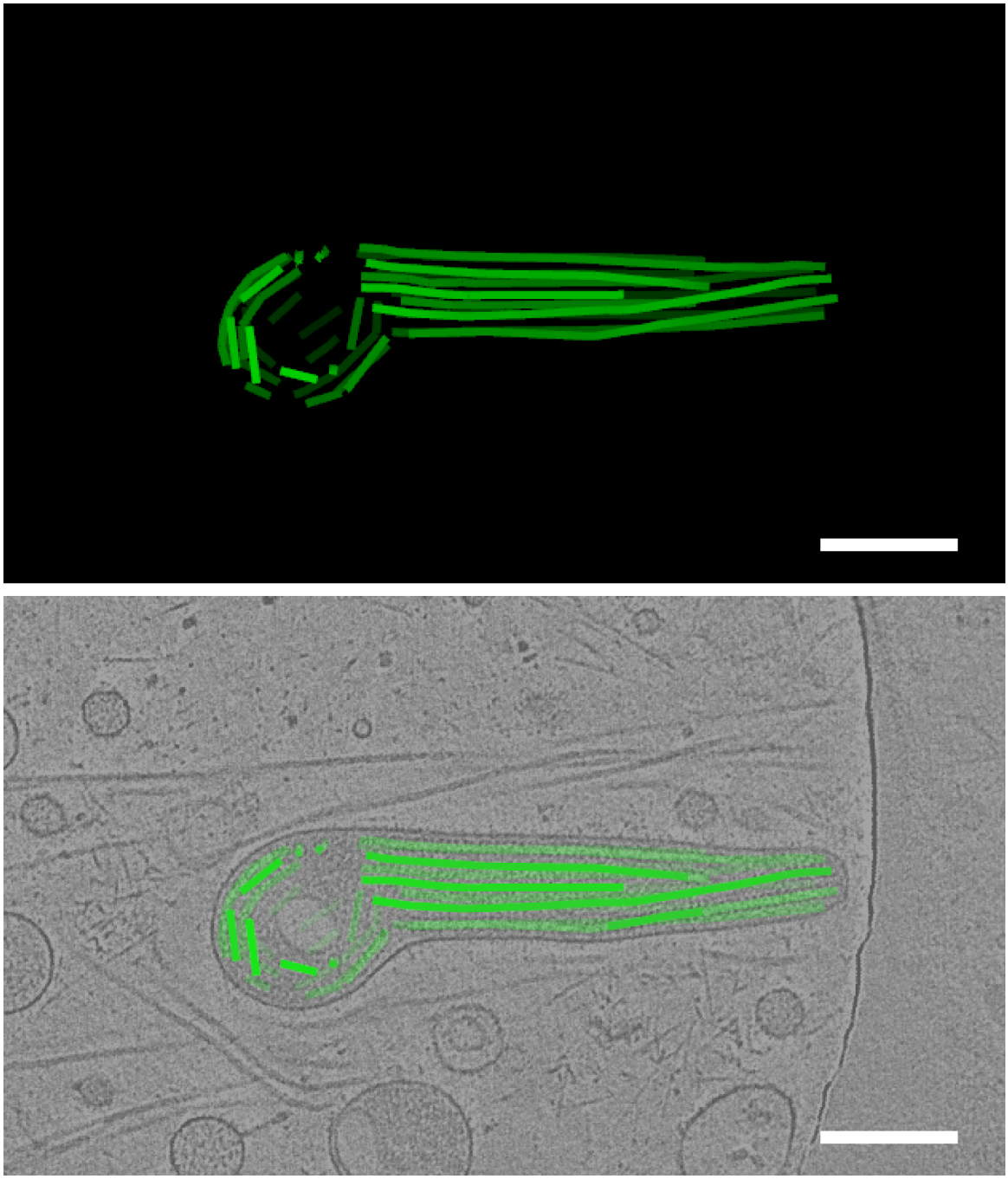

Figure 31: 3D model for VWF tubules within an ordered WPB. The top panel shows the model alone and the bottom panel includes a slice of the tomogram showing the helices and the WPB limiting membrane. Short sections of VWF tubule pack around the internal vesicle. Contrast in the lower panel is reduced due to model depth cueing. Scale bar: 200 nm

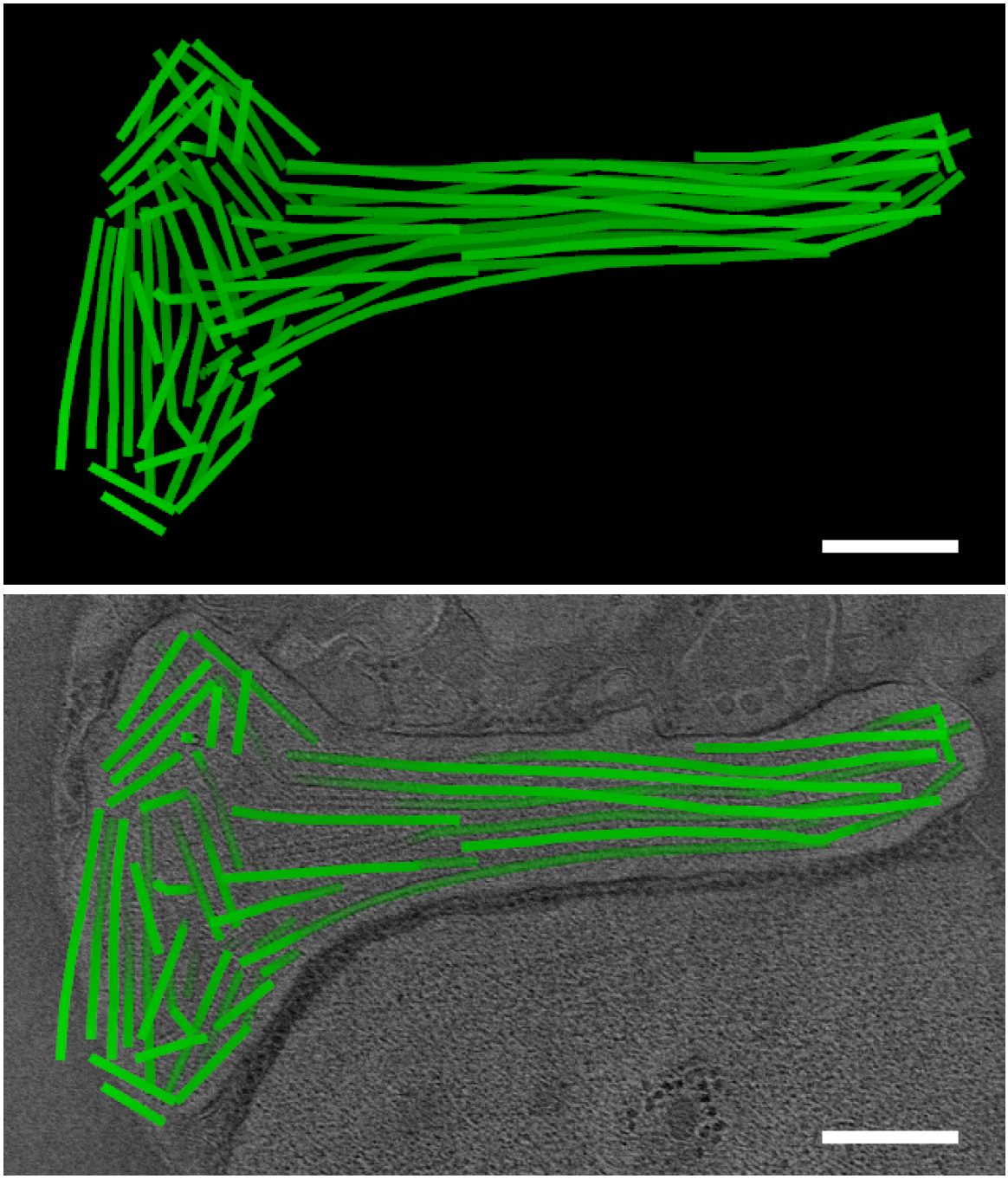

Figure 32: 3D model for VWF tubules within a disordered WPB. The top panel shows the model alone and the bottom panel includes a slice of the tomogram showing the helices and the WPB limiting membrane. Contrast in the lower panel is reduced due to model depth cueing. Scale bar: 200 nm

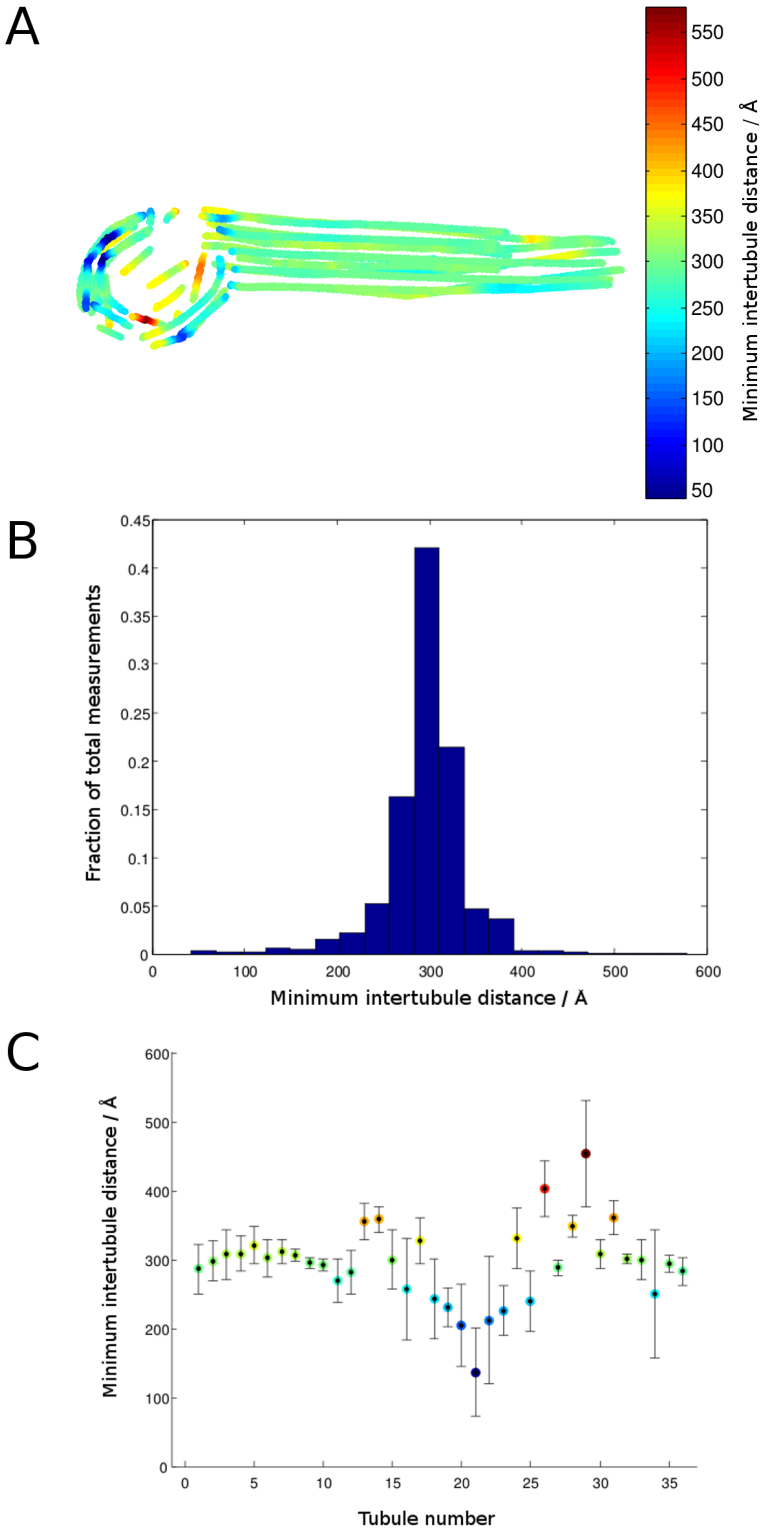

Figure 33: **A**: VWF tubule within an ordered WPB, coloured to show the minimum distance to a neighbouring tubule. Distances are displayed in Å. **B**: Histogram of minimum intertubule distances from the model. Distances are sampled every half pixel and frequency is expressed as fraction of total measurements. **C**: Plot of the mean and standard deviation of the measurements, averaged for each individual tubule.

ation in distances in the this model. In the left hand, disordered region, the ends of the tubules are a dark blue, indicating a small distance where the intertubule axial rather than radial distance is being calculated. The histogram peak is at the 32.5–35 nm bin, indicating an increase in the modal intertubule distance between the ordered and disordered WPB models. The large increase in variability between the two models is expected and can be used as a measure of WPB order, as the increasing intertubule distance variation is a consequence of non-parallel packing, whereas two parallel tubules have no change in distance. The overall mean distance for the disordered model is 31.9 ± 7.2 nm. An increase in intertubule distance fits with previous observations of a WPB appearing to swell into a "marrow" shape upon beginning to fuse [4].

Using the increased intertubule space observed in disordered WPBs, combined with cryo-electron tomography allows individual tubules to be extracted and examined in 3D. 55 tubules from the tomogram in figure 28 were extracted using the program *Cylinder* (obtained from Dr Sebastian Wasilewski). This program takes the x,y,z coordinates for the centre of the start and finish of each section of tubule and outputs a 20 px radius cylindrical subtomogram between those points. 3D reconstruction of the WPB followed by tubule extraction is neccessary as the 3D tubule arrangement means tubules overlap when projected in 2D. The individual tubule tomograms were then projected in 2D to give a non-overlapping set of 2D projections with no missing wedge effect, and padded into a 2048×2048 px box. The sum of the FFTs of all 55 tubules is shown in figure 35. The FFT clearly shows the helical repeats of VWF and indicates the potential for a low resolution VWF reconstruction from tubules within WPBs. Cutting each 2D tubule projection into 32×32 px boxes gave a data set for calculating a 3D helical reconstruction. 3D reconstruction from the 2D projections is possible as the helical symmetry means that even a single image is sufficent to reconstruct the tubule [18]. Averaging of subtomograms in 3D is another possible approach, which requires alignment of the volumes in 3D and will be worthwhile with

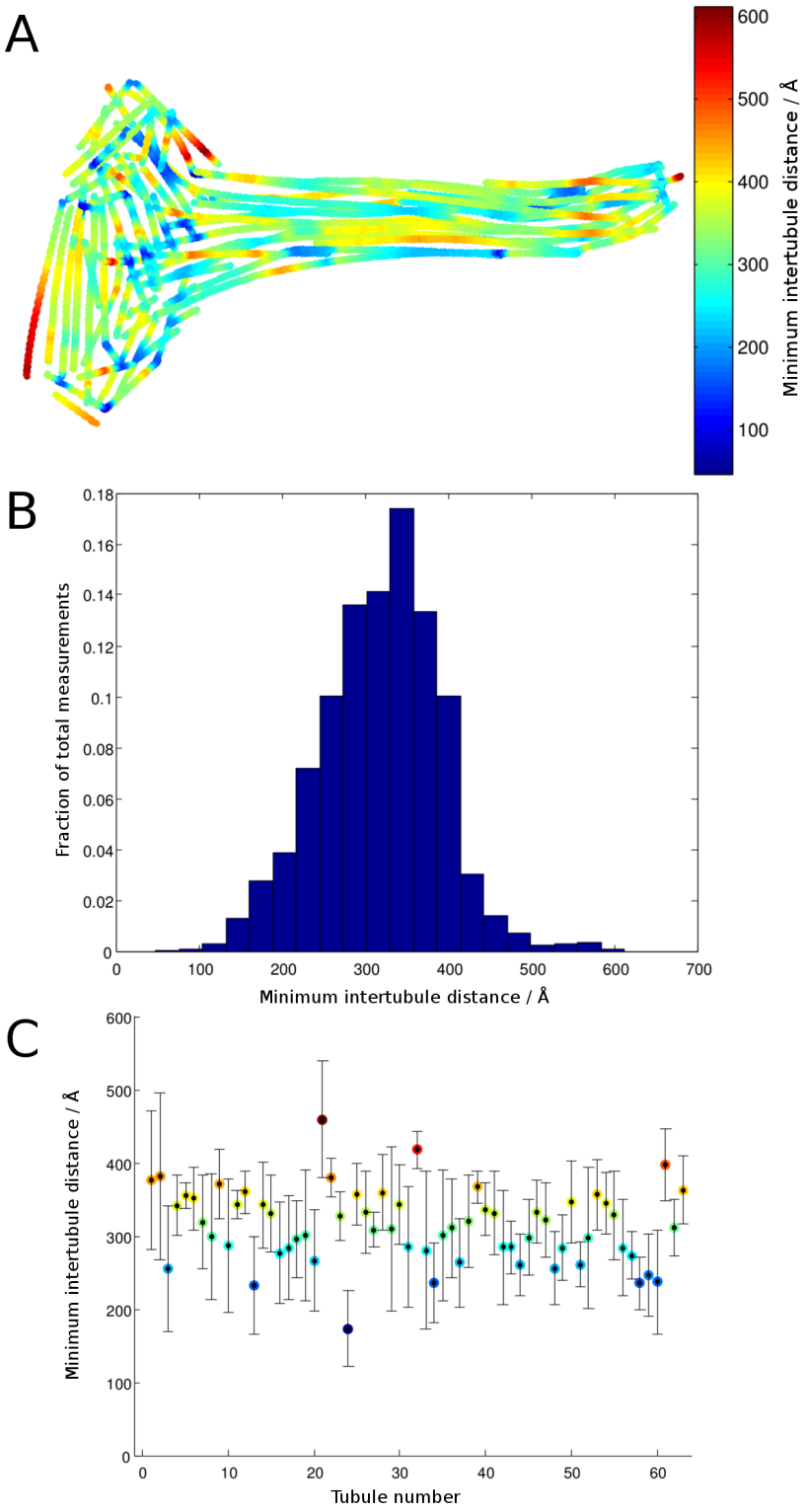

Figure 34: **A**: VWF tubule within a disordered WPB, coloured to show the minimum distance to a neighbouring tubule. Distances are displayed in Å. **B**: Histogram of minimum intertubule distances from the model. Distances are sampled every half pixel and frequency is expressed as fraction of total measurements. **C**: Plot of the mean and standard deviation of the measurements, averaged along each individual tubule.

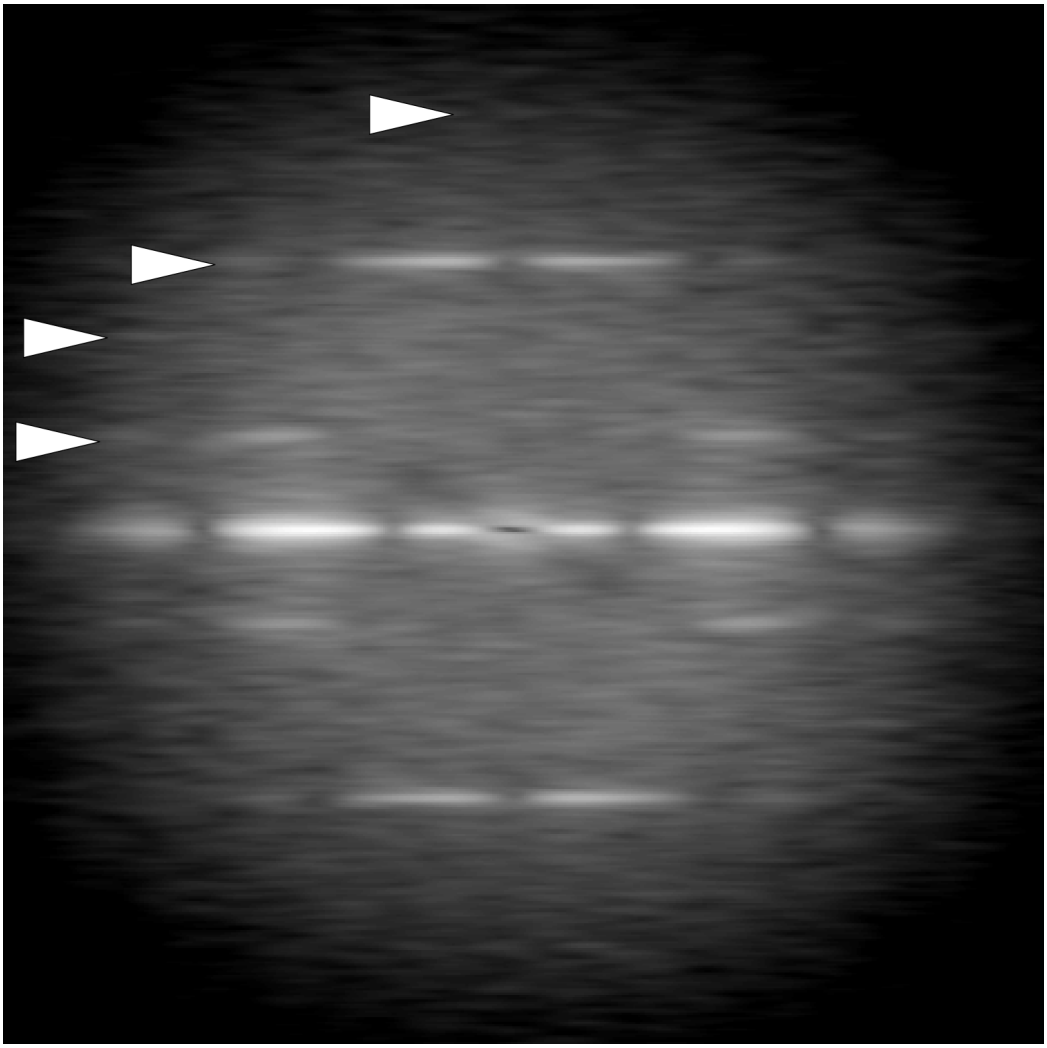

Figure 35: Average FFT of 55 VWF tubules extracted from a tomogram and padded to 2048×2048 px. Arrows indicate repeats at 77, 119, 165 and 337 Å.

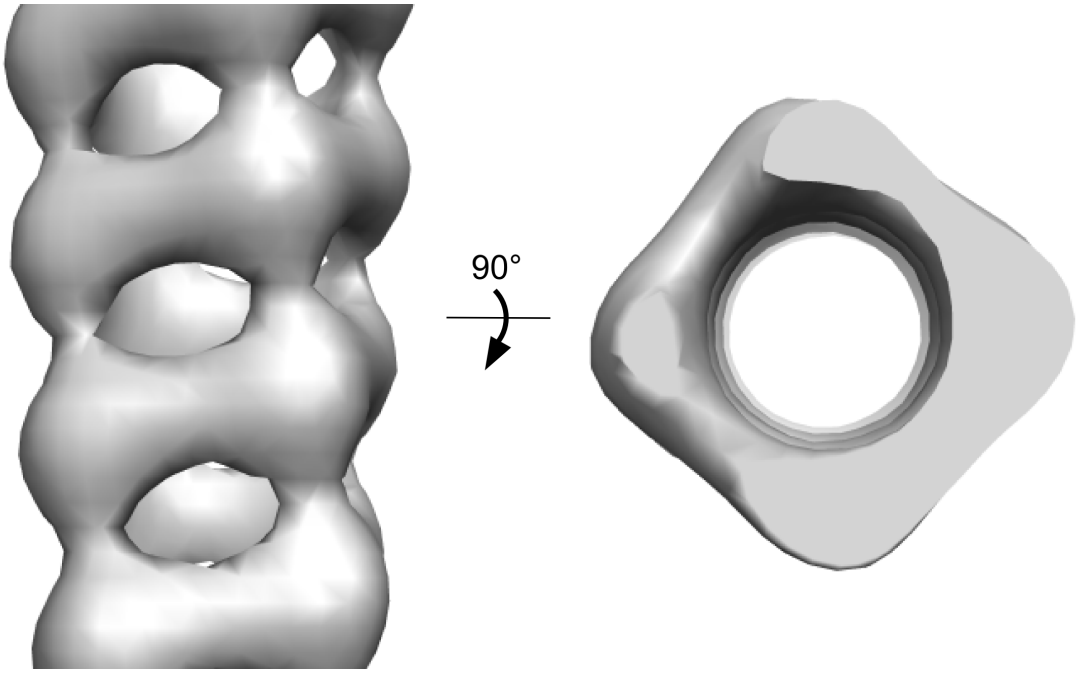

Figure 36: A 3D model for a VWF helix, obtained by helical image processing of 2D projections from tubule subtomograms.

a larger dataset.

Images were aligned and classified in IMAGIC-5 [113], and helical processing and 3D model calculation took place in Tigris (package from Dr Tim Grant), using the symmetry parameters defined in [4] for the initial reconstruction. Handedness was assigned as right-handed, as previously determined by quick-freeze deep-etch EM [47]. The handedness of the VWF tubules is also visible in the raw electron density of the extracted subtomograms. The side and top views of the reconstruction are shown in figure 36. The model is similar to both the previous full-length VWF model from a single, computationally extracted tubule in cryo-EM [4] and negative stain EM D1D2D'D3 truncation model [47], with a resolution similar to [4] and less than [47]. This model will be improved by adding data from additional disordered tomograms. Increasing the box size may help to visualise the radiating C-terminal arms, however this will mean utilising models of the VWF helices within disordered WPBs (figure 32) to select only the tubules that are well separated from neighbouring tubules, to ensure that each extracted cylinder only contains density from a single tubule.

Subtracting the tubule radii (~12.5 nm) for each tubule from the centre-to-centre distance means that the actual space between the tubules at its minimum is only 4.7 nm in ordered WPBs. The linear length of the C-terminal bouquet predicted to occupy this space is ~51 nm excluding the A1 domain [137]. The A1 domain is surrounded by flexible linkers, meaning it does not appear in negative stain EM class averages, and the "stem" region of the bouquet is also flexible, with the CK domain appearing at multiple different positions relative to the D4 domain in class averages. By looking at the ordered WPB in cross-section in figure 37, some larger spaces between the tubules can be seen. The high degree of flexibility must allow the bouquet to bend into the larger spaces between tubules. Like in negative stain EM, the bouquets must pack in a variable manner, as they do not appear with the same helical order as the tubules when averaging.

From looking at individual VWF tubules in disordered WPBs, some densities appear to be protruding from the main helix. A section of a single slice through the tomogram in figure 29 is shown in figure 38. Each VWF tubule has small lines of density, extending radially from the tubule in the space between adjacent tubules. Despite being only ~20 nm in length compared to the C-terminal bouquet length of 51 nm from A2-CK domain [137], its location does suggest that these extensions are part of a C-terminal 'arm', even if the complete bouquet is not seen. The highly flexible nature of the bouquets suggests that they could be partially "wrapped" around the tubule, with only a small portion visible as an arm. Two of the arms in figure 38 appear to fork close to the tubule. This split is predicted as the flexible A1 domains form the "head" of the bouquet at the interface between the bouquet and the D3 domain which forms part of the helix (figure 4). Individual arms are not visible in rod-shaped WPBs, suggesting that they are too tightly packed to be seen individually in ordered WPBs and that the increased intertubule distance within disordered WPBs allows individual arms to be seen.

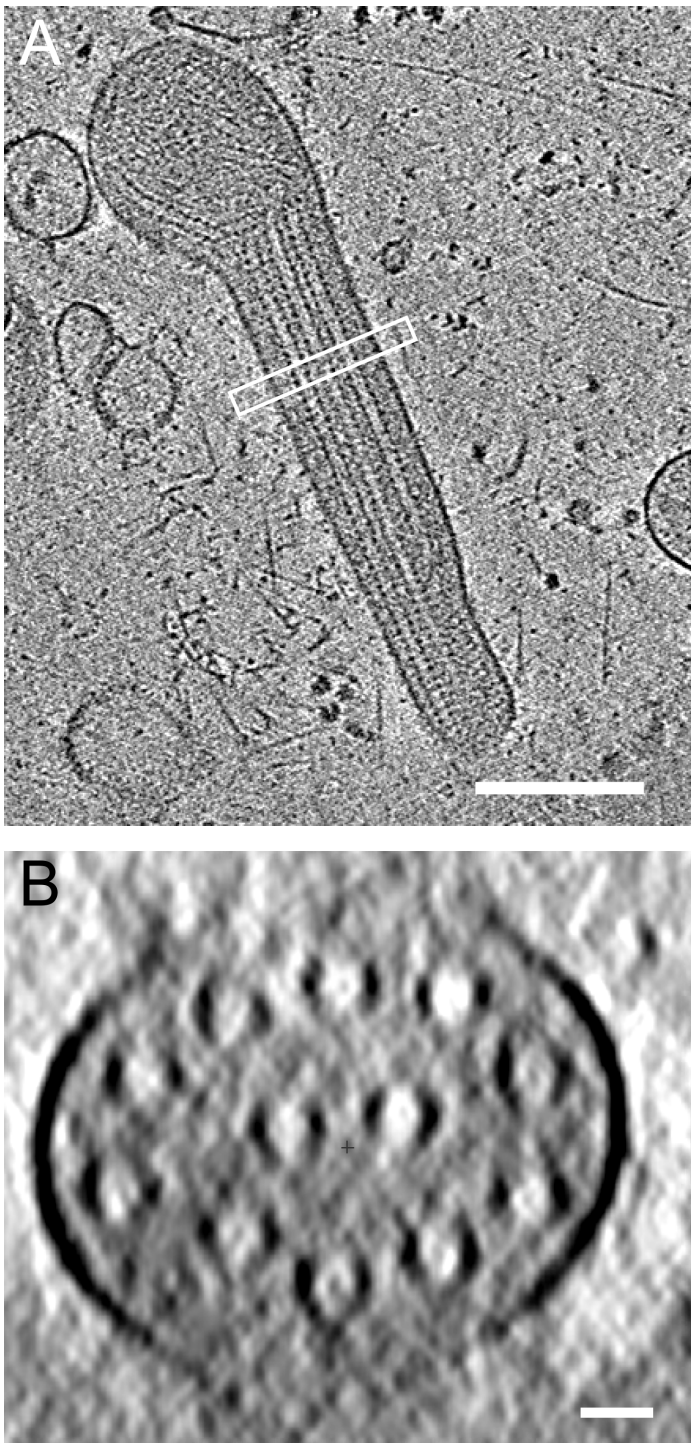

Figure 37: WPB and VWF helices in cross-section. **A**: Slice through tomogram showing the ordered, rod-shaped region of a WPB. Scale bar: 200 nm. **B**: Cross-section through the tomogram shown in A, at the boxed region. The cross-section shows 12 VWF helices within the WPB limiting membrane. Scale bar: 20 nm. ±60° tilt-series collected on an FEI Spirit operating at 120 kV, -8 µm defocus.

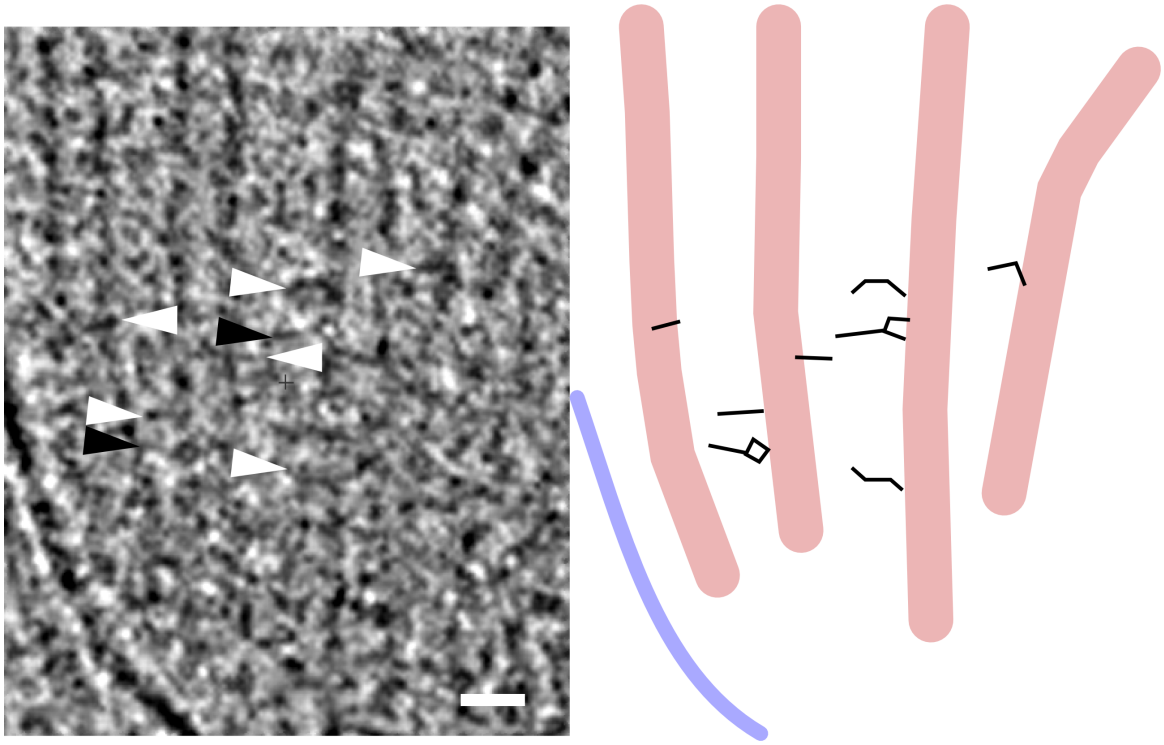

Figure 38: Slice through the tomogram shown in figure 29, depicting VWF tubules with radial densities protruding from it them. On the left the densities are marked with arrowheads. Black arrowheads show densities that fork at the tubule, as expected for the C-terminal bouquets. On the right is a traced schematic of the image, indicating the VWF tubules in pink, the WPB membrane in blue and the indicated densities in black. Scale bar: 20 nm

4.7 Conclusion

In this chapter, the correlation between WPB size, shape and the distribution of VWF tubules has been examined, using stimulation by secretagogues, hypotonic shock and cells that endogeneously make round granules to look at a variety of WPB shapes. Instances of stimulated WPB exocytosis have also been imaged. Imaging of round WPBs from all conditions has demonstated that they contain VWF tubules which are more separated than in ordered, rod-shaped WPBs. Building models of the VWF helices in different states of order allows quantification of the different intertubule distances and suggests how the tubules behave during the transition from storage to disassembly and VWF release. The increased intertubule distance has allowed the C-terminal "arms" to be imaged for the first time.

Subtomographic averaging of the VWF tubules is possible, shown by the FFT of extracted tubules with a strong helical repeat. To go beyond the VWF tubule and examine the head or stem of the bouquet structure however, requires a higher resolution reconstruction and will only be possible if the ordering of the bouquet is sufficient to allow a helical averaging approach to be used.

5 Discovery of a novel, CD63-containing internal vesicle in Weibel-Palade bodies

5.1 Introduction

Whilst the primary cargo of WPBs are VWF tubules [28, 123], WPBs contain many minor components; both membrane associated and soluble proteins within the lumen of the organelle. Some of these components are recruited when the WPB forms at the TGN, whilst others are delivered to the maturing WPBs post-Golgi. A list of these components and their recruitment point is shown on page 18, table 1.

CD63 is a ubiquitously expressed membrane tetraspanin commonly present at the cell surface and in lysosomes and late endosomes [83]. The role of the tetraspanin family is thought to be in organising membrane proteins [83]. In endothelial cells, CD63 is found in WPBs [119], where it is delivered post-Golgi in an AP-3 [43] and annexin A8 [82] dependent process via endosomes.

The presence of CD63 (also known as LAMP-3, lysosomal-associated membrane protein 3), together with their acidic pH, indicates the WPBs are lysosome-related organelles [19]. Lysosome-related organelles are a group of storage and secretory granules that share similar properties (such as pH and transmembrane proteins) with lysosomes. Other lysosome-related organelles include: melanosomes, platelet dense granules and basophil granules [19].

Upon release from WPBs, CD63 acts as a cofactor at the endothelial cell membrane for another WPB membrane protein; P-selectin [22]. P-selectin is a proinflammatory membrane protein stored in WPBs that when delivered to the endothelium acts as a receptor for leukocytes, causing them to adhere to the vessel wall [35]. CD63 and P-selectin co-cluster at the cell surface upon release from WPBs, and knockdown of CD63 reduces P-selectin levels at the cell surface [22], indicating its role as a cell surface co-factor. Knockout of annexin A8, a protein responsible for delivering CD63 from endosome to WPBs, affects both P-selectin levels at the cell surface and the

ability to recruit leukocytes [82] also shows the importance of CD63 for P-selectin levels at the cell surface. Therefore, CD63 has an indirect role in inflammation, hence its presence on WPBs.

In late endosomes/multi-vesicular bodies, CD63 is enriched within the intraluminal vesicles (ILVs) compared to the limiting membrane of the endosome [83]. MVB ILVs are formed by the invagination of the limiting membrane of endosomes, selectively bringing lipids, membrane proteins and ubiquitinated proteins for lysosomal degredation into the MVB [80]. Alternatively, the ILVs are released by fusing the MVB limiting membrane to the plasma membrane, releasing the complete ILVs into extracellular space [20, 86].

Release of whole vesicles into the extracellular space is called exosomal release, with the vesicles known as exosomes. In exosomes from human B-lymphocytes, CD63 is enriched compared to transferrin receptor, a plasma membrane and early endosome marker [27].

In this chapter, a vesicle within WPBs is shown by cryo-EM. The vesicle is present across different cell lines and conditions. Light microscopy studies by Dr Ana Violeta Fonseca identified an CD63-enriched area within WPBs consistant with the vesicle observed by cryo-EM and in 3D by cryo-ET. FRAP (fluorescence recovery after photobleaching) experiments indicate that the CD63-enriched membrane is not part of the outer limiting membrane of the WPB.

5.2 WPBs contain an internal vesicle

WPBs across both cell lines and all conditions showed a membrane limited vesicle within the WPB. Areas where a vesicle was indicated in 2D images were specifically targeted for tomography, leading to 13 tomograms of vesicles within WPBs. Slices through selected tomograms of WPBs containing vesicles in different conditions are shown in figures 39–45.

In most cases, the internal vesicle does not have any large or distinct contents

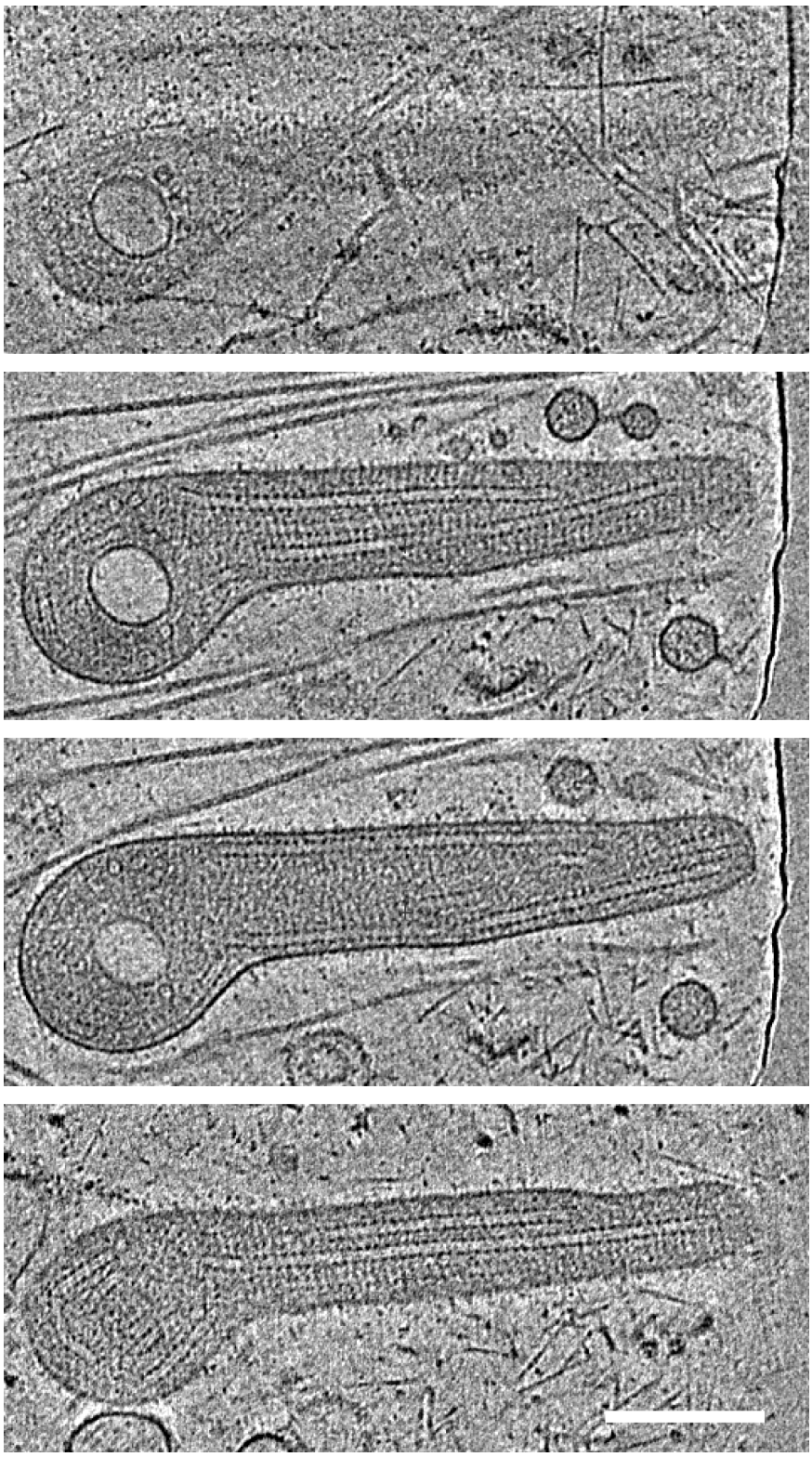

Figure 39: Slices from a tomogram at different z heights of a WPB containing an internal vesicle from a HUVEC stimulated with 0.3 µM ionomycin. The first panel shows the proximity of the internal vesicle to the WPB limiting membrane. ±60° tilt-series collected on an FEI Spirit operating at 120 kV, -8 µm defocus. Scale bar: 200 nm.

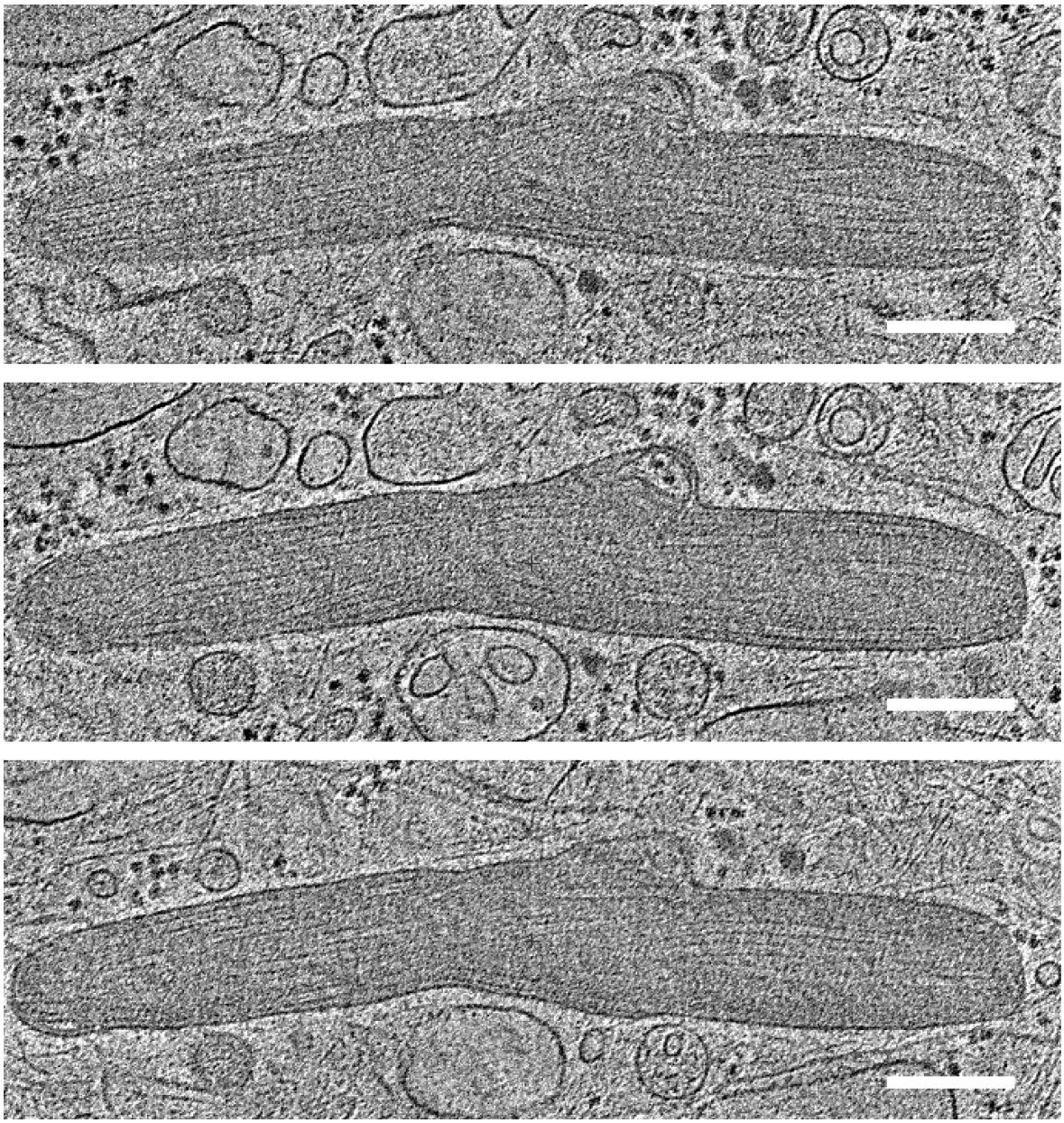

Figure 40: Slices from a tomogram at different z heights of a WPB containing an internal vesicle from a HUVEC stimulated with 0.3 µM ionomycin. In the middle panel, there are two electron dense particles within the internal vesicle, similar to those surrounding the WPB. ±60° tilt-series collected on an FEI Polara operating at 200 kV, -7 µm defocus. Scale bar: 200 nm.

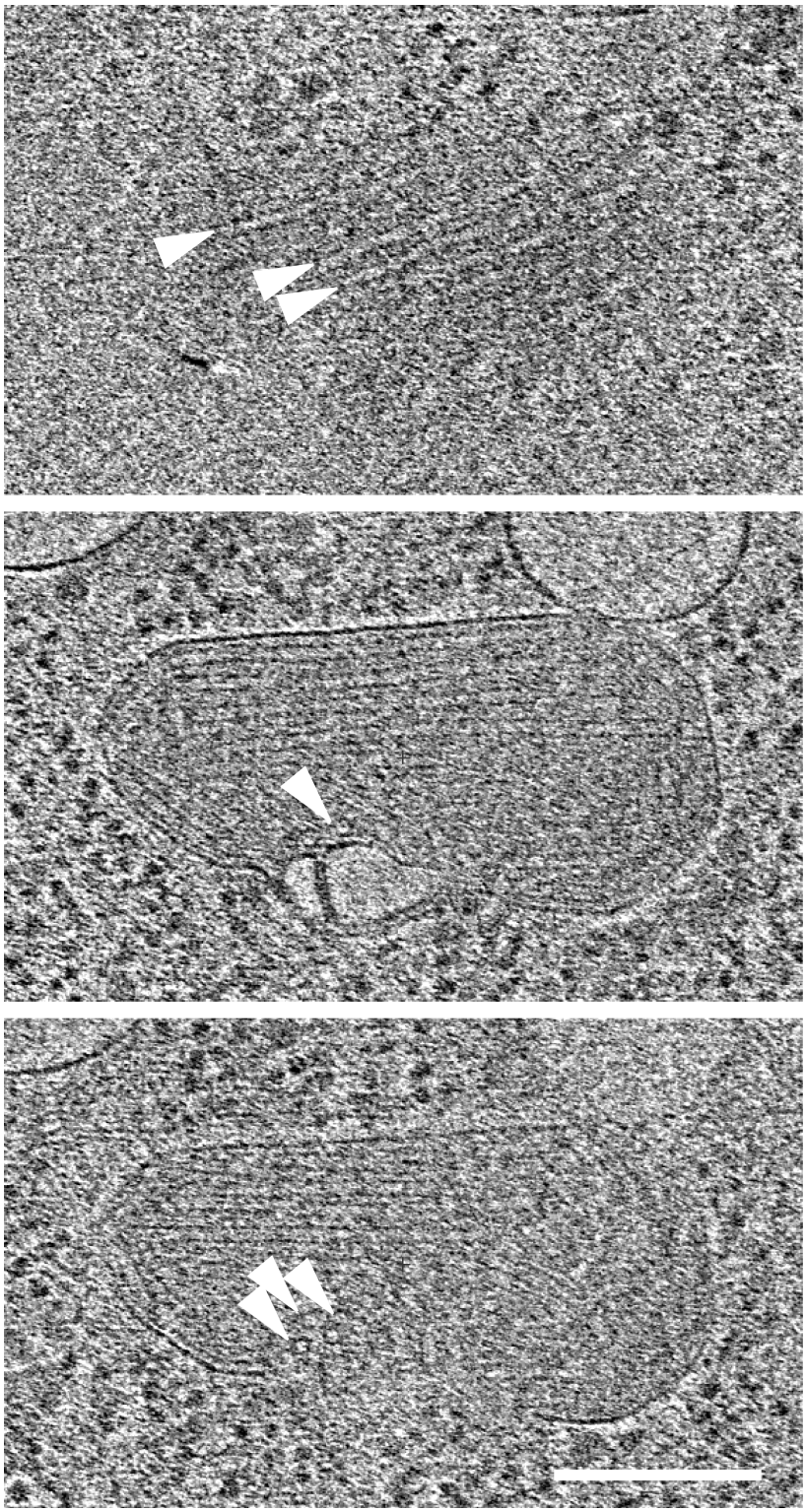

Figure 41: Slices from a tomogram at different z heights of a WPB containing 2 internal vesicles from a HUVEC stimulated with 1 µM ionomycin. In the top panel, VWF tubules at the top of the WPB are indicated with arrowheads. In the middle and bottom panels, disrupted, end-on VWF tubules in the region of the two internal vesicles are indicated. -60° – +39° tilt-series collected on an FEI Polara operating at 200 kV, -4 µm defocus. Scale bar: 200 nm.

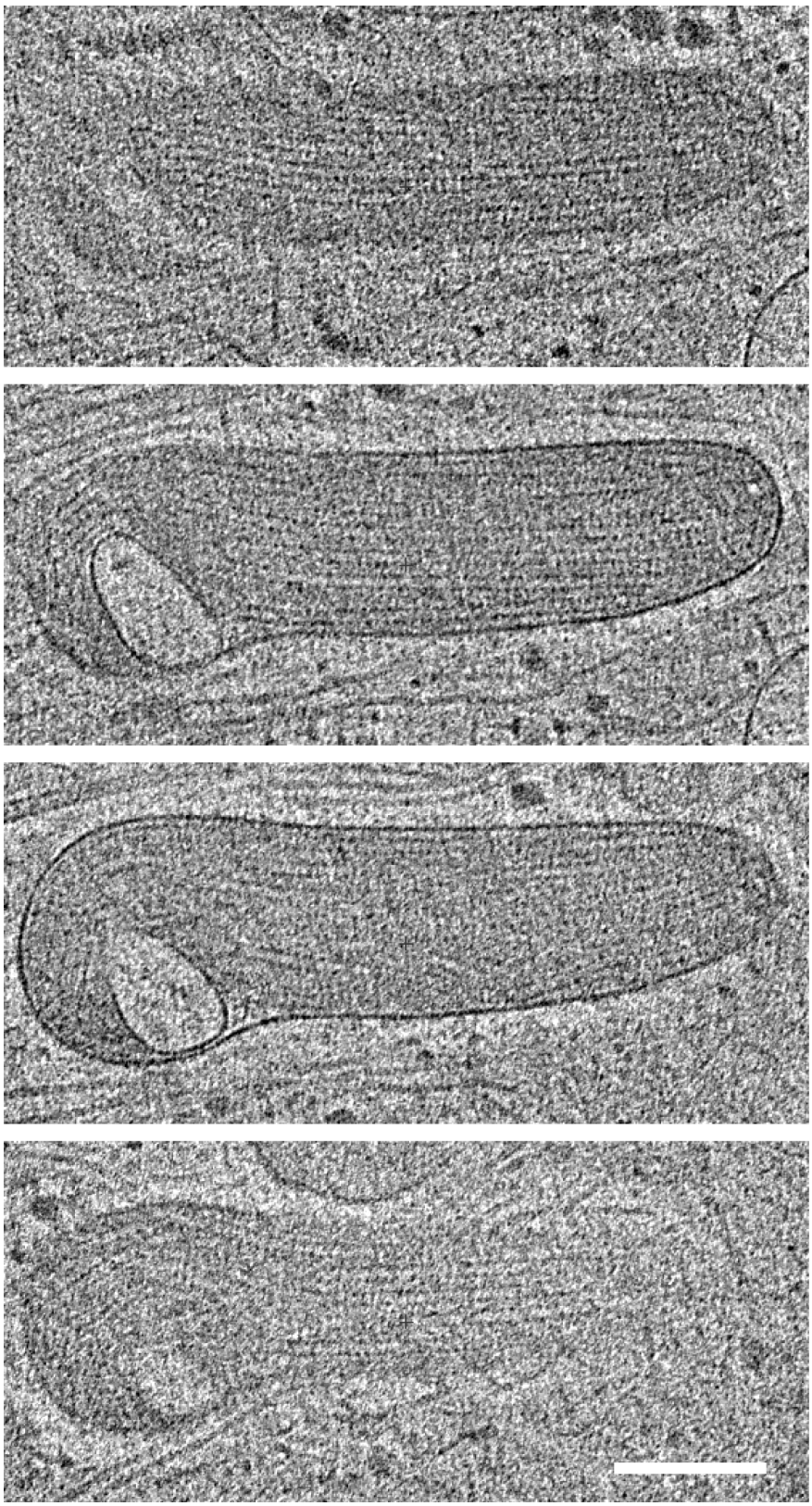

Figure 42: Slices from a tomogram at different z heights of a WPB containing an internal vesicle from an unstimulated HUVEC. $\pm 60^{\circ}$ tilt-series collected on an FEI Spirit operating at 120 kV, -8 µm defocus. Scale bar: 200 nm.

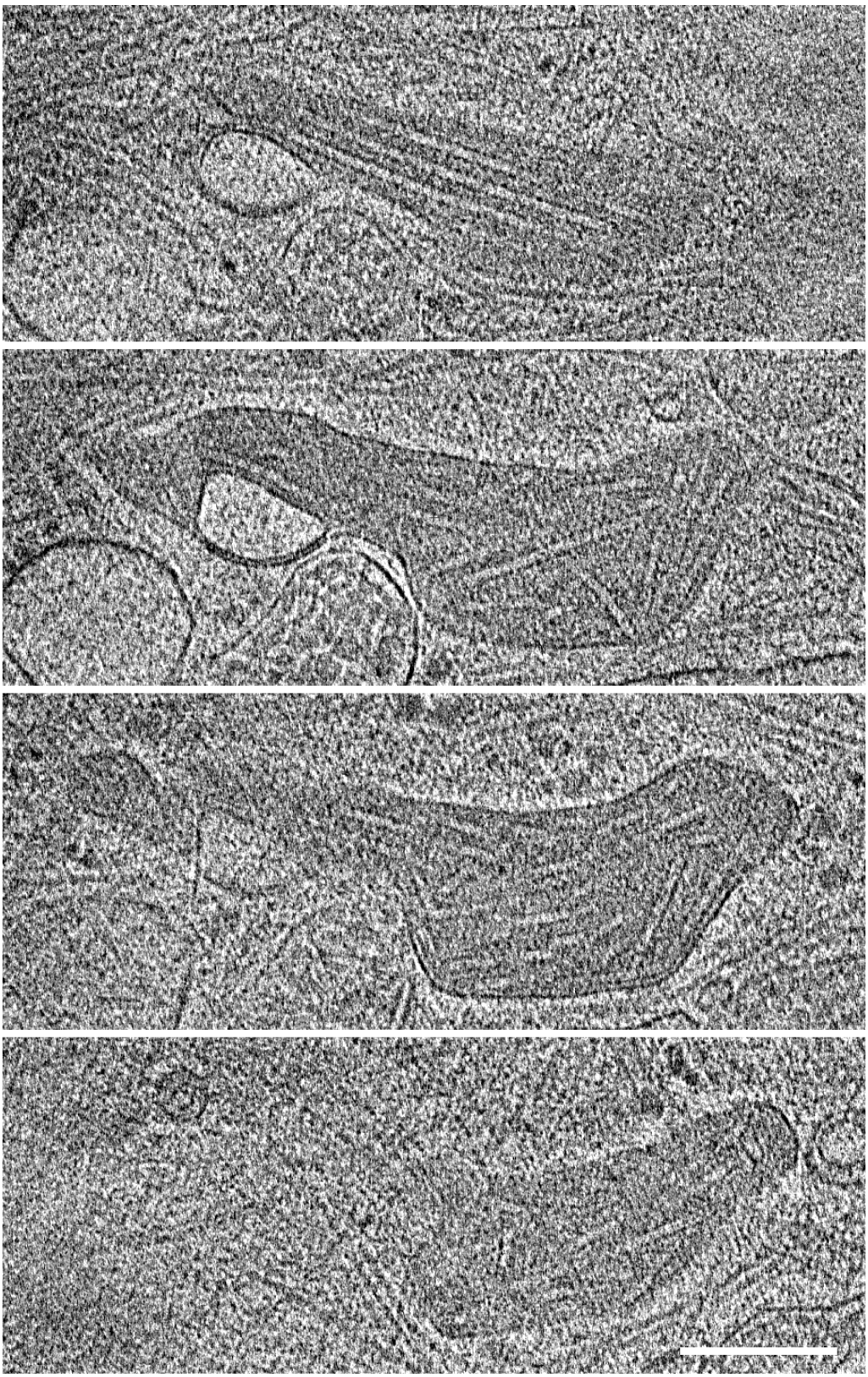

Figure 43: Slices from a tomogram at different z heights of a WPB containing an internal vesicle from an hypotonic shocked HUVEC. $\pm 60^{\circ}$ tilt-series collected on an FEI Polara operating at 200 kV, -8 µm defocus. Scale bar: 200 nm.

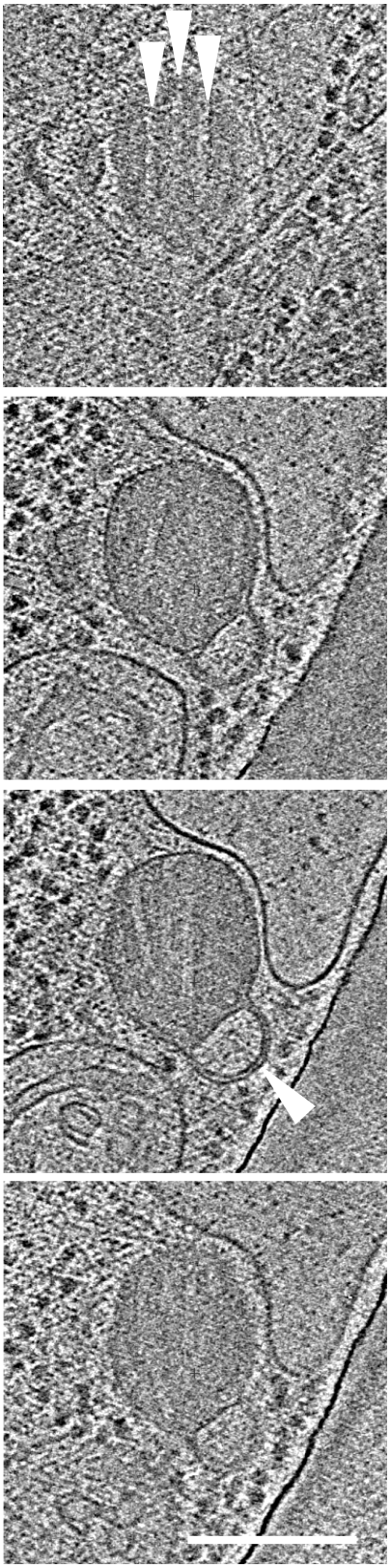

Figure 44: Slices from a tomogram at different z heights of a WPB containing an internal vesicle from a HHMEC. The top panel shows 3 short, parallel VWF tubules. In the third panel, it is clear that the limiting membrane and vesicle membrane are close but separate. $\pm 60^\circ$ tilt-series collected on an FEI Polara operating at 200 kV, -8 µm defocus. Scale bar: 200 nm.

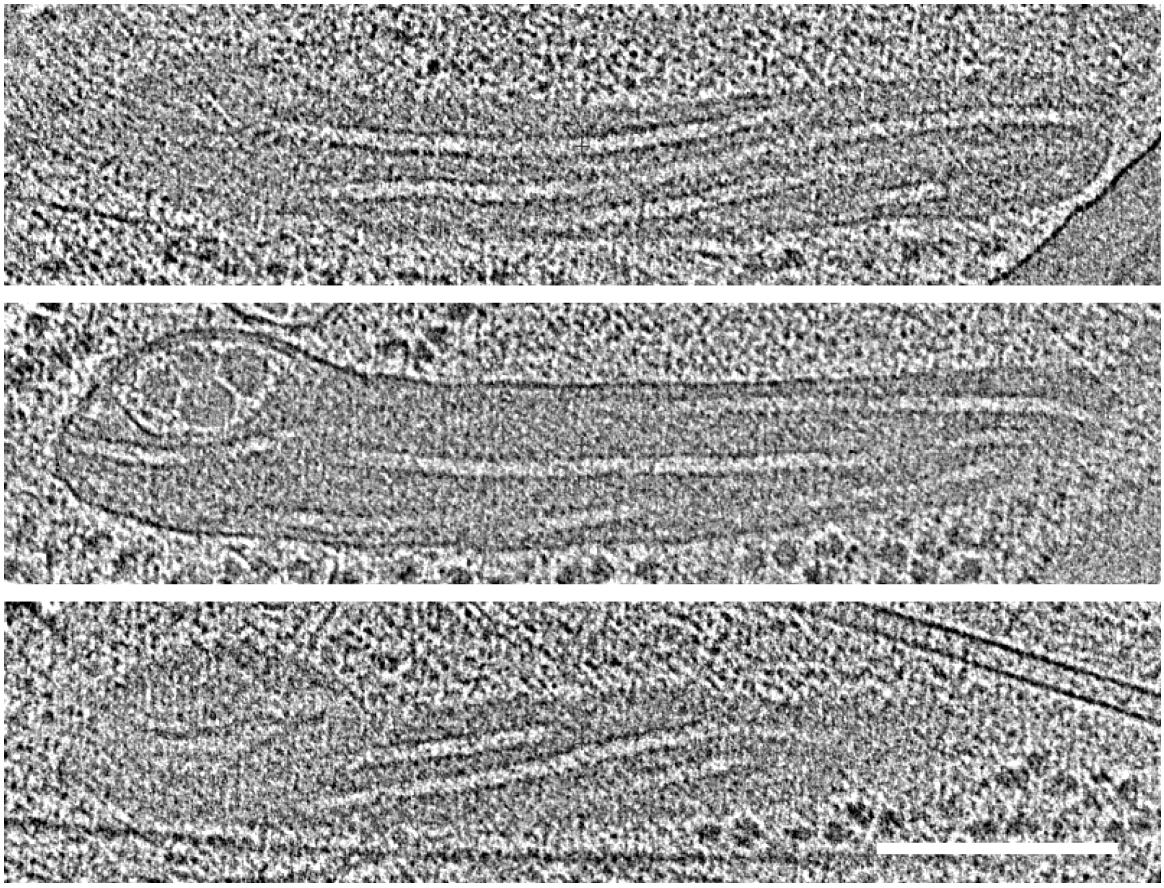

Figure 45: Slices from a tomogram at different z heights of a WPB containing an internal vesicle from a HHMEC. The middle panel shows that the vesicle has 4 electron dense objects within it. -60° – +42° tilt-series collected on an FEI Polara operating at 200 kV, -8 µm defocus. Scale bar: 200 nm.

and is less electron dense than the surrounding VWF, however 2 vesicles; from an ionomycin stimulated HUVEC (figure 40) and from an HHMEC (figure 45) appear to contain some distinct objects.

The location of the vesicle within the WPB can vary. The most common location for the vesicle is centred on the short axis and towards one end (figure 39), however vesicles can also be present at the side (figures 40 and 41) or protruding from the end (figure 44). In all circumstances, the internal vesicle is close to the limiting WPB membrane in one axis. The number of vesicles within a single WPB can also vary, such as the 2 vesicles within the WPB in figure 41. In many cases, the vesicle appears to deform the WPB end in to a "clubbed" shape, which has a disrupting effect on the tubules (figure 39), with the vesicle surrounded by short and bent tubules when compared to the rod-shaped portion of the WPB. In the second and third panels of figure 39 and figure 41, some end-on tubules either side of the vesicle can be seen, emphasising the local deviation from parallel packing around the vesicle. The rod-shaped portion of the WPB remains tightly packed with parallel tubules and a small intertubule distance, evident from the tubules in figure 39 and demonstrated by the WPB model in chapter 4.

Using the library of 535 2D WPB images obtained in chapter 4, the vesicles occur within WPBs with a prevalance rate of 12.0 % (64 internal vesicles). Although it is hard to determine the presence of an internal vesicle in 2D, the striations of VWF helices and the limiting WPB membrane can indicate a presence. In 2D images where a vesicle was indicated and the same area has been reconstructed in 3D, a vesicle was always present in the reconstruction.

The internal vesicles of WPBs appear very similar to the internal vesicles within multivesicular bodies in HUVECs, as shown in figure 46. In this image, the WPB contains 3 ILVs and is surrounded by several vesicles each containing at least one other vesicle. The non-spherical shape and electron density in both the WPB vesicle and the other ILVs are comparable.

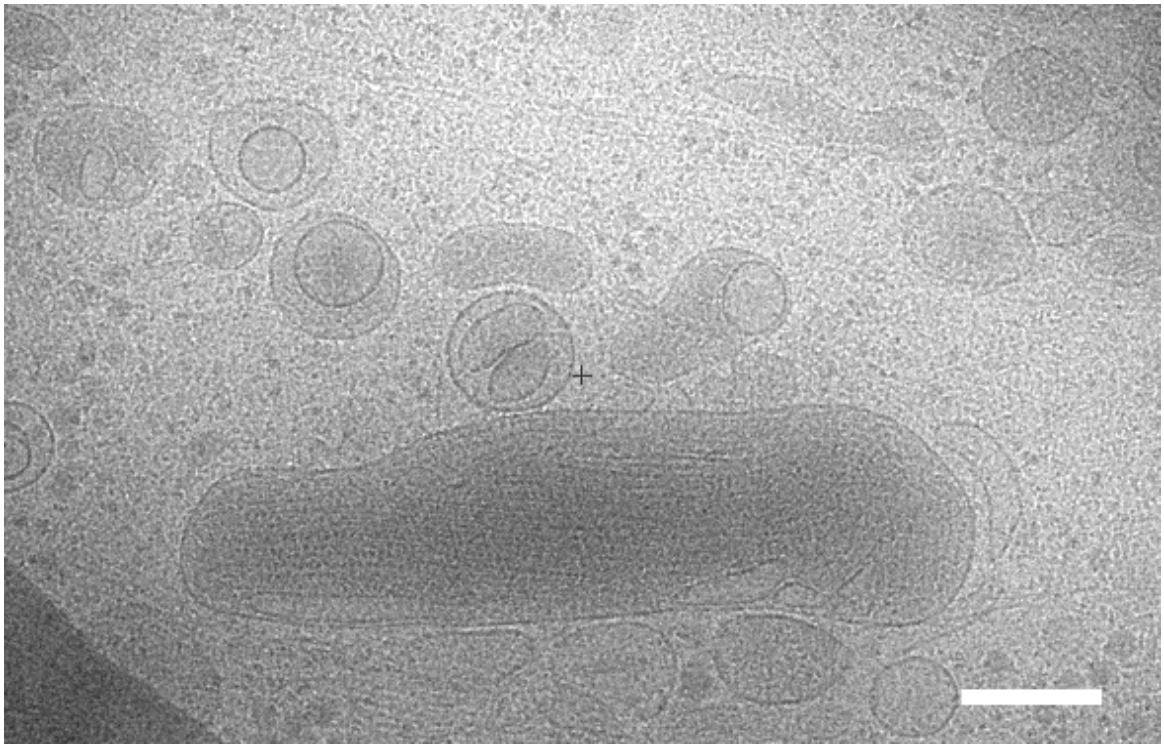

Figure 46: 2D image from an unstimulated HUVEC showing a WPB with multiple ILVs surrounded by other MVBs. Scale bar: 200nm.

The presence of an internal vesicle within WPBs has not been previously reported. It is a feature that is only accessible by EM studies and one reason it may have been previously overlooked is that it requires cryo-electron tomography of whole mount cells to best visualise whole WPBs in 3D, and this technique has not been widely used to study WPBs. The internal vesicles are a persistant feature of WPBs in this study, being present in all conditions and cell lines imaged, suggesting their ubiquity.

Internal vesicles have also been found using EM within a number of other lysosome-related organelles such as melanosomes [49] and platelet α-granules [114]. It is interesting that platelet α-granules can contain internal vesicles as these granules are similar to WPBs as they can contain VWF tubules, however VWF and internal vesicles were not shown in the same granule. The presence of an internal vesicle may be another feature indicating lysosome-related organelle status, in addition to acidic pH and presence of CD63 and further demostrating the link between the MVBs in the endocytic pathway and the secretory storage properties of WPBs.

5.3 A pool of CD63 is present within WPBs, separate to the limiting membrane

Fluorescence microscopy images of antibody-stained HUVECs show CD63 colocalising with VWF in rod-shaped WPBs (figure 47, top left). In up to 5 % of WPBs, the CD63 fluoresence contains a bright spot, indicated by the arrowheads in figure 47 and the inset zoomed panels a and b. The size and position of the CD63 bright spot within the WPBs can be at either tip or side (figure 47 top right). This positioning of the bright spot is consistent with the location of the vesicles imaged by cryo-EM (figures 39 - 45). CD63 bright spots are present when either EGFP-CD63 or antibody-labelled endogenous CD63 is imaged (data not shown).

To investigate if the observed EGFP-CD63 bright spots were due to local enrichment of EGFP-CD63 on the limiting membrane of WPB or EGFP-CD63 in the membrane of a separate, internal vesicle within the lumen of the WPB, FRAP (fluorescence recovery after photobleaching) experiments were carried out (figure 47, bottom panels). CD63 is highly mobile within WPBs and the plasma membrane, with previous FRAP experiments on the limiting membrane of WPBs showing recovery of fluorescence within the bleached region in <20 s post-bleaching [50]. The FRAP experiment reported here was carried out using the same experimental set-up.

The aim of the experiment is to investigate if after photobleaching EGFP-CD63 not within the observed bright spot, fluorescence in that area can recover at the expense of the fluoresence in the bright spot (figure 47, bottom left). The reverse experiment photobleaches CD63 within the bright spot and determines if it can recover by redistribution of the EGFP-CD63 in the WPB limiting membrane to the bright spot (figure 47, bottom right). The movement of CD63 between the two areas would indicate they are linked.

The bottom left panel of figure 47 shows that after photobleaching the half of the WPB without a EGFP-CD63 bright spot, even fluoresence across the WPB is restored but with no change to the bright spot at the tip, indicating EGFP-CD63

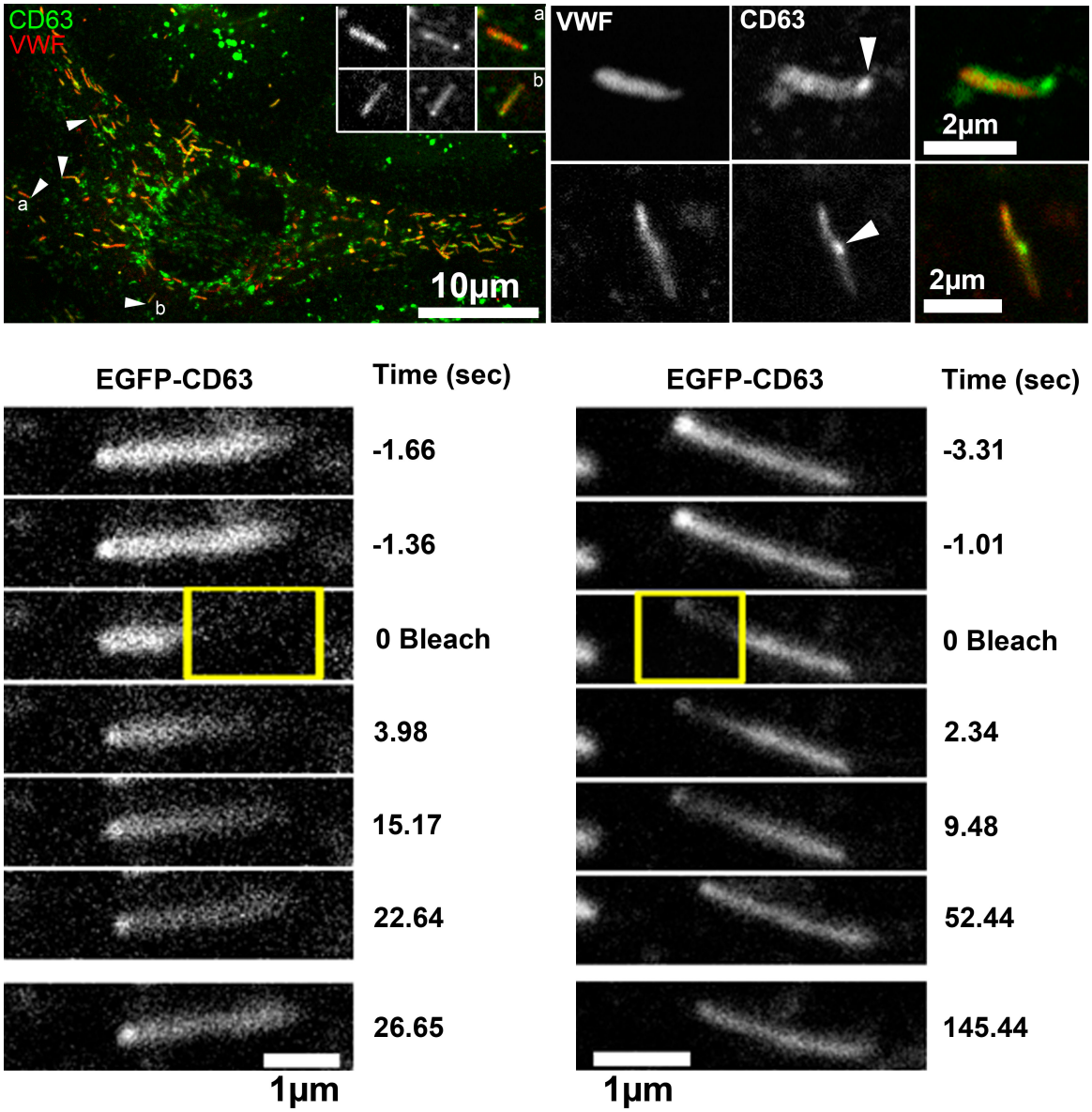

Figure 47: **Top left:** Immunofluoresence image of a single HUVEC, labelled for VWF and CD63. Multiple WPBs (arrowhead and inset) contain CD63 bright spots without a corresponding VWF bright spot. **Top right:** VWF and CD63 labelled individual WPBs, showing a CD63 bright spot at the tip and middle of the WPB respectively (arrowhead). **Bottom:** FRAP experiments showing recovery after bleaching of the non-bright spot region (left) and bright spot containing region (right). Experiment, imaging and analysis by Dr Ana Violeta Fonseca and Dr Tom Carter.

from within the bright spot cannot diffuse through the WPB limiting membrane for even fluorescence. The bottom right panel shows that after bleaching the half of the WPB containing the EGFP-CD63 bright spot, even fluorescence across the WPB can recover through diffusion of the unbleached EGFP-CD63, but the bright spot cannot recover. These two FRAP experiments indicate that there are two distinct pools of EGFP-CD63 in WPBs that contain a bright spot; the EGFP-CD63 within the bright spot and the EGFP-CD63 within the limiting membrane of the WPB.

The identification of CD63 as a component of the internal vesicle of WPBs further indicates the pedigree of WPBs as being lysosome related, given that CD63 is a marker for lysosome related organelles [19]. As WPBs are also regulated secretory organelles, the internal vesicle must also be secreted. The secreted vesicle would then become an exosome. This fits with the known characteristics of exosomes and WPBs, such as being secreted in response to raised intracellular Ca^{2+}levels [86, 26], being positively regulated by Rab27a and its effector Slp4-a [5, 75] and being enriched for CD63, like exosomes secreted from human B-lymphocytes [27].

There is a disparity in estimated prevalance between the CD63-bright spots and the membrane-limited internal vesicles observed by cryo-EM, with the fluorescence prevalance (using unstimulated HUVECs) at $<5\,\%$ and unstimulated HUVEC cryo-EM prevalance at $12.0\,\%$. However, fluorescence microscopy can penetrate the entire cell, encompassing the entire population of WPBs, whereas cryo-EM focuses only on the areas at the thinnest edge of the cell. An increased prevalance of internal vesicles in WPBs towards the cell periphery may indicate that receiving a vesicle is a maturation-dependent event.

5.4 Conclusion

Taken together, the CD63 bright spot observed by light microscopy and the ILVs observed by cryo-EM are likely to be the same object. The size and shape of the bright spot and its position within the WPB is consistant with the size, shape and

position of the WPB internal vesicles observed by cryo-EM. The topology of the objects observed by light and cryo-electron microscopy are also the same, with both indicating the presence of a lipid membrane within WPBs that is separate and distinct from the outer limiting membrane of the WPB.

This raises the question; what function could a CD63-containing internal vesicle have in WPBs? CD63 itself has no direct role in inflammation or haemostasis like other WPB components. Its role on the limiting membrane of WPBs is to stabilise P-selectin at the cell surface [22]. However post-WPB exocytosis, the WPB internal vesicles are thought to be released as exosomes, meaning the CD63 cargo would bypass the cell membrane. The exosomal function of CD63 is also not clear. Additionally, other experiments (Dr Ana Violeta Fonseca) have determined that P-selectin is not co-stored with CD63 on the internal vesicle of WPBs.

Aside from the membrane protein content, tomograms have captured some large and electron dense visible contents in the lumen of the WPB internal vesicle (figures 40 and 45). If the CD63-containing WPB internal vesicles are recycled from the cell membrane, as antibody uptake experiments (Dr Ana Violeta Fonseca) have shown, then they bud inwards from the limiting membrane of the endosome, creating an endosome ILV with the inside topologically equivalent to cytoplasm. It is not clear whether these large cytoplasmic objects are deliberately targeted to the WPB internal vesicle or simply not excluded during membrane invagination and vesicle formation. They appear superficially similar to ribosomes (figure 40) and the glycogen granules previously imaged in the proximity of WPBs ([109], figure 45). Given that neither of these components are expected to be released inside exosomes, this favours their non-exclusion rather than active recruitment to the internal vesicle. Ubiquitinated membrane proteins are targeted to endosome ILVs by ESCRT proteins, but the targetting and delivery mechanisms for cytosolic proteins and RNA released as exosomes is less clear, probably also requiring association with endosomal membrane proteins [86].

Release of exosomes via an intermediate secretory organelle such as the WPB, rather than release directly from endosomes is a novel route for exosome release from endothelial cells, and shows another feature WPBs have in common with other lysosome-related organelles.

6 Effects of pre-fixation on frozen-hydrated specimens

6.1 Introduction

Correlative light and electron microscopy (CLEM) images the same sample by both light microscopy and electron microscopy. The aim is to combine the labelling abilities of light microscopy (antibodies, fusion proteins and fluorescent compounds) with the resolution of the electron microscope. This solves a common problem in cellular EM of locating the object of interest and identifying it amongst other cellular components, without resorting to treatments such as plastic embedding and sectioning in order to allow antibody-conjugated gold particles to access to the cell. Such treatments can distort biological structures. Labelling is especially important for smaller objects without a signature structural element like the VWF tubules of WPBs. Another way to label proteins within the cell for EM is the expression of an electron-dense protein label, such as the iron-containing protein ferritin [127]. Ferritin could then be expressed as fusion protein to label other proteins of interest, in a similar way to GFP fusion proteins in light microscopy.

One of the barriers to CLEM of frozen-hydrated specimens is immobilising the sample prior to light microscopy. Immobilising the sample is necessary to ensure that the objects of interest do not move during imaging or whilst the specimen is transferred between one microscope and another, especially when trying to accurately localise the objects within the cell. Often, immobilisation is achieved through plunge-freezing the sample, for the subsequent cryo-EM experiment and using an adapted light microscope capable of imaging at low temperatures to collect the light microscopy images [12, 93, 97, 112].

Another CLEM approach, called ILEM (integrated light and electron microscope) places the objective lens of a fluoresence microscope within the column of an electron microscope, perpendicular to the electron beam path [1]. The sample is supported

by the same holder, which can be rotated between beam paths. This simplifies the workflow as the sample need only be mounted in one microscope, reducing the risk of introducing handling errors with the delicate specimens and can reduce the processing steps needed to correlate the images as the sample is maintained in the same orientation within the holder. The second generation ILEM2 permits the imaging of frozen-hydrated specimens [29], however in order to fit the light microscopy components within the column of the EM, the cryo blades used to protect the sample from degradation must be removed, limiting the potential imaging time.

A third system seeks the benefit of having the sample held by the same holder, but without the integration into the EM, by using the FEI 'Autogrid' system to hold the sample in both microscopes, therefore transferring whole cartridges between instruments [9].

In this chapter, a method combining the sample preparation and fixation steps commonly used in immunofluorescence microscopy with plunge-freezing is developed. The end result of this sample preparation method is a fixed and frozen-hydrated specimen, where the sample has been kept hydrated throughout. When the grid is fixed and hydrated, it can be imaged by light microscopy prior to plunge-freezing. The aim for developing this technique was to further investigate the CD63-enriched internal vesicles of WPBs (chapter 5), by correlating the CD63-enriched bright spots observed by light microscopy with the membrane enclosed vesicles observed by cryo-EM.

6.2 Development of a method for cryo-electron microscopy of fixed and frozen-hydrated cells

Fixed and permeabilised experiments (2 runs; 15 EM grids total) exactly followed the protocol for immunofluorescence preparation (section 2.4 and section 2.7), with fixation by 3 % PFA and permeabilisation by 50 mM NH_4Cl and 0.2 % saponin in PBS, combined with the plunge-freezing parameters used for live-cell experiments. Images

collected from these grids show the cellular material to be granular and homogenous. There are some structural features, but the information and preservation is limited, only a few cytoskeletal elements seem to be present. At first, this granularity was attributed to collapse due to dehydration, as outside the cells there appeared to be very little ice within the holes of the carbon film, suggesting that the grid had been over blotted and was too dry. Blotting time was systematically reduced over 2 runs, 16 grids from 20 seconds to 1 second, to ensure cells were sufficiently hydrated prior to freezing. The granularity did not improve, but ice was visible in the holes not covered by cells, a sign that the grid is hydrated with a thin film of ice over the whole grid. The observed granular texture in a 2 second blotting time grid is shown in figure 48. This texture obscures all of the detail in the images, rendering them hard to interpret beyond identification of some large cellular componenets such as mitochondria.

A second attempt to find the cause of the granular texture eliminated the permeabilisation step and used both PFA and an alternative fixation agent; glutaraldehyde. 1 run of experiments with 6 EM grids in each condition were prepared. This gave a marked improvement upon previous results, with grids from both the glutaraldehyde and PFA conditions giving similar results in the absence of permeabilisation. The PFA fixation is consistant with the light microscopy protocol and bypasses known autofluoresence problems with glutaraldehyde [55] so PFA was used for further experiments. A typical field of view for PFA without permeabilisation is shown in figure 49. The granular background is significantly reduced, and vesicles and other membrane-enclosed structures remain. There is still some granular background, so omitting the permeabilisation step merely reduces the granularity rather than eliminating it. This is consistant with PFA having a slight permeabilising effect on cells, rendering them "leaky" to dyes that were previously unable to cross the membrane in live cells [78]. Therefore, even without a specific permeabilising step, the cell membrane is perforated with a resulting loss of structure. This protocol has since been sucessfully used in another 25 grids over 3 different runs with nucleofected cells for CLEM.

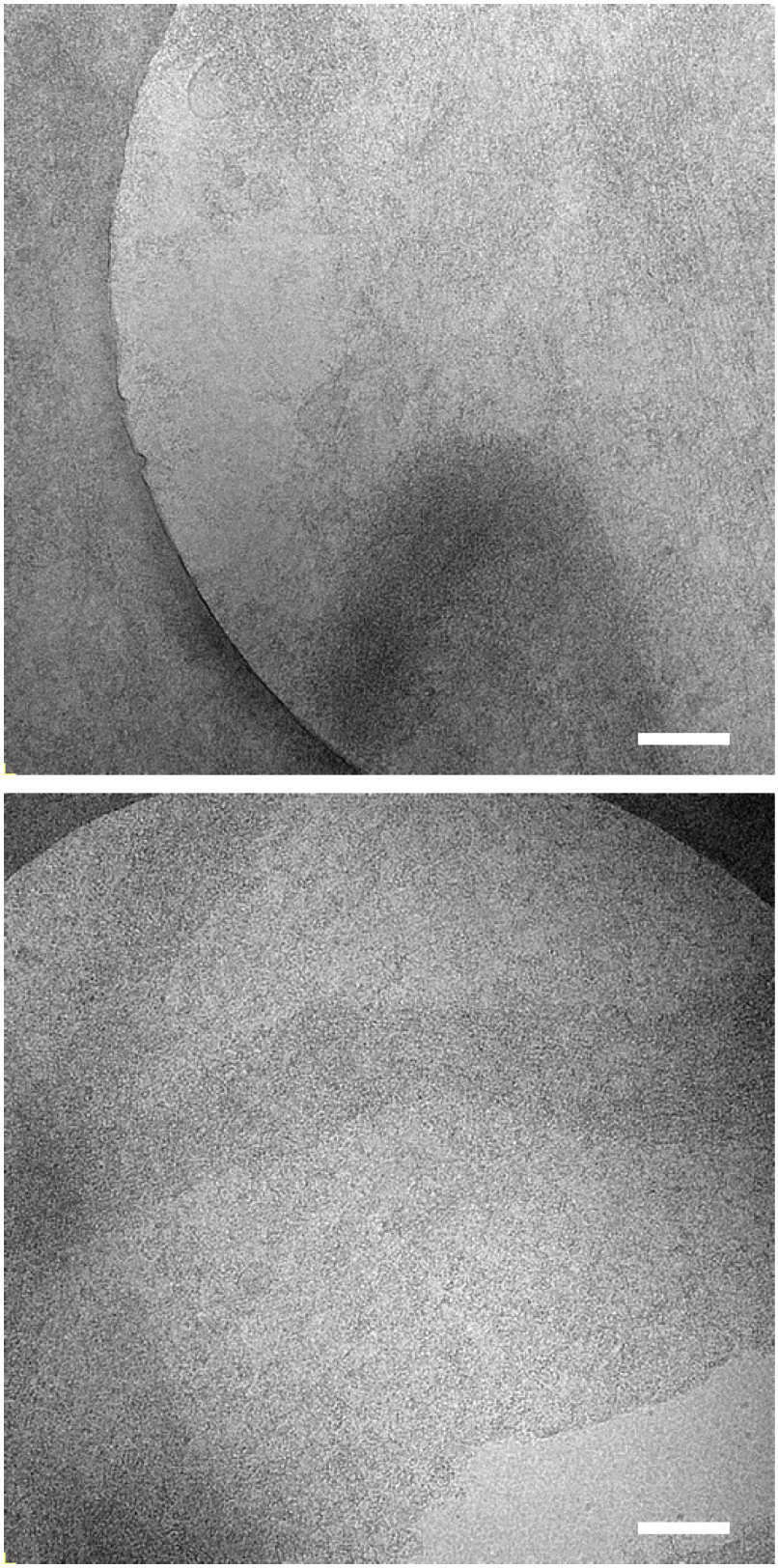

Figure 48: Typical electron micrographs of fixed and permeabilised HUVEC. Images have a very granular background where cellular material is present, and much of the detail is obscured. Scale bar: 200 nm.

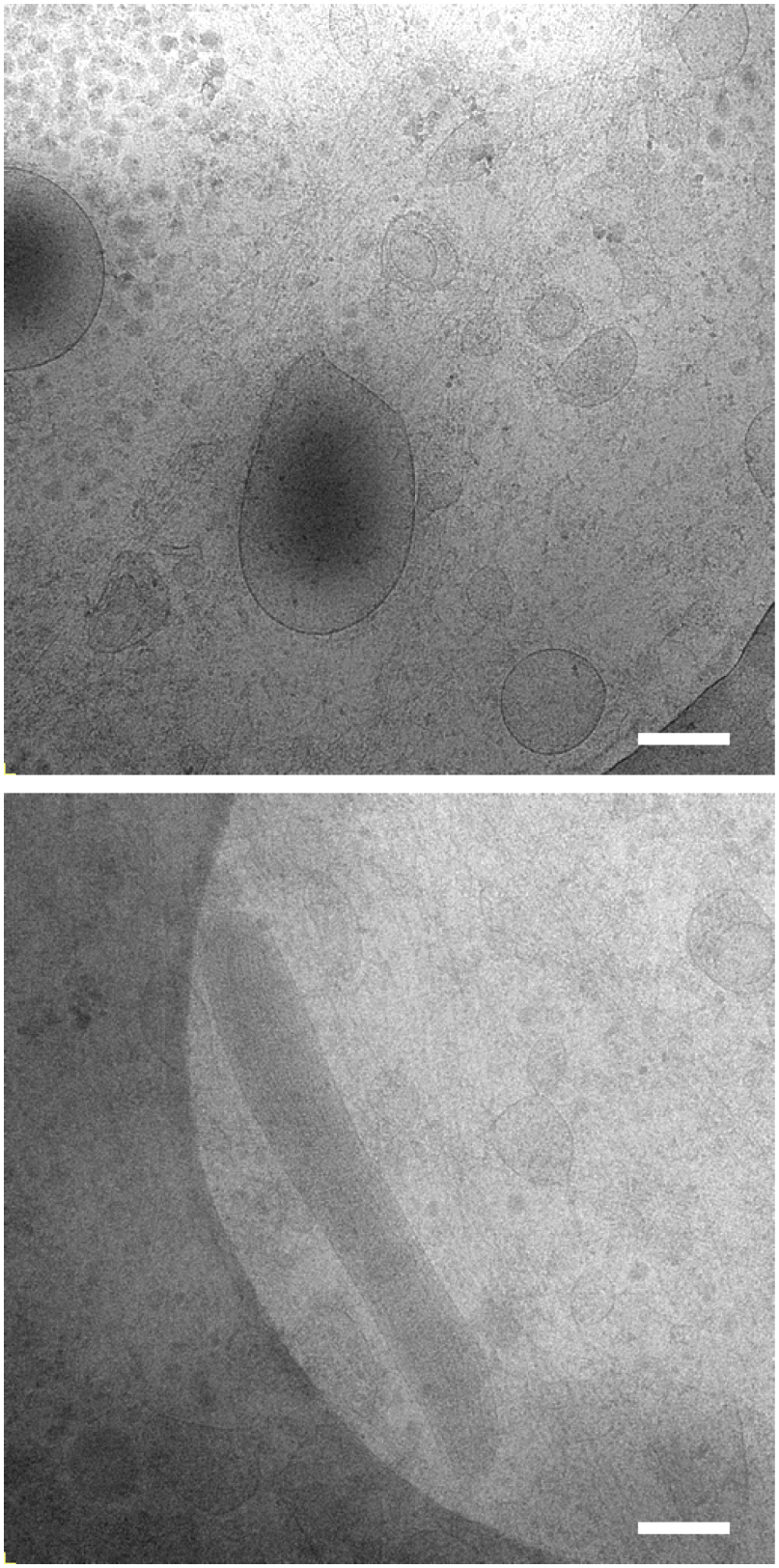

Figure 49: Typical electron micrograph of PFA fixed HUVEC without permeabilisation. The granular background is significantly reduced from permeabilised samples. The top image shows vesicles and other cytoplasmic structures, and the bottom shows a WPB with cytoskeletal elements. Scale bar: 200 nm.

6.3 Structure preservation in pre-fixed, frozen-hydrated cells

In order to determine the degree of preservation conferred by pre-fixing before plunge-freezing and plunge-freezing alone, images of WPBs from each preparation method were compared. Specifically, the helical order of the VWF tubules within WPBs in each condition were compared using their Fourier transforms. The helix formed by VWF has been previously characterised within WPBs [4], with a strong repeat for the third layer line at 120 Å forming the main signal of a "unique molecular signature of VWF tubules". Structures of tubules consisting of truncated VWF containing only the purified D1D2D'D3 domains by negative stain EM give repeats of between 96 Å and 120 Å [47].

This third layer line is also prominent in both new frozen-hydrated images and pre-fixed images (figure 50), with both at 115 Å. Considering the different magnifications and defocus values between these images and from the published data and some flexibility and variability in the helices, this probably indicates that the VWF helices are identically preserved in both methods. This suggests that the pre-fixed, frozen-hydrated method can preserve structure at least to a resolution of ~120 Å, when compared to plunge-freezing alone. Preservation on this scale makes pre-fixed and frozen-hydrated a possible method for cellular biology investigations, such as for WPBs.

As well as preserving the molecular architecture of VWF tubules to a quantifiable resolution of at least ~120 Å, the presence of other cellular components suggests that not only densely packed protein is preserved by this process. In particular, continuous and fluidly-curved lipid membranes and vesicles are present and preserved, in contrast to WPB images from high-pressure freezing and sectioning or other fixation and staining techniques which can give the appearance of lumpy or disjointed plasma membranes [134, 109]. Avoiding the need for resin embedding or sectioning of the fixed cells contributes to a reduction in sample preparation artefacts when compared to those techniques, comparing favourably with solely frozen-hydrated cells. The ar-

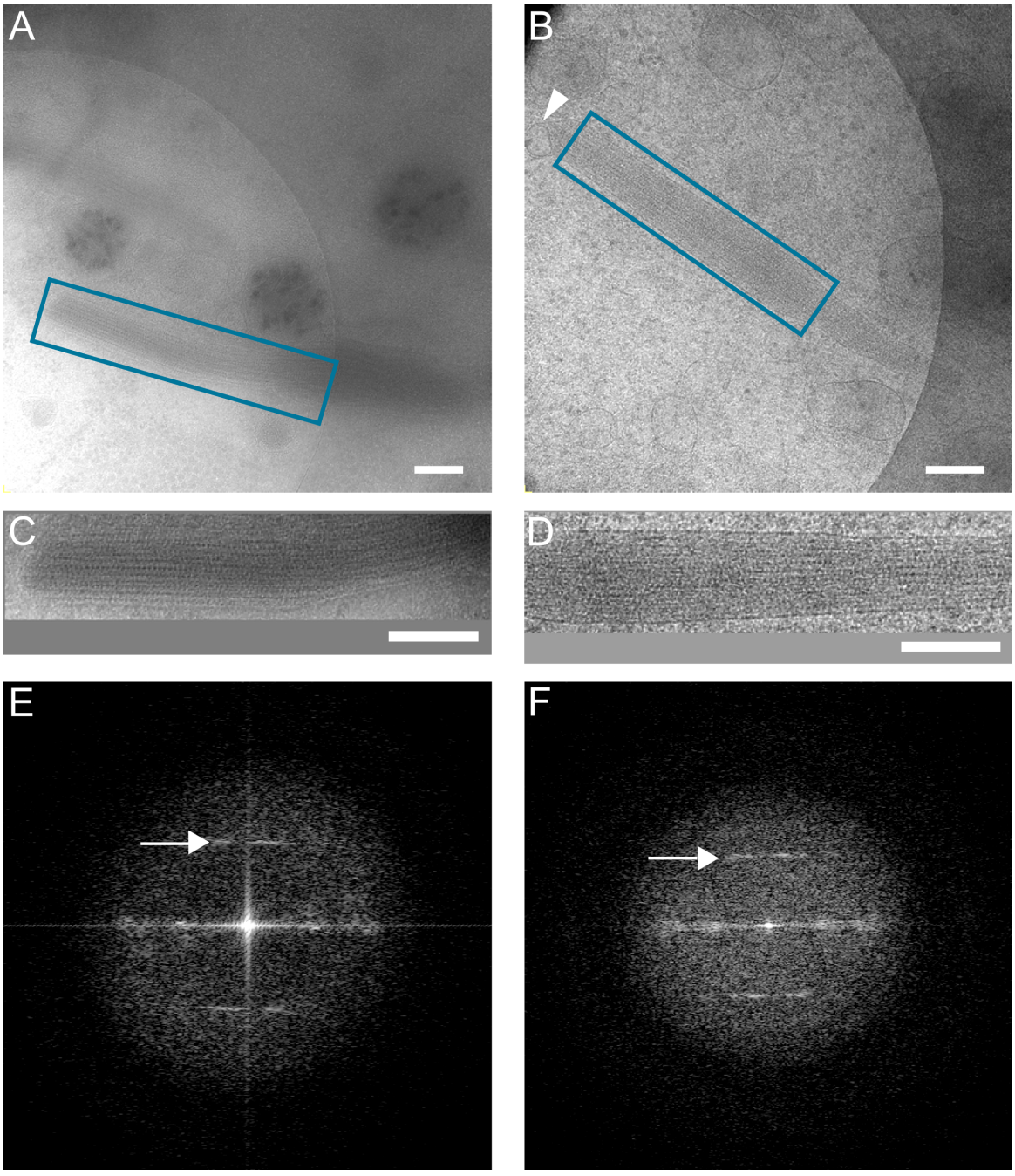

Figure 50: Comparision of frozen-hydrated and pre-fixed WPB images. **A**: Electron micrograph of WPB within frozen-hydrated HUVEC, magnification 21,000x. **B**: Electron micrograph of WPB within pre-fixed, frozen-hydrated HUVEC, magnification 26,000x. The arrowhead shows an internal vesicle preserved within the WPB. **C**: Zoom of boxed region in A. **D**: Zoom of boxed region in B. **E**: FFT of boxed region in A, with third layer line indicated at 115 Å. **F**: FFT of boxed region in B, with third layer line indicated at 115 Å. All scale bars: 200 nm

rowhead in figure 50b indicates the presence of an internal vesicle. It was important to verify that in addition to preserving the VWF helical structure, the internal vesicle was preserved, to ensure that pre-fixation would permit correlative imaging of the internal vesicle.

Comparing figure 50a to figure 50b does show the pre-fixed image to have some 'cloudiness' and less contrast than the solely frozen-hydrated image. As noted above, this is likely to be a consequence of the permeabilising effect of fixation on the cells, disrupting some structures and giving rise to an increased background.

6.4 Correlative light and cryo-electron microscopy on fixed-hydrated cells

6.4.1 Light microscopy

The ability to fix cells and immobilise their components, whilst still later imaging them in a frozen-hydrated state immediately suggests the possibility of using a CLEM approach. Even without permeabilisation making it possible to introduce antibodies into the cells, it still leaves cell permeable compounds such as DAPI, genetic fusion proteins such as GFP labelling or antibodies that can be internalised through plasma membrane receptors as possible fluorescent markers.

2 initial runs of experiments (5 grids each) into CLEM with pre-fixed cells used DAPI to label the nucleus combined with CD63-GFP (section 2.10) to label WPBs (and endosomes) within HUVECs, with the goal of labelling and imaging the CD63-enriched bright spots observed previously and thought to correlate to internal vesicles within WPBs. These experiments were used to develop the image acquisition strategy. A consideration for light microscopy with EM grids is the autofluorescence of both carbon film and gold grid bars. Observations from these experiments suggested the carbon film and gold grid bars were autofluorescent using the TRITC filter set (excitation: 555 nm and emission: 605 nm) and FITC filter set (excitation: 490 nm

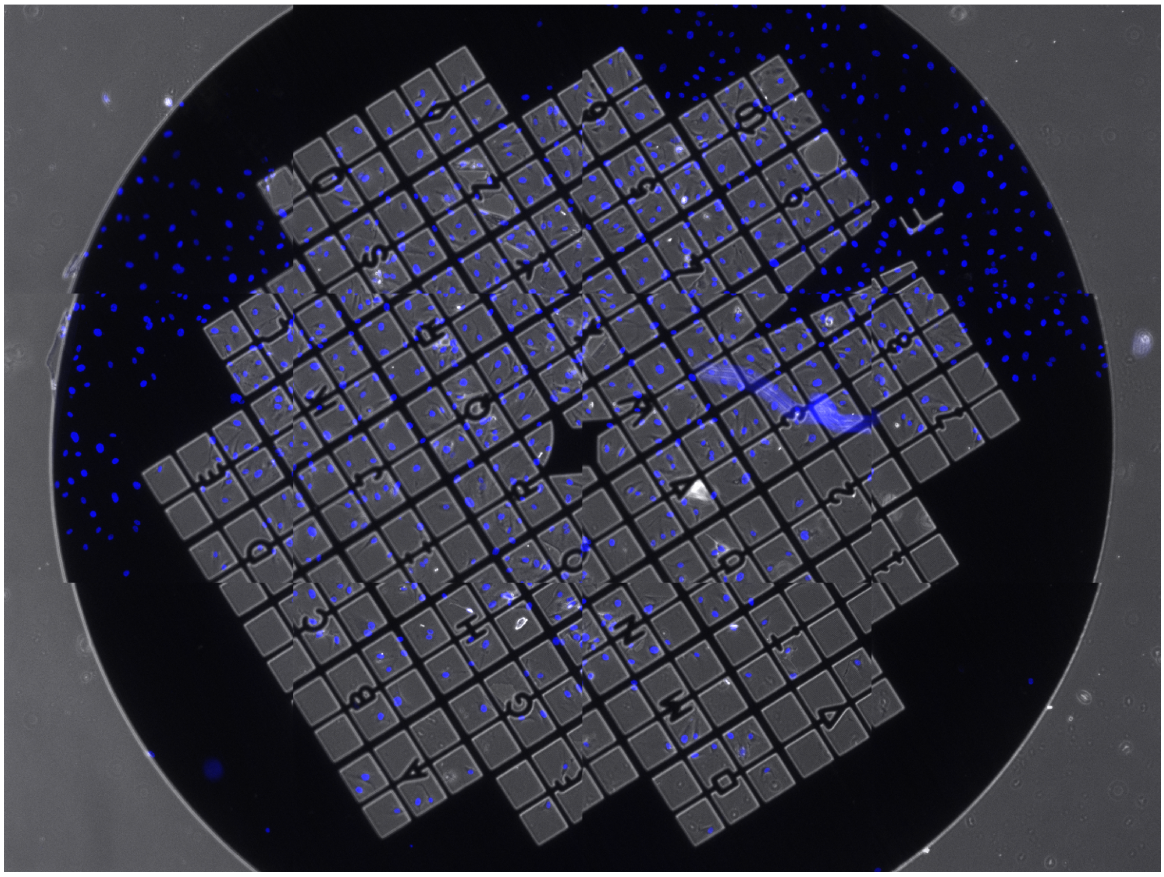

Figure 51: Light microscopy montage of whole EM grid containing fixed HUVECs. DAPI (blue) fluorescence is overlaid on phase constrast images, to show the cell distribution and extent, and the EM grid orientation. Montage of 12 images per channel.

and emission: 528 nm) and lower in the CFP filter set (excitation: 436 nm and emission: 470 nm). Slight autofluorescence can be useful in indicating the position of the grid bars and the holes within the carbon film, but it seems preferable to eliminate the background to increase the signal to noise ratio for the channel containing the experimental data, and use transmitted light/phase contrast to show the carbon film, cell periphery and grid bars. A subsequent run of 12 grids used CD63-CFP to take advantage of the lower background, however both CFP constructs were considerably dimmer than the GFP versions, which when compensated for with longer exposure times gave no additional benefit over GFP.

The first imaging step is to capture a low magnification (10x) light microscopy overview of the whole EM grid (~3 mm in diameter) (figure 51). At this magnification,

an overview of the grid comprises 12 512×512 pixel images per channel, so can be collected rapidly. The overview is useful for determining the orientation of the EM grid, the distribution of cells in each grid square and locations suitable for further imaging with increased magnification. As shown in figure 51, the letters, numbers and symbols on the "Finder" grid are easily visible for identifying each grid square. Only DAPI and phase contrast images are collected for the overview as the WPBs are not visible at this magnification.

Promising areas are then re-imaged using a 100x objective lens, this time with phase contrast, DAPI and GFP or CFP channels collected. A set of example images are shown in figure 52a and b, showing two cells, one containing multiple perinuclear, CD63-positive structures and CD63-positive structures towards the cell periphery. With this set-up (section 2.10.2), a single image corresponds to approximately one Finder grid square.

In these experiments, the initial aim was to collect a complete set of light microscopy data over the whole ~3 mm grid at 100x magnification, the magnification needed to image the WPBs by light microscopy and correlate with the electron microscopy. This turned out to be quite difficult using the software built in to the Deltavision light microscopy system, as the stage height needed to keep the grid in focus varied across its 3 mm diameter. The in-built autofocus was prone to "runaway focusing" in areas with low contrast, where the correct focus couldn't be detected so was moved to the extreme of its range. Multiple z-heights for each channel and position, without autofocus were also considered but led to an unacceptably large imaging time.

To reduce this time, in the current protocol, the whole grid was only covered by 10x magnification, meaning the whole grid can be collected in 12 images per channel (figure 51), and only selected areas imaged at 100x. These areas were determined and subsequently imaged manually. However, manual checking and imaging of each area is also very time-intensive, by definition requires human presence and still misses some

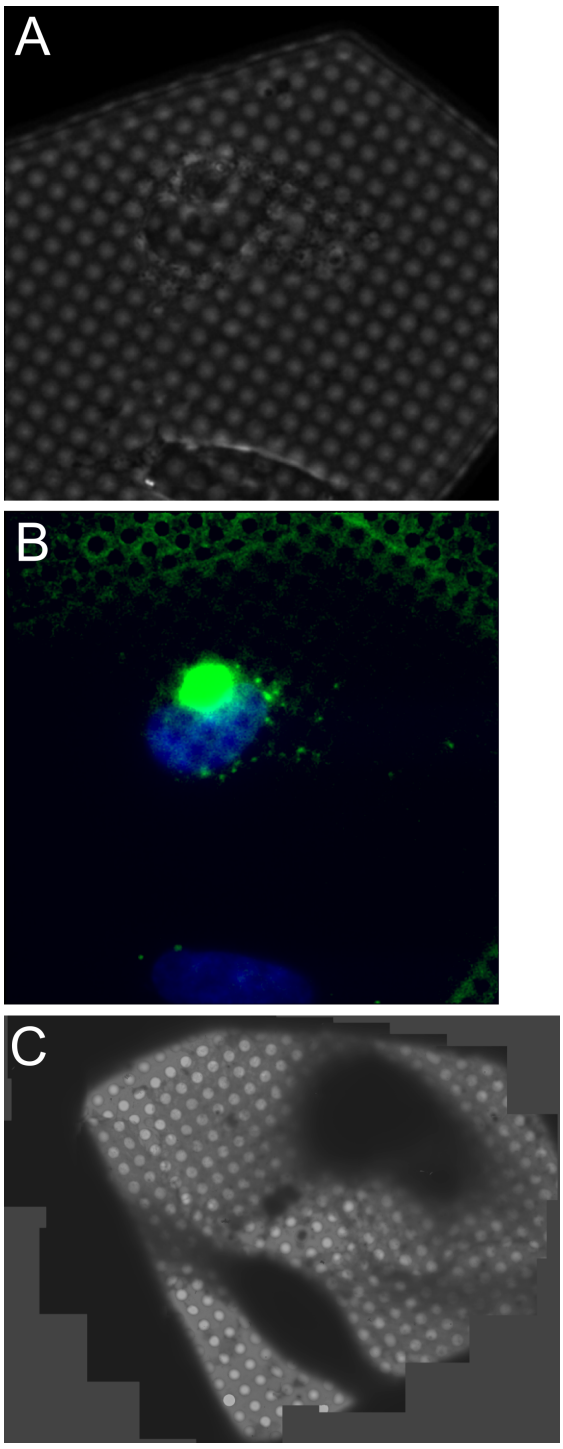

Figure 52: Light and electron microscopy images of the same area before correlation but after approximate comparable scaling. **A**: Single phase contrast image showing two cells within a grid square. **B**: Overlay of two fluorescent images of the same area. DAPI is coloured blue and CD63-CFP labelled in green. **C**: Stitched montage of 48 electron microscopy images of the same grid square as A and B.

areas which could be potentially useful when comparing with the electron microscopy images.

A different sample preparation approach, mounting the grids onto slides but with a spacer between slide and coverslip containing a few microlitres of buffer to allow the grid to remain hydrated, may help with data collection by allowing a wider range of light microscopes to be used. Specifically, the use of a slide scanning microscope. These instruments are purpose-built to image large areas automatically at multiple magnifications, so may have more success with the changes in height across an EM grid.

6.4.2 Electron microscopy

The first step in the electron microscopy imaging is also to take a low magnification overview of the whole EM grid. The EM montage used ~100, 190x magnification, 1024×1024 pixel images to cover the whole grid, following the procedure used in frozen-hydrated imaging (figure 53). Using the symbols on the Finder grid, the same areas that were imaged at 100x by light microscopy were relocated in the electron microscope montage.

Areas with promising light microscopy images were then re-montaged with an increased magnification, suitable for locating individual WPBs and other cellular features. The size of each montage varied depending on how much of the grid square was desired, using a magnification of 2700x and collecting unbinned 2048×2048 pixel images. A montage from 48 images is shown in figure 52c, where it has been stitched into a single image. Light microscopy images from the same grid square are shown in panels a and b.

Finally, images and tomograms at the record magnification, 26000x, 8.17 Å/px, were collected, using the same low dose procedures as for frozen-hydrated grids.

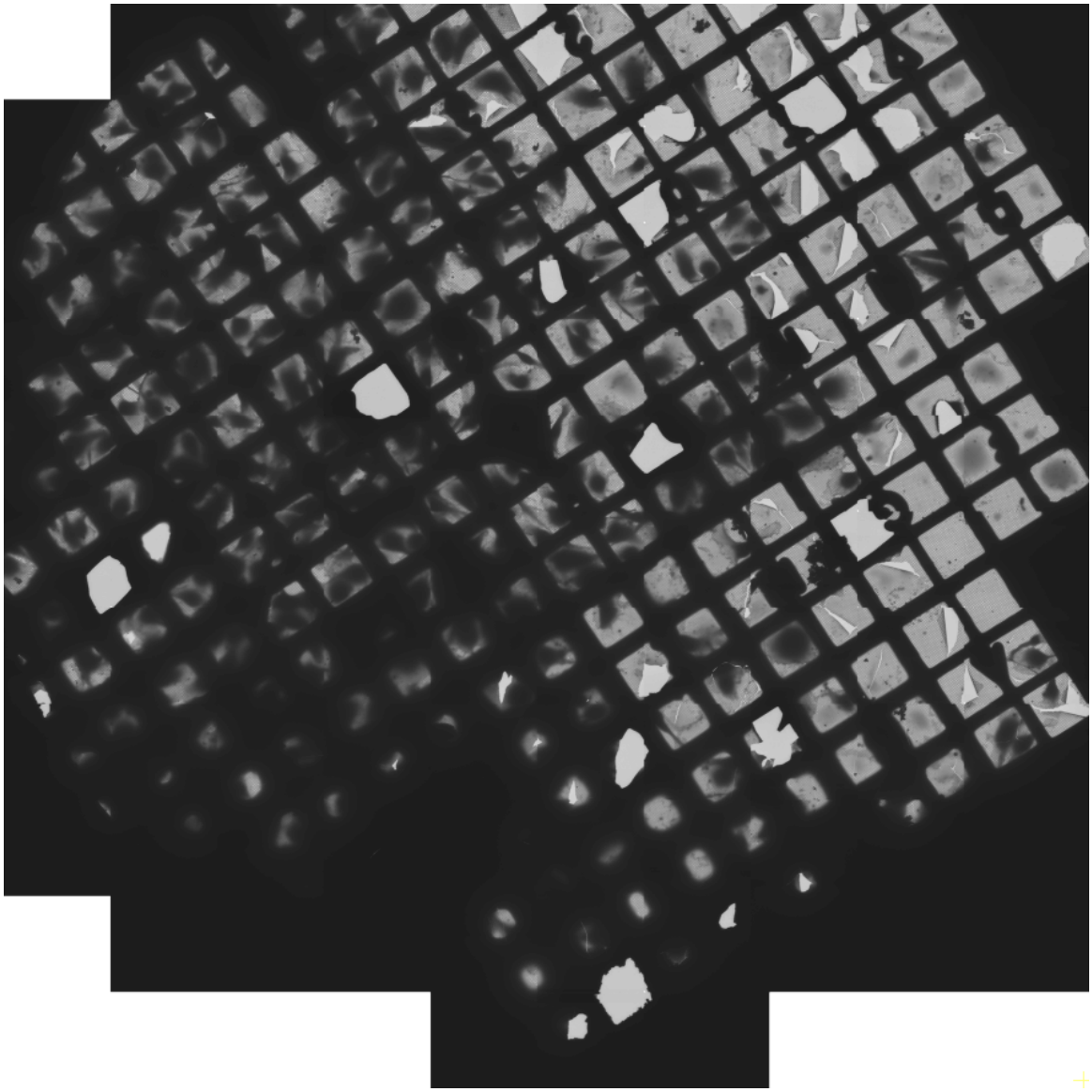

Figure 53: Electron microscopy montage of whole EM grid containing fixed HUVECs. The letters and numbers of the Finder grid can be seen, particularly on the right hand side.

6.4.3 Correlation and interpretation

The first step in correlating between the light and electron images is to compare the lowest magnification montages from both imaging methods that show the entire EM grid. This 'side-by-side' comparison is used to re-locate the areas already imaged by light microscopy in the electron microscope, and so it needs only be accurate enough to identify one grid square from another. Coarsely correlating on this level makes the fine alignment using higher magnification images easier by restricting the alignment to a single grid square. Using the symbols on the Finder grid also allows any mirroring between the light and electron images to be corrected. This is shown in figure 52, where the coarse correlation has already determined that these images relate to the same grid square.

To calculate a fine correlation, a mixture of computational and manual methods were used to determine the parameters needed for alignment. Scale and rotation were determined first. Calculating the scale and rotation parameters utilised the regular, repeating background of the holey carbon film. This repeating pattern is clearly shown in the FFT of both the phase and electron images in figure 54. The relative angle between the patterns and the distance between peaks were measured at 3 different points in the FFT and the average values used to transform the real-space electron microscopy montage to the same scale and angle as the fluorescence and phase contrast light microscopy images. As the holey carbon pattern has 4-fold rotational symmetry, using the relative angles from the FFTs requires that the images are already rotated to $\pm 45^{\circ}$ of each other, so as not to align them in the wrong direction. In the case of the images in figure 52, this true for the unprocessed images, but it is also possible to roughly align them manually to within $\pm 45^{\circ}$ using the distribution of cells.

After scale and rotation were corrected, the light microscopy and cryo-EM images were overlaid manually, using the distribution of cells, grid bars and the holey carbon film as a guide. 3 regions of a single grid have been correlated using this process, of which 2 are shown in figure 55.

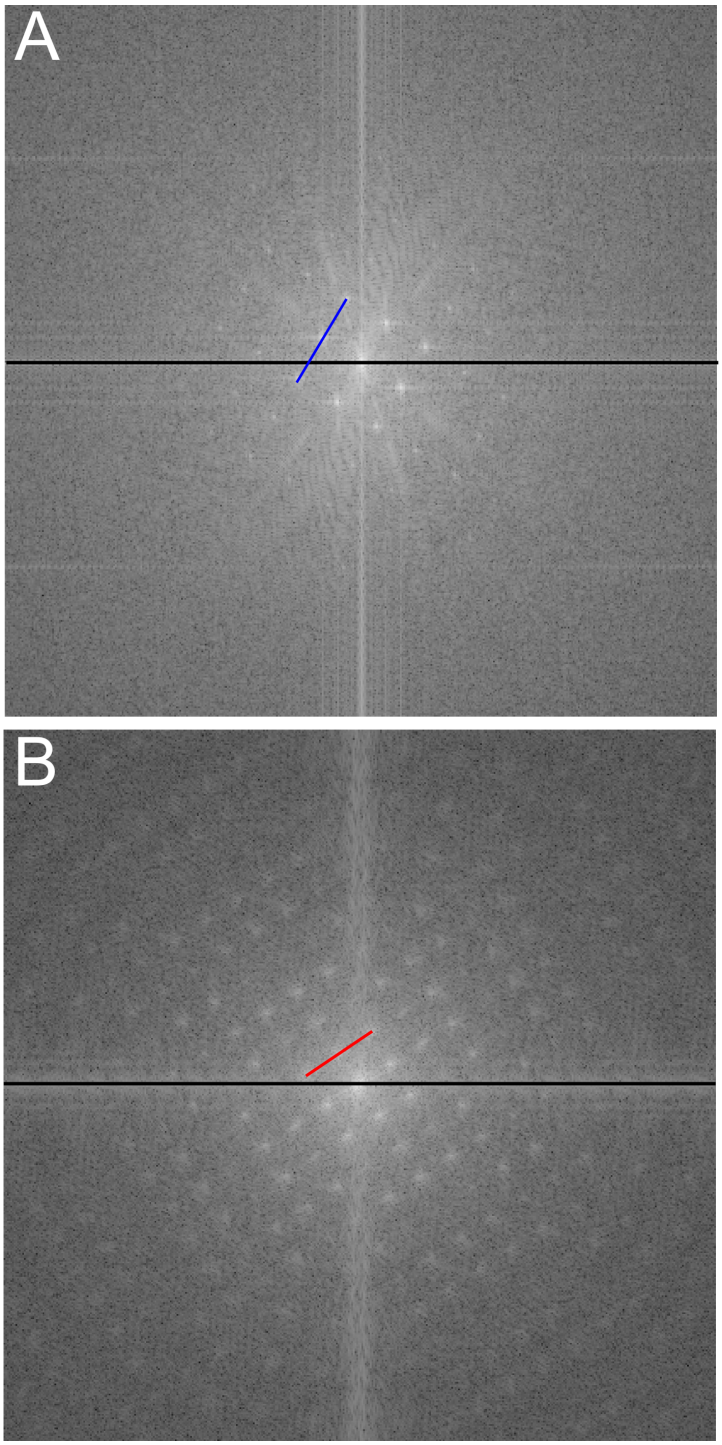

Figure 54: A**:** FFT of the the phase contrast image and **B**: EM montage images for correlation. The EM montage was cropped to 512×512 px to match the phase contrast image before transforming in order to give a comparable transform. The blue and red lines show the length measurement between 3 consecutive peaks and the angle between the blue/red and black central line gives the relative roation between the lattices.

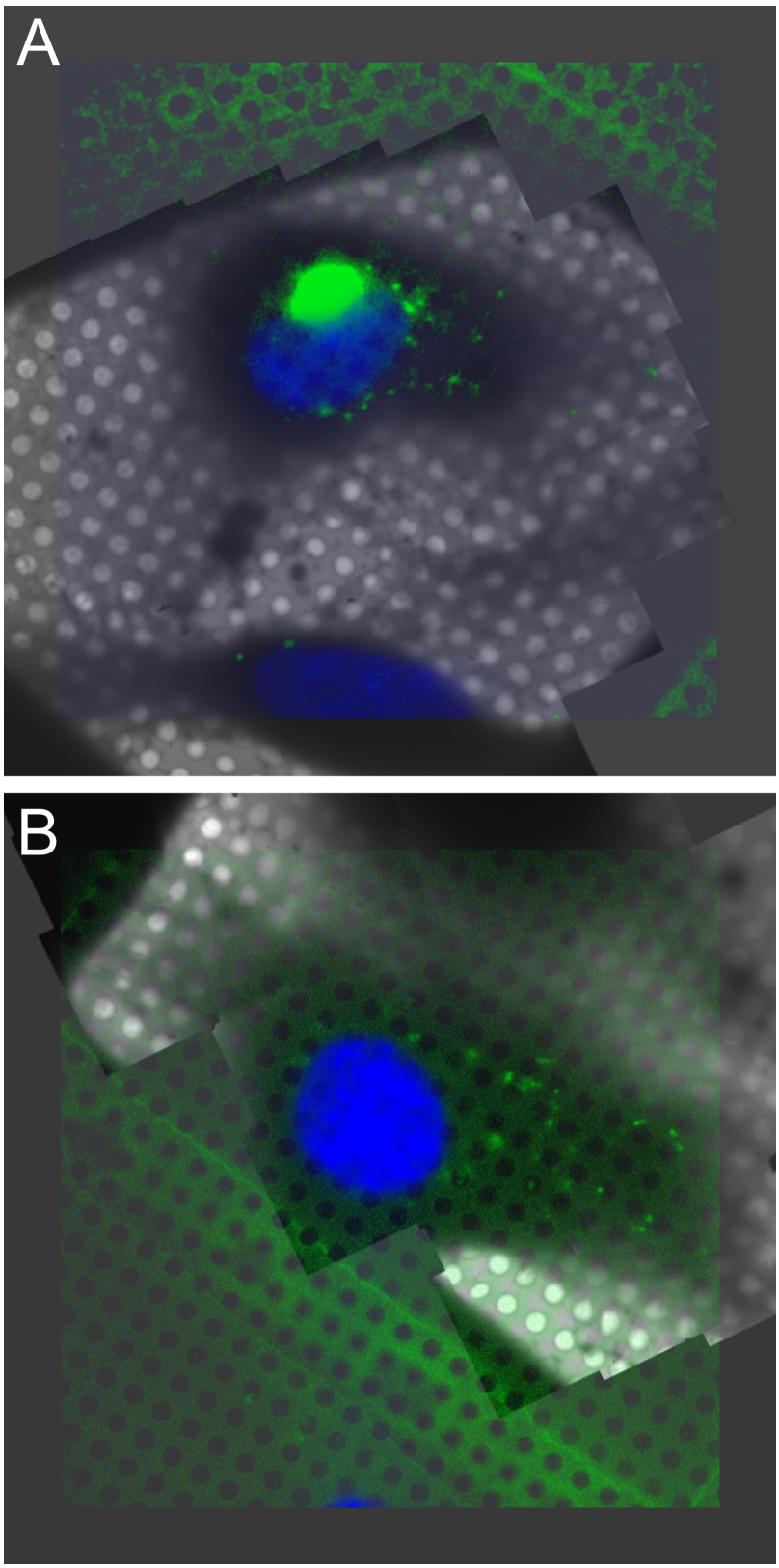

Figure 55: Correlative light-electron microscopy overlays, showing DAPI (blue) and CD63-CFP (green) fluorescence over cryo-electron microscopy montages. **A** shows the data from figure 52.

The correlation between the two sets of images is good enough to identify a single hole in the carbon film in both images. The primary reason for imperfect alignment comes from assembly of the EM montage and is visible in figure 54b, where the peaks are broader in comparison to the sharp points from the single light microscopy image. Broad peaks indicate that the carbon holes are irregularly spaced in the image; an artefact generated from the montage collection and assembly. Irregularly spaced holes mean the lattice is changing across the image, meaning the image is skewed or warped; a transformation that is much harder to correct for.

A more quantitative method for calculating the translation might be possible by harnessing stage co-ordinates from the respective microscopes. Using a cross-correlation step to solve the translation after correcting the scale and rotation, and iterating these steps would also improve the alignment. Automated software to handle bringing images from both modes into registration is not readily availible, with published approachs using in-house software or MATLAB scripts [57, 95].

6.5 Cryo-electron tomography of pre-fixed, frozen-hydrated HUVECs

5 tilt series of pre-fixed, frozen-hydrated HUVECs have been collected, with a maximum dose of 70 $e^-/Å^2$. From these tilt series, 2 were fully processed into tomograms as previously. The other 3 tilt-series contained no fiducial markers, so were aligned only with cross-correlation, leading to poor tomograms. The aligned tilt series and tomograms show no evidence of radiation damage, such as 'bubbling', at this dose which is comparable to the dose that solely frozen-hydrated specimens were imaged at. Cross-sections of the tomograms also show no signs of flattening or collapse. Collapse should not be expected for any frozen-hydrated specimens, as the vitrified buffer supports the fixed cellular material and protects it in the vacuum of the microscope, and the fixation does not affect this.

6.6 Conclusion

Presented in this chapter is a method for fixing cells prior to plunge-freezing for cryo-EM. A primary use for this technique would be for correlative light and electron microscopy, where the sample is imaged by light microscopy prior to cryo-EM. Initial experiments developing this technique are also shown.

Paraformaldehyde fixation does not interfere with the plunge-freezing process and comparison of pre-fixed, frozen-hydrated specimens with those prepared by plunge-freezing alone shows similar preservation to the third layer line of VWF tubules at ~120 Å. Preservation to this resolution makes the technique useful for investigating organelles and large assemblies such as WPBs and the VWF tubules shown.

Before freezing, it is possible to image the fixed-hydrated grid using an glass-bottom dish filled with PBS and an inverted light microscope. This avoids the need for specialised equipment to conduct cryo-light microscopy whilst still keeping the sample hydrated for plunge-freezing prior to imaging by cryo-EM. In this way, a new route to conducting CLEM experiments with standard equipment has been developed. By conducting the light imaging with the specimen hydrated and at room temperature, the sample is much less fragile than when frozen, as it is not susceptible to frost contamination or temperature variations causing formation of crystalline ice.

A method for correlating individual areas using the intrinsic properties of the holey carbon Quantifoil film to calculate the scale and rotation factors between the images has been shown.

In summary, fixed, whole, frozen-hydrated cells are preserved well-enough to permit investigation of WPBs by light and cryo-electron microscopy, using the techniques outlined in this chapter. Further refinements to sample preparation, light microscopy and image processing may improve the technique.

7 Conclusion

The first results chapter (chapter 3) of this thesis showed the development of a reproducible protocol for the preparation of whole-mount frozen-hydrated HUVECs for cryo-EM and imaging them at their thin edge. Using live-cell microscopy, a protocol for stimulating WPB release from HUVECs grown on EM grids that could be translated to sample preparation for electron microscopy was also developed, showing that the release time of ionomycin-evoked WPB exocytosis under conditions prior to plunge-freezing is ~20 seconds, and accessible for cryo-EM sample preparation. The repeat of this protocol for 124 grids over 10 experiments has validated the sample preparation approach, with adapted versions of the preparation protocol used for other cell types and conditions on a further 11 experiments totalling 120 grids.

Chapter 4 used the library of WPB images and tomograms collected to make a comprehensive analysis of the WPB size and shape across different stimulation conditions and cell types. The relationship between WPB shape, presence of VWF tubules and alignment of VWF tubules was examined, using round WPBs from stimulated cells, HHMECs and HUVECs subjected to hypotonic shock. The presence of VWF tubules in WPBs of all shapes was unexpected, as the elongated nature of WPBs is driven by VWF tubules [68]. However, images from HHMECs show that VWF tubules can also be present without elongating the WPB. The tubules in these WPBs are shorter and do not run parallel but in all directions. The effect of disordered tubules on orderly unfurling of VWF tubules into strings during WPB exocytosis is not clear. The difference in WPB shape between different, endogenously VWF expressing cell types suggests that VWF is not solely responsible for the elongated shape of WPBs.

Models of VWF helices within ordered and disordered WPBs show the relationship between organelle shape and cargo organisation, and the relationship between intertubule space and disorder suggests how tubule dissassembly during fusion may function. The preparation of disordered WPBs with unaligned VWF tubules increased

the distance between tubules and gave the opportunity to examine the portion of VWF that does not make up the tubule for the first time in WPBs: the "C-terminal bouquet" [137]. A trailing "arm-like" density protruding from the tubules has been imaged in disordered, non-rod-shaped WPBs. The packing of these arms in rod-shaped WPBs with a smaller intertubule distance remains unclear.

Subtomograms of individual VWF helices were extracted and used to calculate a helical reconstruction for VWF. The reconstruction shows the tubular portion of VWF but cannot resolve the C-terminal bouquets as radial arms. It is not known if the arms are sufficiently helically ordered to permit a reconstruction. So far only flexible structures have been imaged.

In chapter 5, a vesicle within WPBs was identified by cryo-EM and cryo-ET in all cell types imaged. Subsequent fluorescence microscopy investigation by Dr Ana Violeta Fonseca localised the membrane tetraspanin CD63, a known WPB component and endosomal marker, to this vesicle.

The presence of a vesicle within secretory granules, such as WPBs, means that the vesicle is released upon exocytosis, like the VWF content. This release is similar to the exocytosis of the lumenal vesicles of late endosomes/multi-vesicular bodies, which are known as exosomes. The internal vesicles of WPBs are presumably also released as exosomes. The role of CD63-enriched exosome release simultaneously with the haemostatic and proinflammatory proteins of WPBs in not year clear. Identification of additional components in the vesicle, particularly soluble proteins may clarify this. Release of exosomes from WPBs is a novel route for exosome release, although in keeping with the properties of other lysosome related organelles, especially platelet α-granules which contain both internal vesicles and VWF tubules. Further work is needed to identify other components of this internal vesicle and the mechanism of delivery of the vesicle to the WPB.

In the final results chapter (chapter 6), a pre-fixed and frozen-hydrated sample preparation method for cryo-EM and cryo-ET was developed. Fixation prior

to plunge-freezing means the sample is immobilised but still hydrated and at room temperature. This gives a prime window for a fluorescence microscopy investigation prior to freezing and imaging by electron microscopy.

Initial experiments into correlative microscopy targetted correlation of the CD63-enriched vesicle discovered in chapter 5. These experiments showed that the pre-fixed and frozen-hydrated sample preparation protocol sucessfully preserved both the helical structure of VWF tubules and the internal vesicle, compared with frozen-hydrated HUVECs alone. A protocol for fluorescence image acquisition and alignment between the light and electron micrographs was devised and correlation between the images achieved on a grid-square level. Correlation on a sub-organelle level will require further work.

I have extended previous observations on Weibel-Palade bodies through a larger dataset of 3D granule volumes. These have revealed novel features of VWF structure, and granule membrane structure with emphasis on organelle biogenesis as well as exocytosis. In addition, we developed procedures preparing frozen-hydrated and fixed-frozen-hydrated specimens which may be used to further study the major findings of this thesis.

References

[1] AV Agronskaia, JA Valentijn, LF van Driel, CTWM Schneijdenberg, BM Humbel, PMP van Bergen en Henegouwen, AM Verkleij, AJ Koster, and HC Gerritsen. Integrated fluorescence and transmission electron microscopy. *Journal of Structural Biology*, 164:183–189, 2008.

[2] V Babich, A Meli, L Knipe, J Dempster, P Skehel, MJ Hannah, and T Carter. Selective release of molecules from Weibel-Palade bodies during a lingering kiss. *Blood*, 111(11):5282–5290, 2008.

[3] W Baumeister, R Grimm, and J Walz. Electron tomography of molecules and cells. *Trends in Cell Biology*, 9:81–85, 1999.

[4] JA Berriman, S Li, LJ Hewlett, S Wasilewski, FN Kiskin, T Carter, MJ Hannah, and PB Rosenthal. Structural organization of Weibel-Palade bodies revealed by cryo-EM of vitrified endothelial cells. *Proceedings of the National Academy of Sciences of the USA*, 106(41):17407–17412, 2009.

[5] R Bierings, N Hellen, N Kiskin, L Knipe, A-V Fonseca, B Patel, A Meli, M Rose, MJ Hannah, and T Carter. The interplay between the Rab27a effectors Slp4-a and MyRIP controls hormone-evoked Weibel-Palade body exocytosis. *Blood*, 120(3):2757–2767, 2012.

[6] AL Bloom. Von Willebrand factor: Clinical features of inherited and acquired disorders. *Mayo Clinic Proceedings*, 66:743–751, 1991.

[7] R Bonfanti, BC Furie, B Furie, and DD Wagner. PADGEM (GMP140) Is a Component of Weibel-Palade Bodies of Human Endothelial Cells. *Blood*, 73(5):1109–1112, 1989.

[8] M Bowman, WM Hopman, D Rapson, D Lillicrap, M Silva, and P James. A Prospective Evaluation of the Prevalence of Symptomatic von Willebrand Dis-

ease (VWD) in a Pediatric Primary Care Population. *Pediatric Blood Cancer*, 55:171–173, 2010.

[9] A Briegel, S Chen, AJ Koster, JM Plitzko, CL Schwartz, and GJ Jensen. Correlated light and electron cryo-microscopy. *Methods in Enzymology*, 481:317–341, 2010.

[10] D Castaño-Díez, A Al-Amoudi, A-M Glynn, A Seybert, and AS Frangakis. Fiducial-less alignment of cryo-sections. *Journal of Structural Biology*, 159(3):413–423, 2007.

[11] D Castaño-Díez, M Scheffer, A Al-Amoudi, and AS Frangakis. Alignator: A GPU powered software package for robust fiducial-less alignment of cryo tilt-series. *Journal of Structural Biology*, 170(1):117–126, 2010.

[12] Y-W Chang, S Chen, EI Tocheva, A Treuner-Lange, S Löbach, L Søgaard-Andersen, and GJ Jensen. Correlated cryogenic photoactivated localization microscopy and cryo-electron tomography. *Nature Methods*, 11(7):737–739, 2014.

[13] RA Crowther, R Henderson, and JM Smith. MRC Image Processing Programs. *Journal of Structural Biology*, 116:9–16, 1996.

[14] R Danev, RM Glaeser, and K Nagayama. Practical factors affecting the performance of a thin-film phase plate for transmission electron microscopy. *Ultramicroscopy*, 109:312–325, 2009.

[15] R Danev and K Nagayama. Tranmission electron microscopy with Zernike phase plate. *Ultramicroscopy*, 88:243–252, 2001.

[16] B Daum, A Walter, A Horst, HD Osiewacz, and W Kühlbrandt. Age-dependent dissociation of ATP synthase dimers and loss of inner-membrane cristae in mitochondria. *Proceedings of the National Academy of Sciences of the USA*, 110(38):15301–15306, 2013.

[17] K De Ceunynck, SF De Meyer, and K Vanhoorelbeke. Unwinding the von Willebrand factor strings puzzle. *Blood*, 121(2):270–277, 2013.

[18] DJ De Rosier and A Klug. Reconstruction of Three Dimensional Structures from Electron Micrographs. *Nature*, 217:130–134, 1968.

[19] EC Dell'Angelica, C Mullins, S Caplan, and JS Bonifacino. Lysosome-related organelles. *The FASEB Journal*, 14(10):1265–1278, 2000.

[20] K Denzer, MJ Kleijmeer, HF Heijnen, W Stoorvogel, and HJ Geuze. Exosome: from internal vesicle of the multivesicular body to intercellular signalling device. *Journal of Cell Science*, 113(19):3365–3374, 2000.

[21] J-F Dong, JL Moake, L Nolasco, A Bernardo, W Arceneaux, CN Shrimpton, AJ Schade, LV McIntire, K Fujikawa, and JA López. ADAMTS-13 rapidly cleaves newly secreted ultralarge von Willebrand factor multimers on the endothelial surface under flowing conditions. *Blood*, 100(12):4033–4039, 2002.

[22] EL Doyle, V Ridger, F Ferraro, M Turmaine, P Saftig, and DF Cutler. CD63 is an essential cofactor to leukocyte recruitment by P-selectin. *Blood*, 118(15):4265–4273, 2011.

[23] J Dubochet, M Adrian, J-J Chang, J-C Homo, AW McDowall, and P Schultz. Cryo-electron microscopy of vitrified specimens. *Quarterly Review of Biophysics*, 21(2):129–228, 1988.

[24] J Dubochet and AW McDowall. Vitrification of pure water for electron microscopy. *Journal of Microscopy*, 124(3):RP3–RP4, 1981.

[25] EH Egelman. A robust algorithm for the reconstruction of helical filaments using single particle methods. *Ultramicroscopy*, 85:225–234, 2000.

[26] M Erent, A Meli, N Moisoi, V Babich, MJ Hannah, P Skehel, L Knipe, G Zupančič, D Ogden, and T Carter. Rate, extent and concentration dependence

of histamine-evoked Weibel-Palade body exocytosis determined from individual fusion events in human endothelial cells. *Journal of Physiology*, 538:195–212, 2007.

[27] J-M Escola, MJ Kleijmeer, W Stoorvogel, JM Griffith, O Yoshie, and HJ Geuze. Selective Enrichment of Tetraspan Protein on the Internal Vesicle of Multivesicular Endosomes and on Exosomes Secreted by Human B-lymphocytes. *The Journal of Biological Chemistry*, 273(32):20121–20127, 1998.

[28] BM Ewenstein, MJ Warhol, RI Handin, and JS Pober. Composition of the von Willebrand Factor Storage Organelle (Weibel-Palade Body) Isolated from Cultured Human Umbilical Vein Endothelial Cells. *Journal of Cell Biology*, 104:1423–1433, 1987.

[29] FGA Faas, M Bárcena, AV Agronskaia, HC Gerritsen, KB Moscicka, CA Diebolder, LF Van Driel, RWAL Limpens, E Bos, RBG Ravelli, RI Koning, and AJ Koster. Localization of fluorescently labeled structures in frozen-hydrated samples, using integrated light electron microscopy. *Journal of Structural Biology*, 181:283–290, 2013.

[30] F Ferraro, J Kriston-Vizi, DJ Metcalf, B Martin-Martin, J Freeman, JJ Burden, D Westmoreland, CE Dyer, AE Knight, R Ketteler, and DF Cutler. A Two-Tier Golgi Based Control of Organelle Size Underpins the Functional Plasticity of Endothelial Cells. *Developmental Cell*, 29(3):292–304, 2014.

[31] U Fiedler, M Scharpfenecker, S Koidl, A Hegen, V Grunow, JM Schmidt, W Kriz, G Thurston, and HG Augustin. The Tie-2 ligand angiopoietin-2 is stored in and rapidly released upon stimulation from endothelial cell Weibel-Palade bodies. *Blood*, 103(11):4150–4156, 2004.

[32] WE Fowler, LJ Fretto, KK Hamilton, HP Erickson, and PA McKee. Substructure of Human von Willebrand Factor. *Journal of Clinical Investigation*, 76:1491–1500, 1985.

[33] J Fu, AP Naren, X Gao, GU Ahmmed, and AB Malik. Protease-activated Receptor-1 Activation of Endothelial Cells Induces Protein Kinase Cα-dependent Phosphorylation of Syntaxin 4 and Munc18c. *The Journal of Biological Chemistry*, 280(5):3178–3184, 2005.

[34] Y Fukuda and K Nagayama. Zernike phase contrast cryo-electron tomography of whole mounted frozen cells. *Journal of Structural Biology*, 177:484–489, 2012.

[35] J-G Geng, MP Bevilacqua, KL Moore, TM McIntyre, SM Prescott, JM Kim, GA Bliss, GA Zimmerman, and RP McEver. Rapid neutrohpil adhesion to activated endothelium mediated by GMP-140. *Nature*, 343:757–760, 1990.

[36] V Gerke. von Willebrand factor folds into a bouquet. *The EMBO Journal*, 30(19):3880–3881, 2011.

[37] JP Giblin, LJ Hewlett, and MJ Hannah. Basal secretion of von Willebrand factor from human endothelial cells. *Blood*, 112(4):957–964, 2008.

[38] P Gilbert. Iterative Methods for the Three-dimensional Reconstruction of an Object from Projections. *Journal of Theoretical Biology*, 36:105–117, 1972.

[39] DJ Hampshire and AC Goodeve. The International Society on Thrombosis and Haemotosis von Willebrand disease database: an update. *Seminars in Thrombosis and Hemostatis*, 37(5):470–479, 2011.

[40] MJ Hannah, AN Hume, M Arribas, R Williams, LJ Hewlett, MC Seabra, and DF Cutler. Weibel-Palade bodies recruit Rab27 by a content-driven, maturation dependent mechanism that is independent of cell type. *Journal of Cell Science*, 116(19):3939–3948, 2003.

[41] MJ Hannah, P Skehel, M Erent, L Knipe, D Ogden, and T Carter. Differential Kinetics of Cell Surface Loss of von WIllebrand Factor and Its Propolypeptide after Secretion from Weibel-Palade Bodies in Living Human Endothelial Cells. *The Journal of Biological Chemistry*, 280(24):22827–22830, 2005.

[42] JR Harris. *Negative Staining and Cryoelectron microscopy*, volume 35 of *Royal Microscopical Society Microscopy Handbooks*. Bios Scientific Publishers, Oxford, UK, 1997.

[43] KJ Harrison-Lavoie, G Michaux, LJ Hewlett, J Kaur, MJ Hannah, WW Lui-Roberts, KE Norman, and DF Cutler. P-Selectin and CD63 Use Different Mechanisms for Delivery to Weibel-Palade Bodies. *Traffic*, 7:647–662, 2006.

[44] PW Hawkes. The Electron Microscope as a Structure Projector. In J Frank, editor, *Electron Tomomgraphy: Methods for Three-Dimensional Visualization of Structures in the Cell*, pages 83–112. Springer, New York, NY, 2006.

[45] LJ Hewlett, G Zupančič, G Mashanov, L Knipe, D Ogden, MJ Hannah, and T Carter. Temperature-dependence of Weibel-Palade Body exocytosis and cell surface dispersal of von Willebrand factor and its propolypeptide. *PLoS one*, 6(11):e27314, 2011.

[46] T Hrabe, Y Chen, S Pfeffer, LK Cuellar, AV Mangold, and F Förster. PyTom: a python-based toolbox for localization of macromolecules in cryo-electron tomograms and subtomogram analysis. *Journal of Structural Biology*, 178(2):177–188, 2012.

[47] R-H Huang, Y Wang, R Roth, AR Purvis, JE Heuser, EH Egelman, and JE Sadler. Assembly of Weibel-Palade body-like tubules from N-terminal domains of von Willebrand factor. *Proceedings of the National Academy of Sciences of the USA*, 105(2):482–487, 2008.

[48] D Huber, EM Cramer, JE Kaufmann, P Meda, JM Massé, EK Kruithof, and UM Vischer. Tissue-type plasminogen activator is stored in Weibel-Palade bodies in human endothelial cells. *Blood*, 99(10):3637–3645, 2002.

[49] I Hurbain, WJC Geerts, T Boudier, S Marco, AJ Verkleij, MS Marks, and G Raposo. Electron tomography of early melanosomes: Implications for melanogenesis and the generation of fibrillar amyloid sheets. *Proceedings of the National Academy of Sciences of the USA*, 105(50):19726–19731, 2008.

[50] NI Kiskin, N Hellen, V Babich, LJ Hewlett, L Knipe, MJ Hannah, and T Carter. Protein mobilities and P-selectin storage in Weibel-Palade bodies. *Journal of Cell Science*, 123:2964–2975, 2010.

[51] J Kistler and E Kellenberger. Collapse Phenomena in Freeze Drying. *Journal of Ultrastructure Research*, 59:70–75, 1977.

[52] L Knipe, A Meli, LJ Hewlett, R Bierings, J Dempster, P Skehel, MJ Hannah, and T Carter. A revised model for the secretion of tPA and cytokines from cultured endothelial cells. *Blood*, 116(12):2183–2191, 2010.

[53] M Knop, E Aareskjold, G Bode, and V Gerke. Rab3D and annexin A2 play a role in regulated secretion of vWF, but not tPA, from endothelial cells. *The EMBO Journal*, 23(15):2982–2992, 2004.

[54] JR Kremer, DN Mastronarde, and JR McIntosh. Computer Visualization of Three-Dimensional Image Data Using IMOD. *Journal of Structural Biology*, 116:71–76, 1996.

[55] K Lee, S Choi, C Yang, H-C Wu, and J Yu. Autofluorescence generation and elimination: a lesson from glutaraldehyde. *Chemical Communications*, 49:3028–3030, 2013.

[56] S Lepper, M Merkel, A Sartori, M Cyrklaff, and F Frischknecht. Rapid quantification of the effects of blotting for correlation of light and cryo-light microscopy images. *Journal of Microscopy*, 238(1):21–26, 2009.

[57] V Lučić, AH Kossel, T Yang, T Bonhoeffer, W Baumeister, and A Sartori. Multiscale image of neurons grown in culture: From light microscopy to cryo-electron tomography. *Journal of Structural Biology*, 160(2):146–156, 2007.

[58] SJ Ludtke, PR Baldwin, and W Chiu. EMAN: semiautomated software for high-resolution single-particle reconstructions. *Journal of Structural Biology*, 128:82–97, 1999.

[59] WW Lui-Roberts, LM Collinson, LJ Hewlett, G Michaux, and DF Cutler. An AP-1/clathrin coat plays a novel and essential role in forming the Weibel-Palade bodies of endothelial cells. *Journal of Cell Biology*, 170(4):627–636, 2005.

[60] J-B Manneville, S Etienne-Manneville, P Skehel, T Carter, D Ogden, and M Ferenczi. Interaction of the actin cytoskeleton with microtubules regulated secretory organelle movement near the plasma membrane in human endothelial cells. *Journal of Cell Science*, 116:3927–3938, 2003.

[61] T Marti, S Rösselet, K Titani, and KA Walsh. Identification of Disulphide-Bridged Substructures with Human von Willebrand Factor. *Biochemistry*, 26:8099–8109, 1987.

[62] DN Mastronarde. Dual-axis Tomography: An Approach with Alignment Methods That Preserve Resolution. *Journal of Structural Biology*, 120:343–352, 1997.

[63] DN Mastronarde. Automated electron microscope tomography using robust prediction of specimen movements. *Journal of Structural Biology*, 152:36–51, 2005.

[64] RM McDouall, CS Page, S Hafizi, MH Yacoub, and ML Rose. Alloproliferation of purified CD4+ T cells to adult human heart endothelial cells, and study of second-signal requirments. *Immunology*, 89:220–226, 1996.

[65] O Medalia, I Weber, AS Frangakis, D Nicastro, G Gerisch, and W Baumeister. Macromolecular Architecture in Eukaryotic Cells Visualized by Cryoelectron Tomography. *Science*, 298:1209–1213, 2002.

[66] A Meli, T Carter, A McCormack, MJ Hannah, and ML Rose. Antibody Alone Is Not a Stimulator of Exocytosis of Weibel-Palade Bodies From Human Endothelial Cells. *Transplantation*, 94(8), 2012.

[67] DJ Metcalf, TD Nightingale, HL Zenner, WW Lui-Roberts, and DF Cutler. Formation and function of Weibel-Palade bodies. *Journal of Cell Science*, 121(1):19–27, 2008.

[68] G Michaux, KB Abbitt, LM Collinson, SL Haberichter, KE Norman, and DF Cutler. The Physiological Function of von Willebrand's Factor Depends on Its Tubular Storage in Endothelial Weibel-Palade Bodies. *Developmental Cell*, 10:223–232, 2006.

[69] G Michaux and DF Cutler. How to roll an Endothelial Cigar: The Biogenesis of Weibel-Palade Bodies. *Traffic*, 5:69–78, 2004.

[70] MJ Mourik, JA Valentijn, J Voorberg, AJ Koster, KM Valentijn, and J Eikenboom. Von Willebrand Factor remodeling during exocytosis from vascular endothelial cells. *Journal of Thrombosis and Haemostasis*, in press:in press, 2013.

[71] S Nickell, F Förster, A Linaroudis, WD Net, F Beck, R Hegerl, W Baumeister, and JM Plitzko. TOM software toolbox: acquisition and analysis for electron tomography. *Journal of Structural Biology*, 149(3):227–234, 2005.

[72] TD Nightingale, DF Cutler, and LP Cramer. Actin coats and rings promote regulated exocytosis. *Trends in Cell Biology*, 22(6):329–337, 2012.

[73] TD Nightingale, K Pattni, AN Hume, MC Seabra, and DF Cutler. Rab27a and MyRIP regulate the amount and multimeric state of VWF released from endothelial cells. *Blood*, 113(20):5010–5018, 2009.

[74] TD Nightingale, IJ White, EL Doyle, M Turmaine, K Harrison-Lavoie, KF Webb, LP Cramer, and DF Cutler. Actomyosin II contractility expels von Willebrand factor from Weibel-Palade bodies during exocytosis. *Journal of Cell Biology*, 194(4):613–629, 2011.

[75] M Ostrowski, NB Carmo, S Krumeich, I Fanget, G Raposo, A Savina, CF Moita, K Schauer, AN Hume, RP Freitas, B Gould, P Benaroch, N Hacohen, M Fukuda, C Desnos, MC Seabra, F Darchen, S Amigorena, LF Moita, and C Thery. Rab27a and Rab27b control different steps of the exosome secretion pathway. *Nature Cell Biology*, 12(1):19–30, 2010.

[76] I Øynebråten, O Bakke, P Brandtzaeg, F-E Johansen, and G Haraldsen. Rapid chemokine secretion from endothelial cells originates from 2 distinct compartments. *Blood*, 104(2):314–320, 2004.

[77] T Ozaka, Y Doi, K Kayashima, and S Fujimoto. Weibel-Palade bodies as a storage site of calcitonin gene-related peptide and endothelin-1 in blood vessels of the rat carotid body. *Anatomical Record*, 247(3):388–394, 1997.

[78] M Pelts, SM Pandya, CJ Oh, and MA Model. Thickness profiling of formaldehyde-fixed cells by transmission-through-dye microscopy. *BioTechniques*, 50:389–396, 2011.

[79] EF Petterson, TD Goddard, CC Huang, GS Couch, DM Greenblatt, EC Meng, and TE Ferrin. UCSF Chimera–a visualisation system for exploratory reserach and analysis. *Journal of Computational Chemistry*, 25(13):1605–1612, 2004.

[80] RC Piper and DJ Katzmann. Biogenesis and Function of Multivesicular Bodies. *Annual Review of Cell and Developmental Biology*, 23:519–547, 2007.

[81] JM Plitzko, A Rigort, and A Leis. Correlative cryo-light microscopy and cryo-electron tomography: from cellular territories to molecular landscapes. *Current Opinion in Biotechnology*, 20:83–89, 2009.

[82] M Poeter, I Brandherm, J Rossaint, G Rosso, V Shahin, BV Skryabin, A Zarbock, V Gerke, and U Rescher. Annexin A8 controls leukocyte recruitment to activated endothelial cells via cell surface delivery of CD63. *Nature Communications*, 5(3738), 2014.

[83] MS Pols and J Klumperman. Trafficking and function of the tetraspanin CD63. *Experimental Cell Research*, 315:1584–1592, 2009.

[84] IR Pulido, R Jahn, and V Gerke. VAMP3 is associated with endothelial Weibel-Palade bodies and participates in their Ca2? - dependent exocytosis. *Biochimica et Biophysica Acta*, 1813(5):1038–1044, 2011.

[85] IR Pulido, TD Nightingale, F Darchen, MC Seabra, DF Cutler, and V Gerke. Myosin Va Acts in Concert with Rab27a and MyRIP to Regulate Acute Von-Willebrand Factor Release from Endothelial Cells. *Traffic*, 12(10):1371–1382, 2011.

[86] G Raposo and W Stoorvogel. Extracellular vesicles: Exosomes, microvesicles and friends. *Journal of Cell Biology*, 200(4):373–383, 2013.

[87] GP Resch, M Brandstetter, VI Wonesch, and E Urban. Immersion Freezing of Cell Monolayers for Cryo-Electron Tomography. *Cold Spring Harbour Protocols*, 7:815–823, 2011.

[88] A Rigort, FLB Bäuerlein, A Leis, M Gruska, C Hoffmann, T Laugks, U Böhm, M Eibauer, H Gnaegi, W Baumeister, and JM Plitzko. Micromachining tools

and correlative approaches for cellular cryo-electron tomography. *Journal of Structural Biology*, 172:169–179, 2010.

[89] F Rodeghiero, G Castaman, and E Dini. Epidemiological investigation of the prevalence of von Willebrand's disease. *Blood*, 69:454–459, 1987.

[90] E Ruska. The development of the electron microscope and of electron microscopy. *Reviews of Modern Physics*, 59(3):627–638, 1987.

[91] JE Sadler. Biochemistry and Genetics of von Willebrand factor. *Annual Review of Biochemistry*, 67:395–424, 1998.

[92] JE Sadler, U Budde, JCJ Eikenboom, EJ Favaloro, FGH Hill, L Holmberg, J Ingerslev, CA Lee, D Lillicrap, PM Mannucci, C Mazurier, D Meyer, WL Nicholds, M Nishino, IR Peake, F Rodeghiero, AB Federici, and The Working Party on von Willebrand Disease Classification. Update on the pathophysiology and classification of von Willebrand disease: a report of the Subcommittee on von Willebrand factor. *Journal of Thrombosis and Haemostasis*, 4:2103–2114, 2006.

[93] A Sartori, R Gatz, F Beck, A Rigort, W Baumeister, and JM Plitzko. Correlative microscopy: Bridging the gap between fluorescence light microscopy and cryo-electron tomography. *Journal of Structural Biology*, 160:135–145, 2007.

[94] S Schnyder-Candrian, L Borsig, R Moser, and Berger EG. Localization of alpha 1,3-fucosyltransferase VI in Weibel-Palade bodies of human endothelial cells. *Proceedings of the National Academy of Sciences of the USA*, 97(15):8369–8374, 2000.

[95] M Schorb and JAG Briggs. Correlated cryo-fluorescence and cryo-electron microscopy with high spatial precisions and improved sensitivity. *Ultramicroscopy*, 143:24–32, 2014.

[96] RR Schröder, W Hofmann, and J-F Ménétret. Zero-Loss Energy Filtering as Improved Imaging Mode in Cryoelectronmicroscopy of Frozen-Hydrated Specimens. *Journal of Structural Biology*, 105:28–34, 1990.

[97] CL Schwartz, VI Sarbash, FI Atauallakhanov, JR McIntosh, and D Nicastro. Cryo-fluorescence microscopy facilitates correlations between light and cryo-electron microscopy and reduces the rate of photobleaching. *Journal of Microscopy*, 227(2):98–109, 2007.

[98] H Slayter, J Loscalzo, P Bockenstedt, and RI Handin. Native Conformation of Human von Willebrand Protein. *The Journal of Biological Chemistry*, 260(14):8559–8563, 1985.

[99] JM Smith. XIMDISP - A visualization tool to aid structure determination from electron microscope images. *Journal of Structural Biology*, 125:223–228, 1999.

[100] MB Smith, E Karatekin, A Gohlke, H Mizuno, N Watanabe, and D Vavylonis. Interactive, Computer-Assisted Tracking of Speckle Trajectories in Fluorescence Microscopy: Application to Actin Polymerization and Membrane Fusion. *Biophysical Journal*, 101:1794–1804, 2011.

[101] LA Sporn, VJ Marder, and DD Wagner. Inducible Secretion of Large, Biologically Potent von Willebrand Factor Multimers. *Cell*, 46:185–190, 1986.

[102] TA Springer. Complement and the Multifaceted Functions of VWA and Integrin I Domains. *Structure*, 14:1611–1616, 2006.

[103] TA Springer. Biology and physics of von WIllebrand factor concatamers. *Journal of Thrombosis and Haemostasis*, 9(Suppl. 1):130–143, 2011.

[104] D Stalling, M Westerhoff, and H-C Hege. Amira: A Highly Interactive System for Visual Data Analysis. In CD Hansen and CR Johnson, editors, *Visualization Handbook*, pages 749–767. Butterworth-Heinemann, Burlington, 2005.

[105] TC Südhof and JE Rothman. Membrane Fusion: Grappling with SNARE and SM proteins. *Science*, 323:474–477, 2009.

[106] K Titani, S Kumar, K Takio, LH Ericsson, RD Wade, K Ashida, KA Walsh, MW Chopek, JE Sadler, and K Fujikawa. Amino Acid Sequence of Human von Willebrand Factor. *Biochemistry*, 25:3171–3184, 1986.

[107] E Urban, S Jacob, M Nemethova, GP Resch, and JV Small. Electron tomography reveals unbranched networks of actin filaments in lamellipodia. *Nature Cell Biology*, 12(5):429–435, 2010.

[108] JO Utgaard, FL Jahnsen, A Bakka, P Brandtzaeg, and G Haraldsen. Rapid section of prestored interleukin 8 from Weibel-Palade bodies of microvascular endothelial cells. *Journal of Experimental Medicine*, 188(9):1751–1756, 1998.

[109] KM Valentijn, JA Valentijn, KA Jansen, and AJ Koster. A new look at Weibel-Palade body structure in endothelial cells using electron tomography. *Journal of Structural Biology*, 161:447–458, 2008.

[110] KM Valentijn, LF van Driel, MJ Mourik, G-J Hendriks, TJ Arends, AJ Koster, and JA Valentijn. Multigranular exocytosis of Weibel-Palade bodies in vascular endothelial cells. *Blood*, 116(10):1807–1816, 2010.

[111] D van Breevort, AP Snijders, N Hellen, S Weckhuysen, KWEM van Hooren, J Eikenboom, K Valentijn, M Fernandez-Borja, B Ceulemans, P De Jonge, J Voorberg, M Hannah, T Carter, and R Bierings. STXBP1 promotes Weibel-Palade body exocytosis through its interaction witht the Rab27A effector Slp4-a. *Blood*, 123(20):3185–3194, 2014.

[112] LF van Driel, JA Valentijn, KM Valentijn, RI Koning, and AJ Koster. Tools for correlative cryo-fluorescence microscopy and cryo-electron tomography applied to whole mitochondria in human endothelial cells. *European Journal of Cell Biology*, 88:669–684, 2009.

[113] M van Heel, G Harauz, EV Orlova, R Schmidt, and M Schatz. A new generation of the IMAGIC image processing system. *Journal of Structural Biology*, 116(1):17–24, 1996.

[114] H van Nispen tot Pannerden, F de Haas, W Geerts, G Posthuma, S van Dijk, and HFG Heijnen. The platelet interior revisited: electron tomography reveals tubular α-granule subtypes. *Blood*, 116(7):1147–1156, 2010.

[115] CL Verweij, PJ Diergaarde, M Hart, and H Pannekoek. Full-length von Willebrand factor (vWF) cDNA encodes a highly repetitive protein considerably larger than the mature vWF subunit. *The EMBO Journal*, 5(8):1839–1847, 1986.

[116] CL Verweij, M Hart, and H Pannekoek. Expression of variant von Willebrand factor (vWF) cDNA in heterologous cells: requirement of the pro-polypeptide in vWF multimer formation. *The EMBO Journal*, 6(10):2885–2890, 1987.

[117] CL Verweij, M Hart, and H Pannekoek. Proteolytic Cleavage of the Precursor of von Willebrand Factor Is Not Essential for Multimer Formation. *The Journal of Biological Chemistry*, 263(17):7921–7924, 1988.

[118] UM Vischer, H Barth, and CB Wollheim. Regulated von Willebrand Factor Secretion Is Associated With Agonist-Specific Patterns of Cytoskeletal Remodeling in Cultured Endothelial Cells. *Arteriosclerosis, Thrombosis and Vascular Biology*, 20:883–891, 2000.

[119] UM Vischer and DD Wagner. CD63 Is a Component of Weibel-Palade Bodies of Human Endothelial Cells. *Blood*, 82(4):1184–1191, 1993.

[120] UM Vischer and DD Wagner. von Willebrand Factor Proteolytic Processing and Multimerization Precede the Formation of Weibel-Palade Bodies. *Blood*, 83(12):3536–3544, 1994.

[121] J Voorberg, R Fontijn, JA Van Mourik, and H Pannekoek. Domains involved in multimer assembly of von Willebrand factor (vWF): multimerization is independent of dimerization. *The EMBO Journal*, 9(3):797–803, 1990.

[122] DD Wagner, T Mayadas, and VJ Marder. Initial Glycosylation and Acidic pH in the Golgi Apparatus Are Required for Multimerization of von Willebrand Factor. *Journal of Cell Biology*, 102:1320–1324, 1986.

[123] DD Wagner, JB Olmsted, and VJ Marder. Immunolocalization of von Willebrand Protein in Weibel-Palade Bodies of Human Endothelial Cells. *Journal of Cell Biology*, 95:355–360, 1982.

[124] DD Wagner, S Saffaripour, R Bonfanti, JE Sadler, EM Cramer, B Chapman, and T Mayadas. Induction of Specific Storage Organelles by von Willebrand Factor Propolypeptide. *Cell*, 64:403–413, 1991.

[125] JW Wang, DJ Groeneveld, G Cosemans, RJ Dirven, KM Valentijn, J Voorberg, PH Reitsma, and J Eikenboom. Biogenesis of Weibel-Palade bodies in von Willebrand disease varients with impaired von Willebrand factor intrachain or interchain disulfide bond formation. *Haematologica*, in press:in press, 2012.

[126] JW Wang, KM Valentijn, HC de Boer, RJ Dirven, AJ van Zonneveld, AJ Koster, J Voorberg, PH Reitsma, and J Eikenboom. Intracellular Storage and Regulated Secretion of Von Willebrand Factor in Quantitative Von Willebrand Disease. *The Journal of Biological Chemistry*, 286(27):24180–24188, 2011.

[127] Q Wang, CP Mercogliano, and J Löwe. A Ferritin-Based Label for Cellular Electron Cryotomography. *Structure*, 19:147–154, 2011.

[128] ER Weibel. Fifty years of Weibel-Palade bodies: the discovery and early history of an enigmatic organelle of endothelial cells. *Journal of Thrombosis and Haemostasis*, 10:979–984, 2012.

[129] ER Weibel and GE Palade. New Cytoplasmic Components in Arterial Endothelia. *Journal of Cell Biology*, 23:101–112, 1964.

[130] H Winkler. 3D reconstruction and processing of volumetric data in cryo-electron tomography. *Journal of Structural Biology*, 157:126–137, 2007.

[131] RJ Wise, PJ Barr, PA Wong, MC Kiefer, AJ Brake, and RJ Kaufman. Expression of a human propeptide processing enzyme: Correct cleavage of the von Willebrand factor precursor at a paired basic amino acid site. *Proceedings of the National Academy of Sciences of the USA*, 87:9378–9382, 1990.

[132] AJ Xu and TA Springer. Mechanisms by which von Willebrand Disease Mutations Destabilize the A2 Domain. *The Journal of Biological Chemistry*, 288(9):6317–6324, 2013.

[133] ACW Zannettino, CA Holding, P Diamond, GJ Atkins, P Kostakis, A Farrugia, J Gamble, LB To, DM Findlay, and DR Haynes. Osteoprotegerin (OPG) Is Localized to the Weibel-Palade Bodies of Human Vascular Endothelial Cells ans Is Physically Associated With von WIllebrand Factor. *Journal of Cell Physiology*, 204:714–723, 2005.

[134] HL Zenner, LM Collinson, G Michaux, and DF Cutler. High-pressure freezing provides insights into Weibel-Palade body biogenesis. *Journal of Cell Science*, 120(12):2117–2125, 2007.

[135] Q Zhang, Y-F Zhou, C-Z Zhang, X Zhang, C Lu, and TA Springer. Structural specializations of A2, a force-sensing domain in the ultralarge vascular protein von Willebrand factor. *Proceedings of the National Academy of Sciences of the USA*, 106(23):9226–9231, 2009.

[136] X Zhang, K Halvorson, C-Z Zhang, WP Wong, and TA Springer. Mechanoenzymatic Cleavage of the Ultralarge Vascular Protein von Willebrand Factor. *Science*, 324:1330–1334, 2009.

[137] Y-F Zhou, ET Eng, N Nishida, C Lu, T Walz, and TA Springer. A pH-regulated dimeric bouquet in the structure of von Willebrand factor. *The EMBO Journal*, 30(19):4098–4111, 2011.

[138] Y-F Zhou, ET Eng, J Zhu, C Lu, T Walz, and TA Springer. Sequence and structure relationships within von Willebrand factor. *Blood*, 120(2):449–458, 2012.

[139] Y-F Zhou and TA Springer. Highly reinforced structure of a C-terminal dimerization domain in von Willebrand factor. *Blood*, 123(12):1785–1793, 2014.

[140] S Zografou, D Basagiannis, A Papafotika, R Shirakawa, H Horiuchi, D Auerbach, M Fukuda, and S Christoforidis. A complete Rab screening reveals novel insights in Weibel-Palade body exocytosis. *Journal of Cell Science*, 125:4780–4790, 2012.